Spring 2014

Effect of hydrogen addition and burner diameter on the stability and structure of lean, premixed flames

Kelsey Leigh Kaufman
University of Iowa

EFFECT OF HYDROGEN ADDITION AND BURNER DIAMETER ON THE STABILITY AND STRUCTURE OF LEAN, PREMIXED FLAMES

by

Kelsey Leigh Kaufman

A thesis submitted in partial fulfillment
of the requirements for the Master of
Science degree in Mechanical Engineering
in the Graduate College of
The University of Iowa

May 2014

Thesis Supervisor: Associate Professor Albert Ratner

Graduate College
The University of Iowa
Iowa City, Iowa

CERTIFICATE OF APPROVAL

_____

MASTER'S THESIS

_____

This is to certify that the Master's thesis of

Kelsey Leigh Kaufman

has been approved by the Examining Committee
for the thesis requirement for the Master of Science
degree in Mechanical Engineering at the May 2014 graduation.

Thesis Committee: _____
Albert Ratner, Thesis Supervisor

_____
James Buchholz

_____
Ching-Long Lin

_____
HS Udaykumar

ACKNOWLEDGMENTS

First and foremost, I would like to commend Professor Albert Ratner for his approachability, responsiveness, and excellent mentoring skills. His outgoing nature and unique personality has made my experience at The University of Iowa fun and very rewarding. I count myself lucky to have had the opportunity to learn through his guidance.

I'd also like to thank the three undergraduate students—Kristen Kremer, Ben Karkow, and Andrew Sterling—who took time out of their schedules to help me out in the lab. Additionally, I'd like to thank them for understanding my inexperience and for helping me learn more about my leadership style and the minutia involved with the ongoing and extensive troubleshooting involved in running a laboratory. In addition to having the privilege of leading a fantabulous group of undergraduate students, I also had the opportunity to learn from some amazing mentors. I'd like to thank Majid Emadi for his patience as I joined the LSB research team. For Jianan Zhang, I'd like to express my gratitude for having the flexibility to spontaneously assist in data collection, troubleshoot, and fix the miscellaneous number of roadblocks that arose.

To Tim Dinolfo, I'd like to express my love and gratitude for the everlasting support and sacrifices that were made throughout this entire process. I am indebted to him for his company and motivation that pushed me to endure the lack of sleep and seemingly never-ending, back-to-back nights in the lab.

To my parents, Rick and Tammy Kaufman, I owe the world. Giving me the gift of a college education, I have had the opportunity to focus my stress and efforts solely on academia. Their ongoing positivity and encouragement has bolstered my independence and strengthened my belief that with their continued support, I will always be able to surmount any mountainous challenge that stands in my way.

ABSTRACT

Low swirl burners (LSBs) have gained popularity in heating and gas power generation industries, in part due to their proven capacity for reducing the production of NO_x, which in addition to reacting to form smog and acid rain, plays a central role in the formation of the tropospheric ozone layer. With lean operating conditions, LSBs are susceptible to combustion instability, which can result in flame extinction or equipment failure. Extensive work has been performed to understand the nature of LSB combustion, but scaling trends between laboratory- and industrial-sized burners have not been established. Using hydrogen addition as the primary method of flame stabilization, the current work presents results for a 2.54 cm LSB to investigate potential effects of burner outlet diameter on the nature of flame stability, with focus on flashback and lean blowout conditions. In the lean regime, the onset of instability and flame extinction have been shown to occur at similar equivalence ratios for both the 2.54 cm and a 3.81 cm LSB and depend on the resolution of equivalence ratios incremented. Investigations into flame structures are also performed. Discussion begins with a derivation for properties in a multicomponent gas mixture used to determine the Reynolds number (Re) to develop a condition for turbulent intensity similarity in differently-sized LSBs. Based on this requirement, operating conditions are chosen such that the global Reynolds number for the 2.54 cm LSB is within 2% of the Re for the 3.81 cm burner. With similarity obtained, flame structure investigations focus on flame front curvature and flame surface density (FSD). As flame structure results of the current 2.54 cm LSB work are compared to results for the 3.81 cm LSB, no apparent relationship is shown to exist between burner diameter and the distribution of flame surface density. However, burner diameter is shown to have a definite effect on the flame front curvature. In corresponding flow conditions, a decrease in burner diameter results a broader distribution of curvature and

an increased average curvature, signifying that compared to the larger 3.81 cm LSB, the flame front of the smaller burner contains tighter, smaller scale wrinkling.

TABLE OF CONTENTS

LIST OF TABLES

LIST OF FIGURES

NOMENCLATURE

Parameters

$\langle c \rangle$	Mean progress variable
a	Molar coefficient of air
A	Area
A/F	Air-to-fuel ratio
b	4.76 times the molar coefficient of air
BG	Burned gases
c	Speed of sound
c_p	Specific heat for constant pressure
D	Diameter
	Diffusivity
E	Activation energy
F/A	Fuel-to-air ratio
h	Flame front curvature
k	Thermal conductivity
L	Length or lengthscale
Le	Lewis number
L_i	i^{th} damping process
m	Mass
MW	Molecular weight
n	Moles
n_f	Number of images
p	Chamber pressure
q	Heat release
r	Radius of integration
R	Universal gas constant
	Radius/Radius of Curvature
	Rayleigh Index
Re	Reynolds Number
s	Entropy
S	Speed
	Swirl number
	System boundary
t	Time
T	Period
	Temperature
u, U	Velocity
UR	Unburned reactants
V	Velocity
V	Volume
W	Width of normalized PDF
x	Number of carbon atoms in hydrocarbon
	Mole fraction
y	Number of hydrogen atoms in hydrocarbon

Greek Symbols

α	Flame angle
	Thermal diffusivity
	Volumetric fraction
β	Zeldovich number
γ	Ratio of specific heats
θ	Azimuthal direction
μ	Dynamic viscosity
	Mean/average
ν	Kinematic viscosity
ξ	Non-dimensional time
ρ	Density
Σ	Flame surface density
σ	Standard deviation
ϕ	Equivalence ratio

Subscripts

a	Air
c	Characteristic
	Critical
f	Fuel
L	
rms	Root mean sqare
stoic	Stoichiometric
t	Turbulent
u	Reactants
x	Axial direction

Superscripts & Accents

$'$	Fluctuation
*	Radical electron
^{o}	Reference state
$\dot{}$	Rate/per time
$\bar{}$	Average/Mean

CHAPTER 1

INTRODUCTION

1.1 Background and Motivation

Considered a practical, "state-of-the-art" alternative, interest in lean, premixed combustion systems began in the early 1980s. Initially, burners for these combustion systems were introduced in high-efficiency condensing boilers in domestic central heating appliances to sufficiently overcome the pressure drop observed through the condensing heat exchangers.[1] Recently, these burners have become increasingly common in application of NO_x reduction strategies,[2] especially in industrial applications like natural gas heating and power generation systems.[3,4,5] With increased concern regarding emissions over the last decade or so, premixed combustion systems operating in the lean regime have been brought to the forefront of advancing combustion technology. However, the benefits of NO_x reduction associated with lean, premixed combustion are also accompanied by an increased susceptibility to combustion instabilities,[3,6,7,8] which, when coupled with acoustically-forced pressure perturbations or heat release oscillations, can enter a vicious feedback loop which may result in increased rates of equipment failure, system downtime, or hazardous explosions. Although many examinations have investigated processes involved in flame stabilization, much work is yet to be completed for full comprehension of the phenomena and control of combustion instabilities in lean, premixed systems.

Industrially, lean, premixed combustion systems are commonly found in gas turbines involved in power generation. Typically, these large-scale turbines contain high-swirl burners, which utilize recirculation zones centered in the flow field at the exit of the burner to stabilize the flame by circulating intermediary combustion products toward the flame base such that the incoming flow velocity can be modified to match the magnitude of the flame speed[9,10] and provide a source for the continuous ignition of the fresh,

unburned reactants.[11] However, the recirculation zones can have unfavorable effects on the oscillatory heat release patterns and the combustion process, which may lead to increased operation time under unstable operating conditions.[1]

Developed by Robert K. Cheng of the Lawrence Berkeley National Laboratory, an alternative option to the typical high swirl burner is the low swirl burner (LSB), which stabilizes the flame using flow divergence techniques instead of with recirculation zones. In LSBs, the freely propagating flame is possible due to a balance between the unburned gas velocity and the speed of the flame front.[12,13,14] Even with increasingly turbulent conditions, LSBs have been shown to reduce NO_x emissions and provide increased flame stabilization better than typical high swirl systems. Extensive work has been performed in examining the physics of LSB combustion, but with the exception of the laminar flame speed,[15] many scaling trends—if they exist—have not yet been determined for translation of results from a laboratory scale system to an industrial-sized system.

In recent studies, both numerical and experimental work has shown that improving the stability limits of lean, premixed combustion systems can be achieved with the addition of hydrogen to the fuel mixture, which increases the reactivity of the fuel. Many investigations have delved into the stability limits and regimes associated with lean, premixed combustion in LSB systems with hydrogenated fuel.[16] Specifically, the recent work of Emadi[17] has extended the knowledge of fuel hydrogenation and its effects on the stability and structures found within a 3.81 cm LSB flame. The current work provides a derivation for expressions of characteristic properties of gaseous reactant mixtures. With these results, assays similar to those performed in the 3.81 cm LSB system are employed to examine the effect of fuel hydrogenation on flame stability and structure for a 2.54 cm burner. After confirming that the trends in the current work are in agreement with those predicted by previous studies, dimensionless parameters are utilized to compare results of the current work to previous work to investigate potential

effects that burner diameter may have on stability limits and flame structures in LSB combustion.

1.2 Objectives & Outline

The understanding of combustion instability has come a long way since its discovery. In fact, knowledge of instability in lean, premixed systems has reached a point where many general trends have been well established. However, due to the differences in flammability limits and flow dynamics, phenomena resulting from combustion instability still have yet to be adequately scaled from a laboratory scale to a scale comparable to the combustor systems found in industry. Then, the current work acts to examine well established trends regarding the addition of hydrogen in a preliminary attempt to correlate characteristics of combustion systems utilizing similar burners of a different size.

To begin, Chapter 2 offers a literature review that highlights basic combustion theory, the history and modeling considerations surrounding combustion instability, as well as flame stabilization and imaging techniques utilized in studying the physics of combustion. Following the literature review, Chapter 3 guides readers through the arrangement of the experimental apparatus and its four main subsystems: the combustion chamber and 2.54 cm LSB, the gas supply system, the optics and imaging system, and the data acquisition system. In Chapter 4, a derivation is provided such that mixture properties can be evaluated using known quantities. Experimental results regarding stability and flammability limits—specifically flashback and blowout—and flame structures are presented and discussed in terms of established trends and previous results obtained using a 3.81 cm LSB. Trends predicted by earlier work in flame stability and flame structures are used to validate the results of the current work, and the effect of

burner diameter on these parameters is subsequently investigated. Chapter 5 provides conclusions regarding results and observations presented in previous chapters, as well as detailing paths that may be taken in the future to refine the current results and further the understanding of instability in lean, premixed combustion systems.

CHAPTER 2

LITERATURE REVIEW

Because of the lean nature of premixed, swirled combustion, the many industrial systems are inherently susceptible to combustion instability, which forms the basis for investigations performed in the current work with a low swirl burner. Within this chapter, an extensive summary of previous work will be presented to provide a solid foundation on the topics associated with the current work. To begin, a review of combustion theory and relevant flame parameters, information regarding the discovery and different types of combustion instability, and the formulation of conditions required for acoustically-induced instability will be presented. Discussion will continue with motivation and methods of flame stabilization that aid in efforts to reduce the risks associated with combustion instability. The literature review will conclude with a discussion on techniques used to examine flames in laboratory-based combustion systems.

2.1 Combustion Theory and Relevant Flame Parameters

To explore the depths of the field of fluid mechanics, it is inherently required that the terminology associated with fluid flow is understood. In a similar fashion, the field of combustion physics is also accompanied by its own lexicon of terms inherent to a basic understanding of combustion theory. Before diving into the combustion topics associated with the current examination of lean, premixed flames, the current section will introduce parameters associated with a combustion system. Many more concepts exist to characterize a combustion process, but only those related to the current study will be presented here. Introductions will begin with a discussion of the equivalence ratio for two combustion reactions. In the first reaction, simple combustion of an arbitrary hydrocarbon molecule is assessed. In the second, this concept is tailored to methane

(CH_4) and the possible addition of hydrogen gas (H_2) to the fuel mixture. The flame speed is characterized, and the effect of the equivalence ratio on flame speed is detailed. From this point, the Reynolds number (Re) and the Lewis number (Le) are discussed in relation to the field of combustion physics, and background on the flame front curvature and flame surface density (FSD)—the two basic flame structures examined in the current study—are presented.

2.1.1 Equivalence Ratio and Mixture Ratio

In burning a generalized hydrocarbon with air as the oxidizer, the stoichiometric (perfect ratio of oxidizer to fuel for complete combustion) combustion process can be approximated by the chemical reaction shown in Equation 2.1. In reality, air is comprised of more than oxygen and nitrogen, but in deriving the relationship known as the equivalence ratio, it will be assumed that air consists of 21% O_2 and 79% N_2. The molar coefficient before the reacting air species, a, is such that $a = x + y/4$ for the stoichiometric burning of hydrocarbon C_xH_y.

$$C_xH_y + a(O_2 + 3.76N_2) \rightarrow xCO_2 + \frac{y}{2}H_2O + 3.76aN_2 \tag{2.1}$$

If the molecular weights of the air and fuel are given by MW_{air} and MW_{fuel}, respectively, then the air-fuel ratio required for stoichiometric burning is given by Equation 2.2.

$$(A/F)_{stoic} = \left(\frac{m_{air}}{m_{fuel}}\right)_{stoic} = 4.76a\frac{MW_{air}}{MW_{fuel}} \tag{2.2}$$

In describing the characteristics of combustion, a process is usually defined as fuel-lean or fuel-rich. This is achieved by characterizing the equivalence ratio, ϕ, of a system, which quantitatively indicates the relationship of the air-fuel ratio of a physical process to the stoichiometric air-fuel ratio. Defined as shown in Equation 2.3, an equivalence ratio of unity indicates that the actual air-fuel mixture is stoichiometric. By the same logic, a fuel-lean mixture—a mixture containing more than the stoichiometric amount of oxidizer—is defined for an equivalence ratio such that $\phi < 1$. Conversely, a fuel-rich mixture—a mixture containing less than the stoichiometric amount of oxidizer—is defined for $\phi > 1$.

$$\phi = \frac{(A/F)_{stoic}}{(A/F)} = \frac{(F/A)}{(F/A)_{stoic}} \tag{2.3}$$

In the current work, the fuel mixture only ever consists of up to two gaseous fuels: methane and hydrogen. In some cases, the fuel used is pure methane. However, when blending the methane and hydrogen, it is necessary to define amount of hydrogen within the mixture. In the current work, this will be defined using percent by volume. Then, the percent hydrogen (by volume), given by α_{H_2}, is defined as shown in Equation 2.4, where V_{H_2} and V_{CH_4} is the volume of hydrogen and methane within the mixture, respectively. Also called the volumetric fraction of hydrogen, this parameter can be used in defining molar coefficients for the reaction shown in Equation 2.5.

$$\alpha_{H_2} = \frac{V_{H_2}}{V_{H_2} + V_{CH_4}} \tag{2.4}$$

$$\left(1-\alpha_{H_2}\right)CH_4+\alpha_{H_2}H_2+\left(2-1.5\alpha_{H_2}\right)(O_2+3.76N_2)\rightarrow$$
$$\left(1-\alpha_{H_2}\right)CO_2+\left(2-\alpha_{H_2}\right)H_2O+3.76\left(2-1.5\alpha_{H_2}\right)N_2 \quad (2.5)$$

Then, following a process similar to that used in the previous derivation of the generalized equivalence ratio, Equation 2.6 gives the relationship for the stoichiometric fuel-air ratio while Equation 2.7 gives the equivalence ratio as it is defined in the current work.

$$(F/A)_{stoic}=\left(\frac{m_{fuel}}{m_{air}}\right)_{stoich}=\frac{1}{4.76\left(2-1.5\alpha_{H_2}\right)}\frac{MW_{fuel}}{MW_{air}} \quad (2.6)$$

$$\phi=\frac{(F/A)}{(F/A)_{stoic}}=4.76\left(2-1.5\alpha_{H_2}\right)(F/A)\frac{MW_{air}}{MW_{fuel}} \quad (2.7)$$

2.1.2 Flame Speed

Another important flame parameter used in the characterization of combustion systems is the flame speed, which is highly dependent on fuel composition and the nature of the flow field. In the current work, the flame speed is primarily employed in discussions regarding trends observed in flame stability limits, which will be discussed in more detail. For a reference coordinate system fixed to the laboratory reference frame, a perfectly stable flame may appear to be unmoving. However, the flame front is a self-sustaining wave of combustion propagating at the flame speed, which is the primary property that dictates many stability characteristics of the flame, including blowout and flashback. In both laminar and turbulent flows, the same physical processes are active. In fact, many turbulent flame theories are based on the flame's underlying laminar structure.[18] For a generalized laminar flame front, as in the vector diagram shown in

Figure 2.1, the laminar flame speed is given by the expression in Equation 2.8, which is simply the component of the unburned reactant velocity in the direction normal to the flame front. This speed, S_L, is the velocity of the flame front as observed from a reference frame moving with the unburned reactant mixture entering with incoming velocity, V_u. From the laboratory reference frame, the front having the propagation velocity shown in Equation 2.8 would appear as a stationary flame.

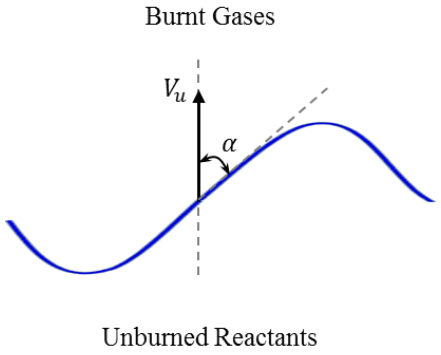

Figure 2.1: Geometry of a Laminar Flame Front

$$S_L = V_u \sin(\alpha) \tag{2.8}$$

Unlike laminar flames, which are dependent on the mixture properties of the flow, the propagation velocity of a turbulent flame is also dependent on the character of the flow. This turbulent flame speed is the velocity at which the unburned reactant mixture enters the flame zone in a direction normal to the flame. Here, the flame surface is assumed to be a time-averaged quantity, and is represented by $\bar{A}$. As defined in Equation 2.9, the turbulent flame speed is also dependent on the density of the reactant mixture (ρ_u) and the reactant flow rate, $\dot{m}$.

$$S_t = \frac{\dot{m}}{\bar{A}\rho_u} \tag{2.9}$$

In the current work, the sets of operating conditions are programmed during data collection such that the bulk mass flow rate of the reactants is held constant. Then, if the temporally averaged surface area of the flame is assumingly similar from one flame to the next, the turbulent flame speed is highly dependent on the density of the fuel/air mixture. Chapter 4 includes a set of derivations required for calculating the Reynolds number for the reactant mixture, but it can also be shown within this derivation that as the equivalence ratio increases, the density of the reactant mixture decreases. Then, from the relationship shown in Equation 2.9 for a constant mass flow rate and time-averaged surface area, an increase in the equivalence ratio of the reactant flow can be shown to increase the propagation velocity of a turbulent flame front. The sensitivity of the turbulent flame speed to the equivalence ratio is useful in investigating the stability characteristics of the 2.54 cm LSB flames examined in the current work. Additionally, because the parameter is highly dependent on the composition of the reactant mixture, adding hydrogen to a fuel mixture is expected to alter the turbulent flame speed. The specific effects of hydrogenation on turbulent flame speed will be presented in the upcoming discussion on flame stabilization through hydrogen addition.

2.1.3 Dimensionless Parameters

In the realm of combustion, many dimensionless parameters are useful in simplifying experimental design and in defining the dynamics and phenomena occurring within the flow field. Here, however, the discussion is limited to parameters relevant to the current study: the Reynolds number and the Lewis number.

2.1.3.1 Reynolds Number

One of the most commonly known dimensionless parameters in any thermal-fluids application is the Reynolds number, which is defined the ratio between inertial effects and viscous effects in the flow field. In the basic definition for the Reynolds number, as shown in Equation 2.10, the characteristic length scale, L_c, is typically determined by the hardware or device used in the combustion process, but can also be defined by alternative length scales specific to the system. Here, the velocity used in defining the macro-scale Reynolds number is the mean flow velocity, and the characteristic length scale is given as the diameter of the burner. Although other length scales do exist for the system and LSB, industry is interested in the effect of the exit diameter of the burner. Then, even though another length scale may be more relevant in characterizing the dynamics of the flow field, the outlet diameter of the burner is used as the characteristic length scale for the current work. In the current study, the mean velocity is taken to be bulk velocity of the incoming reactants. This is the primary Reynolds number that will be used in comparisons to related work, even though alternative turbulent Reynolds numbers have been defined for combustion systems. For example, the current work will compare flame structure results to Emadi's[17] results for the 3.81 cm LSB due to the identical nature of the majority of flame parameters. However, in Emadi's work, the burner size used is 1.5 times larger than that used in the current work. Because flow properties of the mixture (density, viscosity) vary with the composition of the reactant mixture, scaling the Reynolds number between the 2.54 cm burner and 3.81 cm burner is not a simply scaled by 1.5. Instead, an analysis is performed in Chapter 4 to derive expressions for density and viscosity properties of the reactant mixture in terms of known quantities, such as the equivalence ratio and the volumetric fraction of hydrogen. With this derivation and the definition of the macro-scale, or global, Reynolds number from Equation 2.10, the condition required for Reynolds number similarity can be determined, and is presented in Chapter 4.

$$Re_L = {\bar{U}L_c}/{\nu} \tag{2.10}$$

As briefly mentioned, alternative definitions for the Reynolds number do exist. In turbulent flows, four primary length scales can be defined, including that shown in Equation 2.10. The three other Reynolds number definitions are interrelated, but due to the method of similarity used in characterizing the systems involved in the current work, they will not be discussed here. For more detail on the turbulent Reynolds numbers, the reader is referred to Turns'[18] introductory chapter on turbulent flows.

2.1.3.2 Lewis Number

As it is defined in Equation 2.11, the Lewis number provides insight to the relative rates of thermal diffusion to molecular diffusion. Both the thermal diffusivity, α, and the diffusion coefficient, *D*, are dependent on the species present within the system. For example, the diffusive coefficient of methane in air is approximately 0.22 cm^2/s[19] while the diffusive coefficient for hydrogen in air is approximately 0.61 cm^2/s.[18] Then, the diffusivity of hydrogen in air is approximately 280% of methane in air. The main reason for this huge difference in diffusivities is the size of the molecules; methane is a much larger atom than hydrogen.

$$Le = {k}/{\rho c_p D} = {\alpha}/{D} \tag{2.11}$$

Then, hydrogen can be added to a methane fuel mixture to increase the molecular diffusivity associated with the flow, and decrease the respective Lewis number. This will be discussed in more detail during review of thermal-diffusive instabilities and the effect of hydrogen addition on the stability limits of a flame.

2.1.4 Flame Front Curvature

For an arbitrary flame front with outward normal defined as in Figure 2.2, regions of the flame convex to the unburned reactants will be defined as having positive curvature, while regions of the flame concave to the reactants will be defined as having negative curvature. Positive regions and negative regions of the simple flame front shown in Figure 2.2 are depicted by the red and blue regions of the front, respectively.

However, for a more complex surface, a series of algorithms must be performed to determine the curvature of the flame front. Images of the flame front are obtained using OH planar laser-induced fluorescence (PLIF), which will be discussed in more detail in review of flame imaging techniques. Sample OH-PLIF images are shown in Figure 2.3; qualitatively, it can be seen that from Figure 2.3a to 2.3b to 2.3c, the radii of curvature decrease. Then, because curvature is defined as the inverse of the radius of curvature (by definition), it would be expected that when moving from Figure 2.3a to 2.3b to 2.3c, the flame front curvature would increase. Emadi[17] analyzed these images and showed that quantitatively, flame front curvature does, in fact, increase with an increase in fuel hydrogenation.

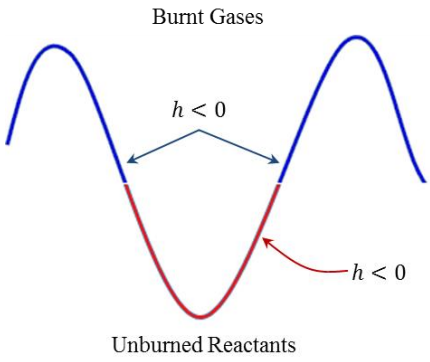

Figure 2.2: Sign convention for flame front curvature, h

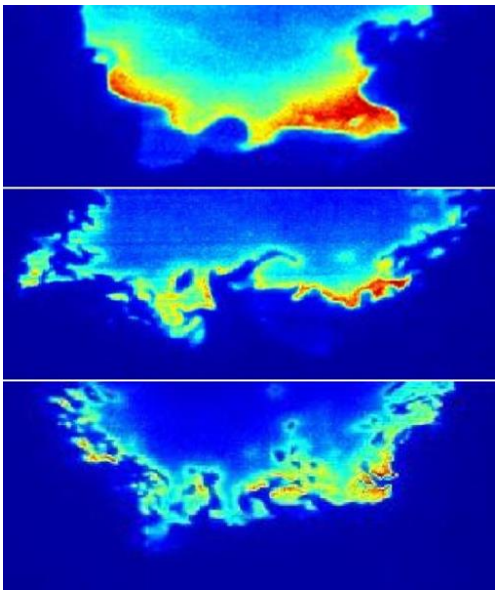

Figure 2.3: Instantaneous OH-PLIF images of flames with increasing flame front curvature due to increasing fraction of hydrogen within the fuel mixture

Source: [17]

Because one goal of the current work is to compare curvature data for burners of different sizes, a process similar to that utilized by Emadi[17] is executed to quantify flame front curvature in the current work. First, MATLAB is utilized to implement the Canny edge detection algorithm to locate the boundary (y) between the hydroxyl layer and the unburned reactants. Then, instantaneous radii of curvature (R) along the boundary are found using a Cartesian coordinate system and the definition shown in Equation 2.12. By taking the inverse and modifying the sign to match the convention with positive in regions of convexity toward the unburned gases, flame front curvature (h) is found as defined in Equation 2.13. To decrease the computation time and power required, the flame front curvature can be computed directly (without first finding radii of curvature)

using Equation 2.13. From this point, statistical analyses are applied to examine and compare the curvature characteristics of different flame fronts.

$$R = \frac{\left[1+\left(\frac{dy}{dx}\right)^2\right]^{3/2}}{\left|\frac{d^2y}{dx^2}\right|} \tag{2.12}$$

$$h = \frac{\frac{d^2y}{dx^2}}{\left[1+\left(\frac{dy}{dx}\right)^2\right]^{3/2}} \tag{2.13}$$

Shepherd[20] and Soika[21] are among others who have examined curvature of the flame front in premixed, turbulent flames. In both studies, the structures were examined for cases of extreme turbulence. In Shepherd's work with LSBs, increasing the turbulence (via the modification of the mass flow rate and bulk velocity) resulted in a broadening of the flame front curvature distributions, indicating that the increase in turbulence led to an increase in convolution of the flame front.[20] Although operating conditions are much different and a swirl-stabilized burner is used, Soika's observations for a bluff-body stabilized burner are in agreement with Emadi's results.[17] That is, Soika observed that an increase in chamber pressure (with a range from 5 bar to 15 bar) resulted in widening of the flame front curvature distribution.

2.1.5 Flame Surface Density

As in the process used to determine flame front curvature, MATLAB is used to apply the Canny edge detection algorithm to delineate the boundary between the OH field and the unburned reactants. Then, with this boundary, nondimensional mean progress variable contours– $\langle c \rangle$ –are defined, as shown in Figure 2.4. Theoretically, the contours

of the progress variable signify the margins of the region in which the boundary of the OH layer is most likely to occur. The binarized edges of the OH boundary are overlaid on the mean progress contours. The total length of the OH boundaries falling between the $\langle c \rangle$ contours is summed, and given by $L(\langle c \rangle)$. Similarly, the total 2D area of the flame brush falling within the contours is calculated using MATLAB, and is defined by $A(\langle c \rangle)$. Pictorial representations of these quantities are shown in Figure 2.4.

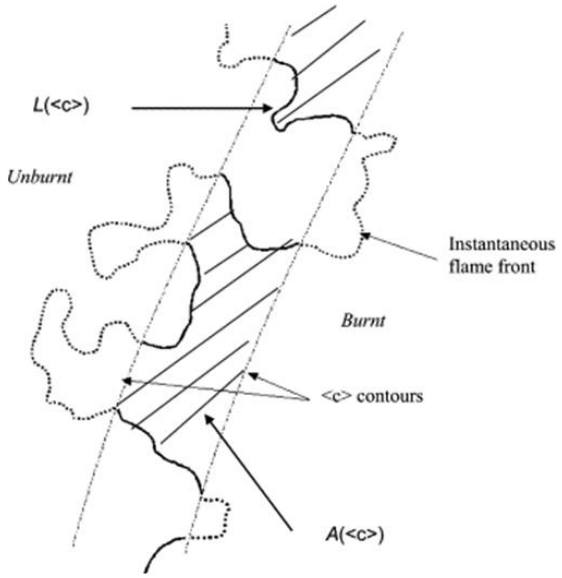

Figure 2.4: Graphical depiction of parameters required for calculation of flame surface density

Source: [22]

Within a data set consisting of n_f images, this process is performed for each instantaneous OH-PLIF image. The flame surface density, Σ, can then be calculated using this information from 900 images by employing the relationship shown in Equation 2.14.

$$\Sigma(\langle c \rangle) = \frac{L(\langle c \rangle)}{n_f A(\langle c \rangle)} \tag{2.14}$$

For fundamentally different burner geometries and experimental configurations, it has been shown that as a function of the progress variable, $\langle c \rangle$, the flame surface density exhibits parabolic trends.[17,20,21,23,120]

2.2 Combustion Instability:
History and Modeling Considerations

In closed combustion chambers, oscillating regimes called combustion instabilities are observed when acoustics and combustion are strongly coupled.[24] However, because of the unsteady nature of combustion, direct observation of the flame is not sufficient for fully understanding the attributes of these instabilities. To comprehend the details of the effect of instabilities on combustion, the types of instabilities must first be understood. In understanding the physics of a combustion system and the possible instabilities that may exist, characteristics of the system must be gathered for modeling and analysis. In the following discussion, the history and discovery of combustion instabilities will be offered and characterization of combustion instability will be discussed, highlighting the mathematical criteria for instability to occur. At this point, background on four types of instability is presented, followed by mechanisms of instability instigation. The current section will conclude with a discussion of the Rayleigh index and Rayleigh index maps, which are used in modeling instability and visualizing associated flame structures.

2.2.1 Discovery of the Instability

The examination of combustion instability may be traced back to 1777, in which Higgins first observed the peculiar "singing wave" phenomenon. In 1802, Higgins[25] reported details of the investigation into these sound-producing flames. Glass tubes of various diameters—sealed at the far end—were placed over gaseous hydrogen flames. With smaller-diameter tubes, Higgins reported that the hydrogen flame was extinguished. However, as the diameter of the tube was increased, the tone produced by the flame would develop, changing pitch and intensity based on the "width, length, and thickness of the glass jar or sealed tube."[25] However, as the diameters of the tubes became increasingly large, the sounds produced by the flame would weaken, and ultimately cease to occur.

In the mid nineteenth century, Rijke[26] expanded upon Higgins' work using air and an apparatus now known as the Rijke tube. Shown in Figure 2.5, the Rijke tube—unlike Higgins' experimental setup—is open on both ends and instead of the hydrogen flame, employs layer(s) of thin gauze composed of red-hot, iron wire as the heat source, and usually has a large length-to-diameter ratio. In this case, the wire gauze heats the surrounding air, resulting in the convection of the air upward through the tube due to local differences in the density of the air. Rijke noticed that tones were produced regardless of the type of flame used to heat the wire gauze, and used specific gases to prove that water vapor is not required for the existence of sound. With his apparatus, Rijke noted in covering the top of the tube (as in Higgins' work),[25] no sound would be produced, leading to the conclusion that the upward convection of air through the tube was necessary for the generation of sound. Rijke also examined the effect of changing the relative position of the wire gauze within the tube. The most intense sounds were produced when wire gauze is placed above the bottom of the tube at a distance of one-fourth of the length of the tube. Additionally, Rijke reported that oscillations occurred if

the gauze was placed in the lower half of the tube, but would subside if placed in the upper half of the tube.

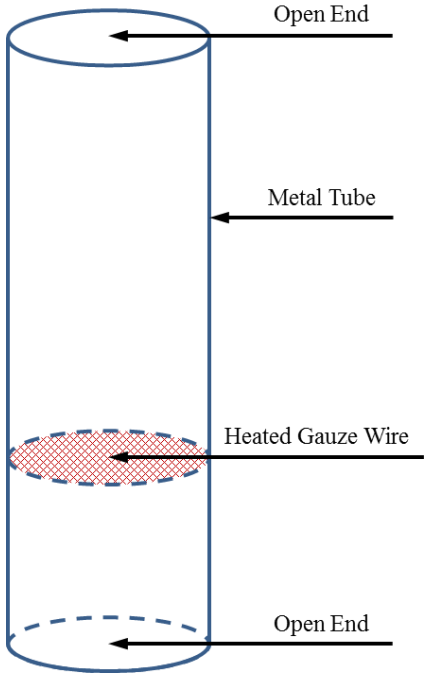

Figure 2.5: The Rijke tube apparatus

In continuing Rijke's observations, Tyndall[27] disclosed that in his experimentation, sound could always be produced by adjusting the size of the flame relative to the size of the tube, and that the "shaking of the flame" that he observed was directly proportional to the pitch created by the flame. For flames that did not naturally produce any sound, Tyndall was able to trigger the sound by creating the correct pitch himself (via a tuning fork or his own voice). In this practice, the pitch produced by the flame was the same pitch with which the sound was triggered. Then, without knowing which pitch to produce, Tyndall would produce an oscillatory, siren-like sound. When the

correct pitch was produced, no matter how briefly, the flame would begin singing and shaking. In his later work, Tyndall[28] showed that varying the length of the tube used would result in differently pitched tones, and that the corresponding "vibrations of the flame consist of a series of partial extinctions and revivals of the flame."[28] With large tubes, the intensity and volume of the sound was such that it caused physical vibration within the room, and sometimes resulted in "the flame [being] extinguished by its own violence, [ending] its peal by an explosion as loud as a pistol-shot."[28] Although not designated as such at the time, Higgins,[25] Rijke,[26] and Tyndall[27,28] were among the first to inspect the effect of thermoacoustic phenomena and their relation to combustion instability.

2.2.2 Characterization of the Instability

Although scientists of the nineteenth century attempted to explain the thermo-acoustic phenomena, it was not until 1945 in which the mechanism by which heat release and the excitation of acoustic waves was characterized. In qualitatively defining the coupling between local pressure and heat release oscillations, Lord Rayleigh stated:

> If heat be periodically communicated to, and abstracted from, a mass of air vibrating (for example) in a cylinder bounded by a piston, the effect produced will depend upon the phase of the vibration at which the transfer of heat takes place. If the heat is given to the air at the moment of greatest condensation, or be taken from it at the moment of greatest rarefaction, the vibration is encouraged. On the other hand, if heat be given at the moment of greatest rarefaction, or abstracted at the moment of greatest condensation, the vibration is discouraged.[29]

In other words, the observed instability is dependent on the relationship between heat release oscillations and local pressure oscillations. Energy is added to the acoustic field and vibrations are encouraged when heat is added (removed) when the local pressure of the gas is above (below) the mean pressure in the system. That is to say, energy is added

to the acoustic field when the phase difference between the heat release and pressure oscillations is less than $\pi/2$ (in phase heat release/pressure fluctuations). Similarly, and conversely, energy is removed from the acoustic field and vibrations are damped when the phase difference between the heat release and pressure oscillations is greater than $\pi/2$ (out of phase heat release/pressure fluctuations). In the system Rayleigh proposes, this occurs when heat is added to (removed from) the system as the local pressure is below (above) the mean pressure of the system.

Putnam and Dennis[30] theoretically investigated the criterion using a heat-driven wave equation that resulted from a derivation utilizing the perfect gas equation, continuity, linear momentum, and energy conservation. With this thermodynamic analysis, they demonstrated the validity of Rayleigh's criterion. Ultimately, Putnam and Dennis derived the first mathematical formulation of the criterion presented by Rayleigh using the relationship between heat release and pressure oscillations, as shown in Equation 2.15.[31]

$$\int_0^T p'q'dt > 0 \tag{2.15}$$

To include effects of boundary conditions, Chu[32] expanded on Putnam and Dennis'[31] Rayleigh integral. Fundamentally, Chu's formulation is a linear equation that describes the fluctuation of acoustic energy within the system, specifically for cases of low amplitude oscillations in gases with a constant specific heat ratio. In verifying Rayleigh's criterion, Chu's formulation explains that for amplification to occur, the net mechanical work done by the gas must be greater than the acoustic losses due to viscous dissipation. Additionally, Chu's formulation illustrates a temporal relationship between the relevant oscillations and assumes that the mean entropy of the flow is spatially uniform. However, the pressure and heat release oscillations are also spatially dependent

in real systems, as reflected in Zinn's[33] formulation of the Rayleigh criterion (Eq. 2.16), which takes the volume of the system, V, into account.

$$\int_V \int_T p'(x,t)\, q'(x,t) dt\, dV \geq \int_V \int_T \sum L_i(x,t)\, dt\, dV \tag{2.16}$$

Unlike Putnam and Dennis'[31] Rayleigh criterion (Equation 2.15), Zinn's[33] formulation better reflects a real process by using a spatially- and temporally-dependent term— $L_i(x,t)$, as shown on the right-hand side of Equation 2.16—to represent the ith damping process. In other words, the acoustic losses present in real systems are reflected in Zinn's Rayleigh criterion. Examples of damping processes include: heat release, acoustic radiation, and viscous dissipation.

Nicoud and Poinsot[34] also included effects of acoustic losses in their formulation of instability criterion. They began with a derivation of an acoustic energy equation (see Equation 2.17), from which they formulated their acoustic energy criterion, seen in Equation 2.18. Essentially, Nicoud and Poinsot's acoustic energy criterion shows that for stability, the amplification of acoustic energy within the system must be greater than losses as a result of acoustic fluxes at the system boundaries, S.

$$\frac{\partial}{\partial t}\int_V \frac{1}{2}\left(\bar{\rho}\,\vec{u}^2 + {p'^2}/{\bar{\rho}\bar{c}}\right) dV = \int_V \left({\gamma - 1}/{\gamma\bar{p}}\right) p'q'dV - \int_S p'\,\vec{u}\cdot d\vec{S} \tag{2.17}$$

$$\int_V \left({\gamma - 1}/{\gamma\bar{p}}\right) p'(t)\, q'(t) dV > \int_S p'\,\vec{u}\cdot d\vec{S} \tag{2.18}$$

However, the acoustic energy relations (Eq. 2.17, 2.18) are only valid for isentropic flows. For any real system, entropic losses would also need to be included in

the prediction of instability. With Gibbs relations, the continuity equation, and the state equation, Nicoud and Poinsot then derived the "fluctuation energy equation"—see Equation 2.19—that includes effects of an irreversible flow field containing linear entropy fluctuations with the initiation of instability. From this point, Nicoud and Poinsot developed the instability criterion shown in Equation 2.20 for real, irreversible flows. These two equations are also capable of describing isentropic flows. In this case, Equations 2.19 and 2.20 would reduce to Equations 2.17 and 2.18, respectively.

$$\frac{\partial}{\partial t}\int_V \frac{1}{2}\left(\bar{\rho}\,\vec{u}^2 + \frac{p'^2}{\bar{\rho}\bar{c}} + \frac{\bar{p}s'^2}{Rc_p}\right)dV = \int_V \left[\frac{T'q'}{\bar{T}} - \frac{\bar{p}s'^2}{Rc_p}\vec{u}\cdot\nabla\vec{s}\right]dV - \int_S p'\,\vec{u}\cdot d\vec{S} \quad (2.19)$$

$$\int_V \left(\gamma - 1/\gamma\bar{p}\right)p'(t)\,q'(t)dV > \int_S p'\,\vec{u}\cdot d\vec{S} \quad (2.20)$$

The instability criteria developed by Nicoud and Poinsot[34] (Eq. 2.18 and 2.20) apply to systems in which the thermoacoustic oscillations are linear. However, Culick[35] has verified the Rayleigh criterion through a mathematical derivation that is applicable to both linear and nonlinear thermoacoustic oscillations. In his derivation, Culick assumes an arbitrary shape for the combustion chamber, leading to the verification of the Rayleigh criterion for all thermoacoustic oscillations and all combustion chambers; Culick's Rayleigh criterion is shown in Equation 2.21. This work provided an analogy between the effects of an oscillating heat source and the effect of an oscillating piston in wave generation, and increased the understanding of the effect of q' and dq'/dt on the amplification of acoustic waves.

$$\Delta E = \int_V \int_t^{t+T} \left(\gamma - 1 \Big/ \gamma \bar{p} \right) p'(t)\, q'(t)\, dt dV \tag{2.21}$$

For a more complete, comprehensive review on literature related to combustion instability and Rayleigh's instability criterion, the reader is referred to Raun et al.'s "A Review of Rijke Tubes Rijke Burners and Related Devices."[36] In this review, Raun et al. covers literature related to the history and theoretical mechanisms of heat-driven acoustic instability. Modern experimental work with Rijke tubes and burners is also discussed, including experimental work conducted by Putnam and Dennis between 1953 and 1956 when they published their initial mathematical description of the Rayleigh criterion.

2.2.3 Types of Instability

Because of the work performed by Barrère and Williams[37] and Putnam,[38] combustion instabilities can be classified based on the size of the components that are involved in the instability. Small-scale instabilities, or intrinsic instabilities, are caused by short distance interactions between chemical kinetics and the flow field. Based on the relative rates of the molecular diffusion of reactants and the thermal diffusion of heat, the thermal-diffusive instability is one example of an intrinsic instability. Combustion instabilities due to the interaction of the flame front and vorticity in the shear layer are known as chamber instabilities, which can be further classified as acoustic instabilities, shock instabilities, or fluid-dynamic instabilities.[37] The Darrieus-Landau instability, or hydrodynamic instability, falls within the category of fluid-dynamic chamber instabilities. Acoustic instabilities involve the propagation of acoustic waves within the combustion chamber. If paired with the heat release oscillations produced by the flame, like those observed by Higgins,[25] Rijke,[26] and Tyndall,[27,28] these acoustic instabilities are

specifically known as thermoacoustic instabilities. The final classification, system instabilities, is where large-scale, combustor-level instabilities are categorized. Because thermoacoustic instabilities have already been discussed, the two modes that will be discussed are the Darrieus-Landau instability and thermal-diffusive instability.

2.2.3.1 Darrieus-Landau (Hydrodynamic) Instability

Between the unburned gases (reactants) and the burned gases (products) in a flame, a large density gradient exists, giving rise to baroclinic effects on the flame front. As it is defined, baroclinity is due to misaligned gradients of density and pressure, resulting in the rotation known as baroclinic torque. This large density gradient is inherently tied to the increase in temperature—and the interrelated expansion of the gas—as the combustion reaction proceeds. Small perturbations, including those arising from baroclinic effects, can significantly influence the geometry of the flame front, especially through the formation of wrinkles.

In the case of a laminar, premixed planar flame, any gradients of temperature and species concentration occur normal to the flame. Using the temperature of combustion and the thickness, velocity, and thermal diffusivity of the flame, Zel'dovich and Kamenetzki[39] developed a mathematical description for characteristics of laminar, freely propagating planar flames. For a wrinkled flame, however, the behavior of the flame is dependent on the diffusive and convective transport of energy and mass. The combustion does not have a direct impact on the geometry of the flame front, but results in the convective displacement of the front. The expansion of the gas and conservation of mass and momentum require that the streamlines change direction at the flame front. In concave regions (relative to the reactants), the downstream streamlines curve toward the flame front, while the upstream streamlines bend away from the front. Conversely, the downstream streamlines bend away from the front in convex wrinkling regions, while the

upstream streamlines curve toward the flame front. Because the Mach number for their flames was relatively small, Darrieus[40] and Landau[41] were able to classify their flow as quasi-incompressible. Then, deviation in the streamlines across the flame front will influence the upstream flow field. The modification of the upstream flow field creates flow divergence and velocity gradients that in turn, couple back and increase the wrinkling of the flame front.[42] This feedback mechanism and resulting (unconditional) hydrodynamic combustion instability is designated the Darrieus-Landau instability. Sometimes, it is simply referred to as the hydrodynamic instability.

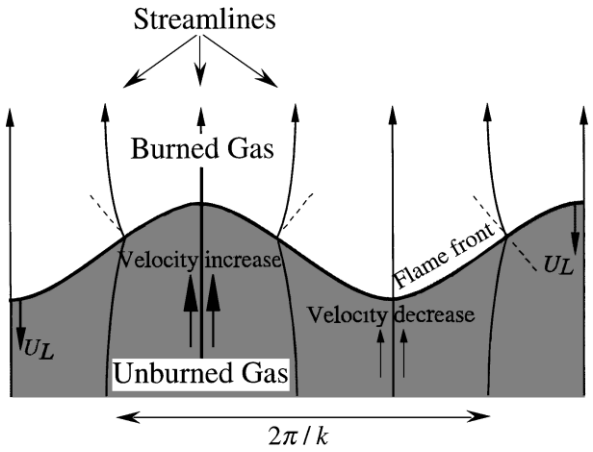

Figure 2.6: Deviation of flow lines leading to Darrieus-Landau combustion instability

Source: [42]

As anticipated by Darrieus and Landau, the problem of analytically characterizing the structure of a non-steady wrinkled flame (with hydrodynamic instability) can be approached as an incompressible-flow problem outside the flame thickness by specifying boundary conditions on either side of the flame front.[43] Although Markstein presented a

phenomenological description of the wrinkled front[44] and Zel'dovich et al. discussed the hydrodynamics and stability of flame propagation in tubes,[45] it was Sivashinsky[46] and Joulin & Clavin[47] who provided full descriptions of the structure of the wrinkled flame front. These descriptions were attained by solving the thermal-diffusive instability model proposed by Barenblatt et al..[48] With more developments in the field, Sivashinsky paired with Gutman[49] to continue examining hydrodynamic flame instability. Together, the two examined the geometries of a downward-propagating planar flame under the influence of the Darrieus-Landau instability. In smaller combustion systems, Gutman and Sivashinsky showed that although small-scale instability cells may initially form in the planar front, they will eventually merge until a single cusp-shaped flame is formed, as shown in Figure 2.7.

In large-scale combustion systems, however, Gutman and Sivashinsky[49] showed that the instability presents as fine cellular structures that constantly develop, merge, and divide. As time progresses, this chaotic nature continues, and one overall structure (as in Figure 2.7) does not develop.

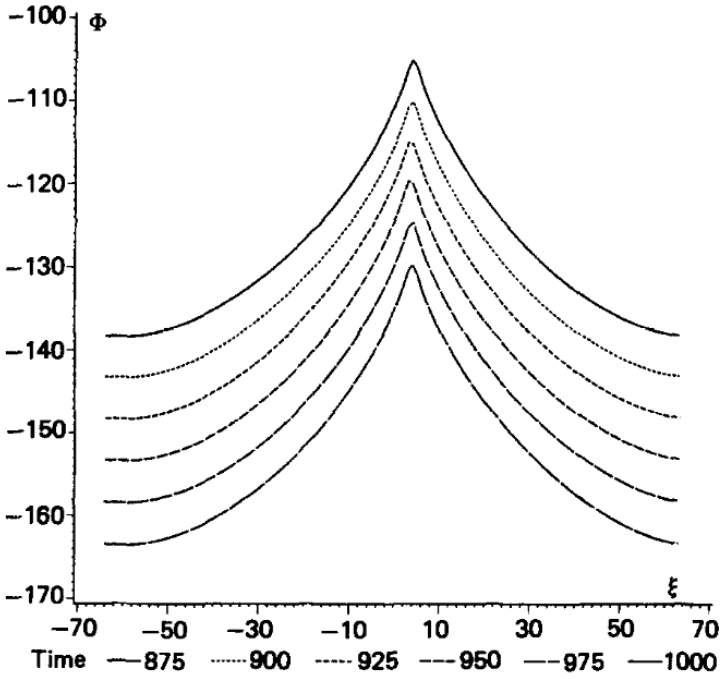

Figure 2.7: The amplification of a small-scale combustion instability along a planar flame front forms a cusp-shaped flame.

Source: [49]

2.2.3.2 Thermal-diffusive Instability

If the thermal expansion of gases across the flame front were neglected, then theoretically, the Darrieus-Landau instability caused by this expansion would not be observed. Even in the absence of hydrodynamic effects, however, combustion instability may still be observed. In premixed flames, for example, thermal-diffusive instabilities are intrinsic to the nature of the flow field. The instability is dependent on the relationship

between the molecular diffusion of the reactants and the thermal diffusion of heat, which can be expressed in terms of the Lewis number, which is defined in Equation 2.11.

A simple examination of the physics behind the Lewis number can provide information on the nature of the stability of the flame. If equal to unity, the mass and thermal diffusion rates are equal, and the surface of the flame front is unaltered. If not equal to unity, however, two cases provide stability information for the flame: those in which $Le > 1$ and in which $Le < 1$. A depiction of the physical mechanism associated with these regimes is shown in Figure 2.8.

For cases in which the Lewis number is less than unity, the rate of thermal diffusion is lower than the rate of molecular diffusion of the reactants. As such, in regions of the flame front that are convex toward the unburned reactants (UR in Figure 2.8), the reactants diffuse toward the burnt gases (BG) faster than heat diffuses toward the BG. Then, as reactants diffuse, they are heated by the BG and proceed through the combustion more quickly than in the case of a planar flame front. In turn, this results in an increased local (laminar) flame speed, s_L, for regions convex toward the UR (compared to s_L^0, the flame speed of a planar flame front). Conversely, in zones that are concave to the UR, the reactant molecules diffuse outward toward the BG side of the flame front. Then, compared to the planar flame front, the larger potential for outward diffusion (without encountering another portion of the flame front) results in a decreased local flame speed. Then, for $Le < 1$, the integration of thermal-diffusive effects in the different regions of premixed flames amplifies perturbations and results in an unstable, increasingly wrinkled flame.[24,50,51]

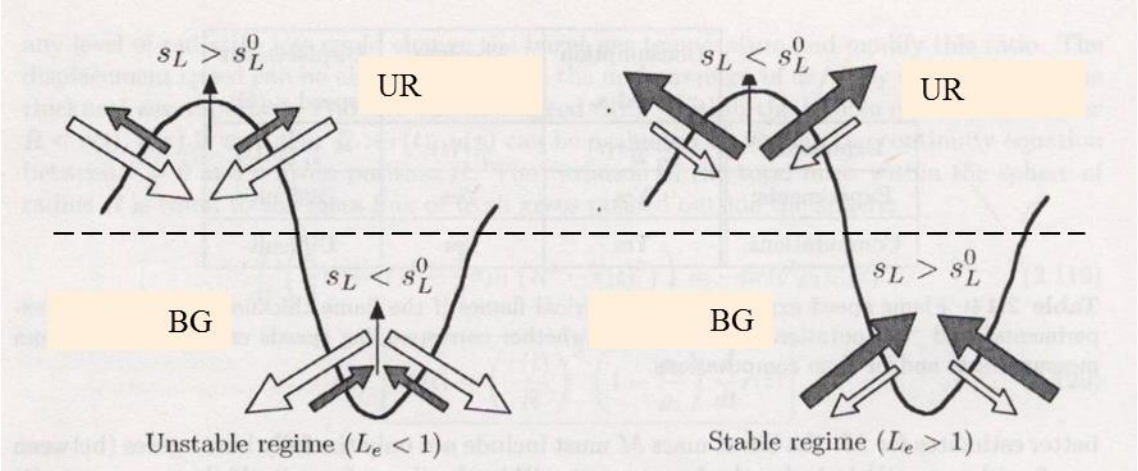

Figure 2.8: Depiction of (Le-dependent) thermal-diffusive instability regimes

---

Adapted from: [24]
The dashed line represents the planar flame front, while "UR" and "BG" represent the unburned reactants and the burnt gases, respectively.

"For Le < 1, molecular diffusion (empty arrows) is larger than heat diffusion (filled arrows) and the wrinkling of the flame front is enhanced by differential flame speeds (left figure). For Le > (right figure), a stable planar flame is obtained."[24]

In a similar fashion, the effect of a Lewis number greater than unity on a flame front can be determined. For this case, the rate of thermal diffusion by heat is dominant to that of the mass diffusion of the reactants. In regions that are convex to the UR, the thermal diffusion by heat can occur in large outward-oriented zones and compared to the planar flame speed, and the local flame speed is decreased. In regions that are concave to the UR, the diffusive heat will increase the temperature of the reactants, and the local flame speed will be higher than that of the planar flame speed. Then, for $Le > 1$, the higher relative rate of thermal diffusion (by heat) acts to stabilize the front by smoothing flame wrinkling and decreasing the overall surface area of the flame.

In this simple stability analysis, it was assumed hydrodynamic effects on the stability of the flame were negligible. This, of course, is not true for actual flames. In their analysis, both Barenblatt et al.[48] and Williams[52] determined stability limits that took both the thermal-diffusive and hydrodynamic instability effects into consideration. For both analyses, the authors' stability conditions do not revolve around $Le = 1$, but are instead dependent on the value of the Lewis number compared to an arbitrary critical Lewis number, Le_c. In Barenblatt's analysis of a planar flame front influenced by long-wave perturbations, the critical number (defined in Equation 2.22) was shown to be dependent on the Zeldovich number, β, which is dependent on the temperature of the burned gases (T_{BG}), the temperature of the unburned reactants (T_u), and the reactions' activation energy (E), as shown in Equation 2.23.

$$Le_c = 1 - {}^{2}/_{\beta} \tag{2.22}$$

$$\beta = {}^{E(T_{BG} - T_u)}\Big/_{RT_{BG}^2} \tag{2.23}$$

For a typical flame, the second term in Equation 2.22 is approximately 0.133. Then, the critical Lewis number for a typical flame is approximately 0.877. In most flames, the Lewis number is near unity. Depending on the composition, this is also true in some mixed-fuel flames. For example, the Lewis number is approximately unity for a flame using a methane and hydrogen as the fuel source. However, as the ratio of methane to hydrogen decreases—that is, with increasing the relative fraction of hydrogen in the mixed fuel—the Lewis number is reduced, and the potential for thermal-diffusive instabilities in the system develops.[17,53]

Following Sivashinsky's[46] analysis of thermal-diffusive theory of single-reactant, cellular flames, Joulin & Mitani[54] considered the linear stability of a two-reactant flame, which is governed by perturbations of temperature and the predominant component in the fuel mixture. The stoichiometry and the Lewis numbers of the two components are important in determining the stability characteristics for two-reactant flames. Although the authors show that the stability of two-reactant flames is governed only by a single parameter, the interrelatedness of defining this parameter to other characteristics of the flame is such that the reader is referred to Joulin and Mitani's "Linear Stability Analysis of Two-Reactant Flames"[54] for the complete derivation of the stability conditions. Within their analysis, they showed that for a given Lewis number and stoichiometric ratios, their stability condition can be reduced to resemble exactly that derived by Sivashinsky[46] for single-reactant flames. In both analyses, the authors showed that as the Lewis number (or reduced Lewis number, as in Joulin & Mitani) is sufficiently small, the instability presents in cellular structures within the flame.

2.2.3.3 Blowout

At sufficiently low fuel/oxidizer flow rates, the base of a flame will lie relatively close to the exit of the burner. However, as the flow rate of the incoming gases is increased, the flame lifts away from the burner until the rate of combustion cannot maintain the rate at which unburned reactants are entering the region in which the combustion occurs. As the incoming flow rate (and thusly, bulk velocity) becomes sufficiently high, the flame is said to experience blowout.[18] Ultimately, blowout is a mechanism resulting in flame extinction, and is not desirable in combustion systems.

However, blowout is not solely dependent on the relationship between the rate of combustion and the incoming reactant mixture flow rate. For combustion in industry and in the current work, operating under sufficiently fuel-lean conditions ($\phi < 1$) may result

in flame failure. In this situation, there is not enough fuel in the fuel/oxidizer mixture for the flame to self-sustain. With a decreasing equivalence ratio, ceteris paribus, regions of stability related to lean blowout are easy to observe in a low swirl burner. For example, in the current work, stable flames remain relatively stationary in relation to the exit of the burner. With a decrease in equivalence ratio, however, a region of instability exists in which the flame boucnes. Here, the flame is characterized as unstable, but extinction has not yet occurred. As the equivalence ratio is decreased further, however, the flame will either shoot upward or extinguish due to its inability to self-sustain. The equivalence ratio at which this blowout occurs is known as the lean blowout (LBO) limit, and is influenced by fuel type, flow velocity, system pressure, and burner geometry. Details regarding the LBO limit will be addressed further during discussion of hydrogen addition to the fuel mixture as a method of stabilizing flames.

2.2.3.4 Flashback

Flashback is the transient phenomenon that occurs when a flame enters and propagates through a burner without extinction. Compared to blowout, which results in flame extinction, flashback is a serious safety hazard. Without precautions or flame arrests in place, flashback can result in the flame propagating through the fuel supply line to the fuel reservoir, which may result in an explosion.[18] Like blowout, flashback is influenced by fuel type, flow velocity, system pressure, and burner geometry. For example, as the flow velocity is decreased, the rate of combustion—and hence, the flame speed—may exceed the local velocity of unburned reactants, resulting in flashback of the flame. Fritz, et al.[55] highlighted the four principal causes of flashback:

- flashback in the boundary layer
- turbulent flame propagation in the core flow
- flashback due to combustion instabilities
- combustion induced vortex breakdown (CIVB)

Predominant in nonswirling, low turbulence flows, flashback in the boundary layer is due to low flow velocities in the boundary layer of the flow, which promote upstream flame propagation. Additionally, heat transfer to the walls of the combustor can also result in flame extinction. Lewis and von Elbe[56] derived flashback criterion for laminar flows based on the laminar flame speed and the distance required for flame quenching. Based on their criterion, flashback occurs if the gradient of velocity is less than the ratio of the laminar flame speed to the quenching distance. In turbulent flows, however, the axial turbulent diffusion above the laminar sublayer increases the flame speed, so for turbulent flows, the critical velocity gradient for flashback is much higher than in laminar flows.[57] In a recent study, it was concluded that key parameters for determining meaningful turbulent boundary layer flashback limits include the distribution of the flame backpressure and the flame position. Additionally, it was shown that confined flames produced more conservative criteria than unconfined flames in designing burners resistant to turbulent boundary layer-induced flashback.[58]

In the second principal cause of flashback as highlighted by Fritz et al., flashback occurs if the turbulent burning velocity exceeds the local flow velocity in the core flow. This is the mode of flashback highlighted in Turns' Introduction to Combustion.[18] Because the turbulent flame speed is highly dependent on chemical kinetics and flame structure, studies to find correlations between the turbulent velocity fluctuations and the turbulent burning velocity are in disagreement.[59,60,61,62] In swirled flames, flame wrinkling results in a larger flame surface area, resulting in a higher increase from the laminar flame speed to the turbulent flame speed than in non-swirled cases. For swirled

burners, a higher level of protection against flashback is provided in lower-turbulence burners (e.g. LSBs) than in high-swirl burners.[55]

Combustion instabilities, such as those resulting from vortical flame structures or those within the precessing vortex core (PVC) of high swirl flows, can also cause flashback in the boundary layer and/or in the core flow.[10,63] The last mechanism resulting in flashback is associated with the breakdown of vortices in the PVC or recirculating region(s) of the flow. Although many studies have been performed on CIVB-induced flashback,[64,65,66] the current work focuses on flashback limits in a LSB. Because the PVC is not present in LSB flow fields, details of the CIVB mechanism will not be discussed here. For a more detailed explanation of the physics behind flashback resulting from combustion instability and CIVB, the reader is referred to Fritz et al.'s "Flashback in a Swirl Burner With Cylindrical Premixing Zone."[55]

2.2.4 Instigating Instability

In both industrial processes and in experimental systems, observed instabilities may be due to one of many mechanisms, such as the presence of a feedback loop within the system. As illustrated in Figure 2.9, a causal relationship exists between unsteady heat release oscillations, acoustic excitations, and perturbations in the flow field. Within the flow field, fluctuation properties may be thermodynamic or chemical in nature, but will have an impact on the heat release oscillations within the flame. Inhomogeneities within the flow field influence the heat release such that the resulting oscillations are unsteady. From this point, the acoustic field—and thus, the pressure fluctuations—in the chamber is affected by the unsteady heat release oscillations, and in turn, will couple back and change various thermodynamic or chemical properties of the flow field. This feedback loop is only one of many mechanisms that are capable of triggering instabilities within a

combustion system, but essentially is a method of relating the downstream flow to the upstream region where perturbations originate. Another way of altering flame stability is to change the density of the unburned reactants or the mean pressure of the combustion system, which results in modifying the flame speed and/or the acoustic characteristics of the flame. In these cases, the velocity field and acoustic field are reformed, and the stability and flame dynamics of the combustion are altered.

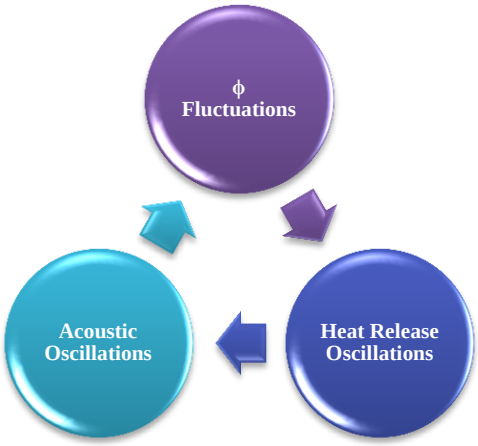

Figure 2.9: Illustration of feedback loop involved in sustainment and amplification of combustion instabilities

Theoretically, variations in equivalence ratio were shown to participate in the feedback loop within a lean, premixed gas turbine system.[67] Variations in the equivalence ratio may be due to an incomplete or an inefficient premixing process or due to unanticipated pressure fluctuations within the fuel/air supply system, which may be due the nature of release patterns from the reservoir. More likely, however, pressure perturbations within the acoustic field will influence the pressure drop and variations within the supply system and alter the flow rate of the fuel or air being supplied.[68]

Experimentally, Kang et al.[69] used a non-premixed jet flame to investigate the relationship between the level of mixing and acoustic fluctuations. The work supported Lieuwen's theoretical work to show that the level of premixing and the local equivalence ratio are influenced by acoustic perturbations, which also have an effect on the flame response.

Another source of flame and acoustic coupling is the formation of vortices, as first evidenced in the early studies of Reynst,[70] who identified "whirls" as a source of combustion instabilities. In sheared zones, hydrodynamic instability can induce vortices. With the introduction of acoustics, the hydrodynamic mode can couple to create vortices that are excited both acoustically and hydrodynamically.[71] Vortices can act to trigger instability through interaction with the flow, leading to small-scale turbulent structures and localized, sudden heat release. On the other hand, the vortices can act to increase the surface area—and as such, the heat release—of the flame. In either case, the vortices completely modify the flow structure and result in an unsteady heat release, which can then instigate the cyclical feedback process depicted in Figure 2.9. The presence of acoustic oscillations may, in fact, actually act to stabilize vortex formation, as evidenced by studies of vortex formation in the shear layer of dump combustors or combustors with bluff-body flame holders.[72]

2.2.5 Rayleigh Index & Maps

From Culick's derivation of the Rayleigh criterion (Equation 2.21), a normalized, non-dimensional parameter was developed that is now commonly used in the modeling of combustion instabilities.[73,74,75,76] This parameter, shown in Equation 2.24, is known as the Rayleigh index. Non-dimensionalizing and normalizing processes were performed in the development of the parameter accounts for the amplitude and period of driving pressure

oscillations. Here, the period of the driving acoustic wave, T, is used to develop the non-dimensional time, ξ.[77]

$$R = \int_0^1 \frac{p'q'}{p_{rms}\,\bar{q}}\, d\xi \tag{2.24}$$

Previously, p' and q' were the pressure and heat release oscillations, respectively. Here, in Equation 2.24, p' is instead the amplitude of driving pressure perturbations and q' is the heat release fluctuation per unit volume. In a similar fashion, p_{rms} is the root mean square of the amplitudes of driving pressure oscillations and $\bar{q}$ denotes the mean intensity of heat release.

With Lord Rayleigh's criterion, knowing the relationship between the heat release and pressure oscillations gives insight into the type of combustion instability observed. With the Rayleigh index, the sign convention is indicative of the type of combustion instability. Positive indices are obtained if the acoustic energy within the flame is amplified, and negative indices indicate that the acoustic vibrations are damped by the driving perturbations. In the examination of thermoacoustics, the Rayleigh index can be used to explore flame response for combustion systems. For example, Allison et al.[78] uses the Rayleigh index to examine the thermoacoustics of a flat and a V-shaped syngas flame produced by a simple dual-swirl burner. Huang and Ratner[75,79] and Kang et al.,[74] however, used the Rayleigh index to examine the flame response of acoustically forced bowl-shaped methane flames produced by laboratory scale low-swirl burners. In addition to the ability to examine local flame response, the Rayleigh index can also be applied globally to determine the overall stability of the flame. To obtain the global index, the local, Rayleigh index (from Equation 2.24) is integrated over the volume of interest. The global Rayleigh index has been utilized by many, including Poinsot et al.[80] to verify the Rayleigh criterion for a multiple inlet combustor system. A numerical investigation by

Shinjo et al.[81] utilized the global Rayleigh index to validate a large eddy simulation approach to modeling unsteady methane-air flames produced by a gas turbine swirl burner. Huang and Ratner[75,79] and Kang et al.[74] utilized the global Rayleigh index in their examination of 2.54 cm low swirl burners.

As the insertion of a thermocouple (or other physical device) into a combustion chamber is bound to alter the flow field, planar laser-induced fluorescence—a non-intrusive technique which will be discussed in more detail during the review of imaging techniques—of OH^* can be used to visualize the flame and assist in the formulation of the Rayleigh index for experimental combustion systems. As an intermediate product of combustion, the concentration of OH, [OH], is an approximate measure of the local temperature in the flame, and as such, can be used as a relative indicator of heat release.[82,83,84] The definition of the Rayleigh index retains the same form but can instead be written as shown in Equation 2.25.

$$R = \int_0^1 \frac{p'[OH]'}{p_{rms}\,\overline{[OH]}}\, d\xi \tag{2.25}$$

As in Equation 2.24, p' is the amplitude of driving pressure perturbations and p_{rms} is the root mean square of the amplitudes of driving pressure oscillations. Instead of using $q'/\bar{q}$, however, the ratio of heat release fluctuations to mean heat release is approximated by $[OH]'/\overline{[OH]}$, the ratio of OH concentration fluctuations to the mean OH concentration.

2.3 Flame Stabilization

Although combustion instabilities have been extensively studied in laboratory settings, the presence of instability in industrial combustors must be avoided. The current section will begin by discussing the motivation for avoiding combustion instability, and will then continue to discuss methods that can be used in reducing the presence of instability. The three main methods that will be discussed include active and passive control, the addition of swirl, and the addition of hydrogen to the reactant fuel mixture.

2.3.1 Motivation for Stabilization

In industries that utilize continuous combustion, such as propulsion, power generation, and heating, the appearance of combustion instability is an obstacle that should be avoided for safety purposes and failure prevention. In the gas power industry, biannual (seasonal) maintenance and tuning may be necessary to counteract the effect of ambient temperature changes on incoming fuel/air density and the lean stability limits of the combustor.[85] As previously discussed, instability can cause circumstances in which flashback or blowout can occur, and instability can be preserved and magnified by the cyclic feedback process outlined in Figure 2.9. From a mechanical or thermal fatiguing standpoint, other consequences can result from the onset and proliferation of combustion instability. As one side effect, instabilities can cause localized overheating and fatiguing, which precipitates equipment failure. Within the combustor, the buildup of acoustics can cause unwanted vibrations.[86] In cases where the amplitude of pressure oscillations is sufficiently large, components of the combustor may physically deform. In both of these cases, the rate of fatigue failure is also accelerated. Examples of specific components risks are shown in Table 2.1, and are classified by the type of instability (dependent on oscillation frequency) by which they are caused. Visually, Figure 2.10 shows the

difference between an intact (non-premixed, jet-type) burner assembly and an assembly that has been affected by combustion instability. As evidenced by these examples, the presence and propagation of thermoacoustic instability in industrial systems will eventually lead to failure. In the most severe cases, instabilities can result in system failure occurring in the form of an explosion.

Table 2.1: Potential risks associated with the presence of combustion instability

Description	**Frequency Range [Hz]**	**Component Risks**	**Potential Causes**
Low-frequency dynamics	0-100	• Swirler damage • Basket damage • Nozzle damage	• Flashback indications • Lean blowout • Damaged swirler(s) • Air-flow restriction • High injection flow rates • Pilot-nozzle distress
Intermediate-frequency dynamics	100-500	• Transition panels • Transition seals • Fretting • Wear	• Fuel composition • Fuel splits • Bypass-valve distress
Intermediate-frequency dynamics	500-1500	• Downstream components • Fretting • Wear	• Equipment distress
High-frequency dynamics	500-5000	• Baskets • Cross-flame tubes • Flashback thermocouples	• Over-firing • Fuel composition • System damping • Basket distress

Adapted from [85]

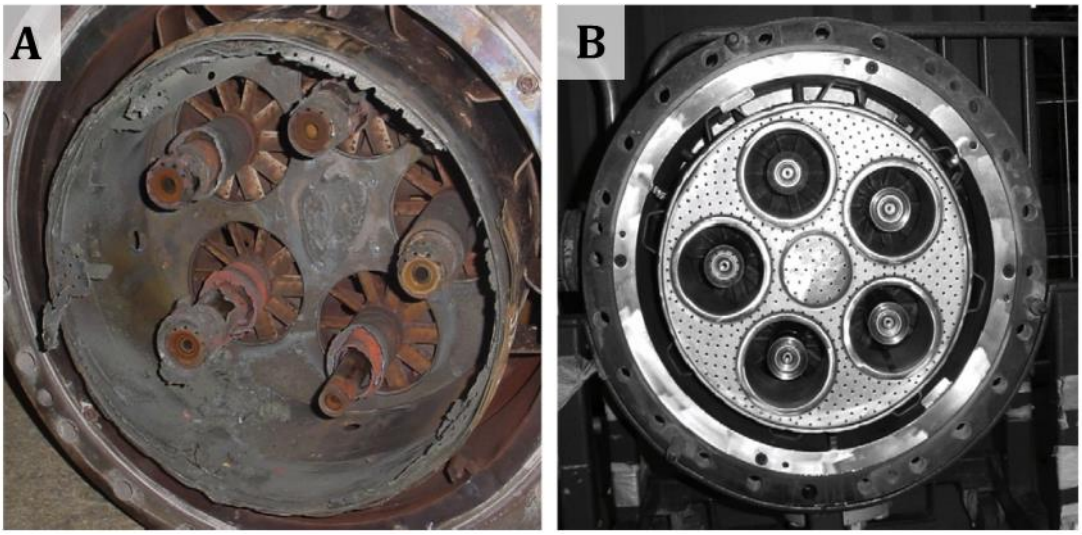

Figure 2.10: Potential effects of combustion instability in a non-premixed jet flame combustor

Adapted from [87]
(A) Assembly exposed to combustion instability
(B) Fresh burner assembly

2.3.2 Methods of Stabilization

To effectively preclude the formation of instability or its presence in a combustion system, the system should be altered such that the system is prevented from entering the instability feedback loop (as in Figure 2.9) or altering the system to interrupt an existing feedback loop. Then, managing instability in a system can be performed by counteracting acoustic oscillations or modifying the flow field to hinder the formation of vortices or alter the heat release pattern. For example, viscous dissipation or heat transfer could be used to transfer acoustic energy to/from vortical disturbances or entropy disturbances, respectively. Energy from acoustic waves can be dissipated through boundary layer losses near rigid surfaces[88] or from flow separation losses at sharp edges or in cases of

rapid expansion.[89] With a reduction in acoustic energy, the feedback loop may not have the level of energy required to sustain the cyclical instability amplification process. In some cases, multiple solutions exist to mitigate combustion instability within a system. For example, Table 2.2 demonstrates potential strategies for dealing with the risks associated with combustion instability that were initially presented in Table 2.1. The present commentary on stabilization strategies will continue with discussion of three areas of stabilization: active and passive control, addition of swirl to the flow field, and addition of hydrogen to premixed fuel blend.

Table 2.2: Strategies used in mitigating risks combustion instability

Description	Potential Causes	Mitigation Strategies
Low-frequency dynamics (0-100 Hz)	• Flashback indications • Lean blowout • Damaged swirler(s) • Air-flow restriction • High injection flow rates • Pilot-nozzle distress	• Increase fuel fraction at different stages • Repair/replace basket • Remove air-side obstructions • Reduce injection flow rate
Intermediate-frequency dynamics (100-500 Hz)	• Fuel composition • Fuel splits • Bypass-valve distress	• Combustion tuning • Active tuning
Intermediate-frequency dynamics (500-1500 Hz)	• Equipment distress	• Inspect and repair combustor components
High-frequency dynamics (500-5000 Hz)	• Over-firing • Fuel composition • System damping • Basket distress	• Install Helmholtz resonators • Increase stream injection • Preheat fuel

Adapted from [85]

2.3.2.1 Active Control vs. Passive Control

In attempts to alleviate destruction in combustion systems, the techniques typically employed to inhibit the damaging effects of thermoacoustic instability can be classified as either passive control or active control. In passive control, instability is suppressed in such a way that the method of control does not continuously alter parameters related to the physics of combustion. For example, passive control may be achieved through modifications to the geometry of the combustion chamber or by presetting properties of the combustion, such as the equivalence ratio or the fuel-to-air ratio of the reactants. In determining modifications required for instability suppression, passive control methods require a basic understanding of the specific physical phenomena occurring in the system.[90] In examining passive control as a NO_x reduction technique, Delabroy et al.[91] altered the configuration of the air and fuel nozzles in a non-premixed system with the goal of attaining homogeneous mixing of the incoming fuel/oxidizer mixture prior to ignition. In typical systems, the air jets are positioned concentrically around the fuel ports. For the new arrangement, alternating air and fuel jets were arranged on a base circle, and were oriented such that axes of all jets were directed away from the axis of the burner. Each type of jet had a constant tilt angle (predetermined by Sobiesiak et al.),[92] but the tilt angle of the air jets differed from that of the fuel jets. In this examination, Delabroy et al.[91] found that the tilt angles of the ports had an effect on the combustion stability, but that the level of NO_x production was relatively unaffected. Using a pulsed combustion active control system, however, Delabroy et al. was able to reduce the NO_x produced in the non-premixed combustion process.

Although there are many types of active control systems, this method of instability suppression can be generally described as a dynamic control system that is usually based on external control loops and adaptive filtering techniques. That is, in active control, manipulations are constantly being applied in attempts to suppress instability. Early work in active control systems was performed by Tsien,[93] Marble and

Cox,[94] Marble,[95] and Crocco and Cheng[96] in analyses of rocket motor instabilities and the introduction of external perturbations to decouple the physical processes responsible for instabilities.[90] Compared to passive control systems, active control is advantageous because the system(s) can be integrated into any existing arrangement to provide stability control, where passive systems may require more construction-based modifications to the existing arrangement.[91] As previously mentioned, Delabroy et al. successfully reduced NO_x production levels in a non-premixed system by means of pulsing the air entering the chamber. Many others have also used pulse combustors as a means of controlling combustion instability, as they have been shown to produce high combustion and thermal efficiencies, promote better combustion intensity, and reduce NO_x, CO, and soot emissions for a variety of fuels.[90,97] Pulse combustors are typically comprised of a large combustion chamber that acts as a Helmholtz resonator and a long tube. Oscillations within the chamber occur at the fundamental frequency of this tube.[90] Examples of some pulse combustor configurations are shown in Figure 2.11. In chamber configurations shown in Figure 2.11a – Figure 2.11d, the large amplitudes of velocity oscillations within the long tube alter heat transfer processes within the combustion chamber. The velocity oscillations cause large flow reversal and shearing motion within the long tube, enhancing the fine-scale turbulence structures of the combustion, which leads to the augmented heat transfer that is observed.[98,99] In Figure 2.11e, however, the twin pulse combustor shown consists of two separate combustion chambers that are connected by a common exhaust volume. Because the chambers operate anti-phase, the pressure pulses from one combustion system cancels with the pressure pulses from the other system, acting to ultimately reduce the noise resulting from the combustion processes.[90,100]

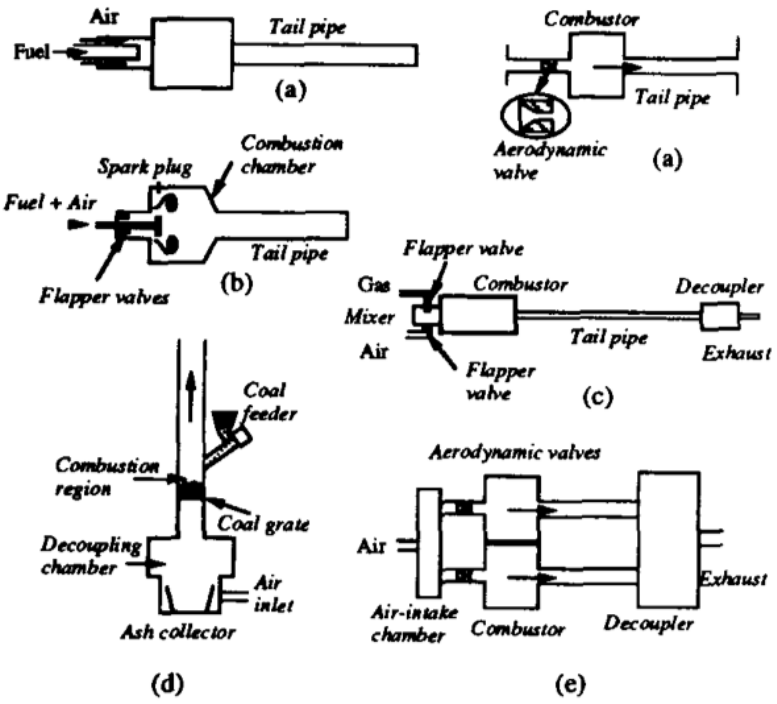

Figure 2.11: Pulse combustor configurations

Adapted from [90]

In non-pulse combustors, others have used a mechanism similar to that of the twin pulse combustor shown in Figure 2.11e to essentially cancel out the presence of acoustics within a combustion chamber. Employing a mechanism known as antisound to suppress combustion instabilities, a loudspeaker is used to produce external acoustic excitations that occur 180° out-of-phase from the actual noise in the chamber.[86,101] In work in a ducted, premixed burner, Lang et al.[86] uses microphones in an active instability control system to experimentally examine the effect of gain and control loop phase on combustion instability. The theoretical model presented is in agreement with experimental work, and shows that if the combustion parameters and active control

parameters are chosen wisely, the energy required to suppress combustion instability is relatively small. Additional experimentation with Rijke tube configurations,[102,103] laboratory reheat channels,[104] small-scale gas rockets,[105] and turbulent diffusion flames[106] further supports observations that active control can be successfully integrated into systems to damp or suppress combustion instabilities.

2.3.2.2 Addition of Swirl

In methods that do not employ active or passive control, changing the dynamics of the flow field can also act to stabilize a flame. One such method of stabilizing the flow field is to swirl the incoming gases prior to ignition. The addition of swirl is the primary mechanism found in both premixed and non-premixed combustion systems because the swirl is effective in controlling flame stability and combustion intensity.[10,107,108,109,110, 111] In premixed, swirled flames, circulation is typically created using vanes to rotate the gases entering the combustion chamber. The level of swirl within the flow field is defined as shown in Equation 2.26, where u_x and u_θ are the axial and azimuthal velocities, respectively, and ρ is the density of the flow, r is the radius of integration, and R gives the outer radius of the annulus.[107,112] Higher swirl numbers correspond to greater circulation within the flow, and conversely, lower swirl numbers correspond to less circulation within the flow. However, as far as swirl classification goes, there is not a specific cutoff to distinguish high swirl flows from low swirl flows. Instead, high swirl flows are characterized by "sufficiently high" swirl numbers, while low swirl flows are characterized by "sufficiently low" swirl numbers.

As incoming gases are circulated in high swirl flows, a toroidal recirculation zone is created at the center of the swirled flow field. By improving the mixing properties of the fuel, oxidizer (in non-premixed systems), and intermediate combustion products, the recirculation zone acts to stabilize the flame. A sample flow field of a high swirl flame is

shown in Figure 2.12. The two important regions that appear within high swirl flames are the central recirculation zone (CRZ) and the precessing vortex core, which is located along the boundary of the CRZ. The role of the PVC in flame stabilization is highly dependent on the nature of the CRZ and the level of swirl within the flame,[113] but can have unfavorable effects on oscillatory heat release patterns and the combustion.[1] However, in premixed systems, the CRZ in known to circulate heat and intermediary combustion products—such as CH and OH radicals—toward the base of the flame, which in turn acts to stabilize the flame in regions where the magnitude of the flame speed and the incoming flow velocity can be equilibriated.[9,10] In this way, the CRZ acts similarly to the wake region of a bluff body flame stabilizer, where a steady supply of radicals and hot combustion products reside to continuously ignite the fresh, unburned reactants.[11]

$$S = \frac{\int_0^R u_x u_\theta r^2 dr}{R \int_0^R u_x^2 r dr} \tag{2.26}$$

In preventing the PVC from adversely affecting the combustion process, the low swirl burner was designed by Robert Cheng of the Lawrence Berkeley National Laboratory to eliminate the formation of the CRZ and in turn, the PVC. Then, because the aforementioned CRZ does not exist, it is not the mechanism that acts to stabilize the flame in low swirl flows. Instead, the design of low swirl burners is such that the flame is stabilized via divergence of the flow field. Figure 2.13 depicts a typical low swirl burner configuration. Here, most of the unburned gases are directed through vanes around the outside of the burner, which act to circulate the flow. Some of the gases are directed axially through screens located at the center of the burner. With increasing downstream distance from the burner exit, the axial flow velocity decreases linearly, which generates the nearly axisymmetric region of flow divergence. Unlike the conventional high swirl burners, LSBs are capable of operating in much leaner regimes, mainly due to the shorter

chemical residence time. With proven lower NO_x production resulting from the leaner combustion regime and the decreased flame temperature, LSBs are an attractive alternative to the high swirl burners that are often used in industry. Additionally, the LSB flow field provides a robust self-adjusting mechanism for the flame to withstand transient flow conditions or unpredicted changes in fuel mixtures.[11] With the leaner combustion regimes, however, the flow field of a LSB is more susceptible to perturbations than the conventional high swirl burner. As previously discussed, these perturbations could alter the combustion process and lead to combustion instability occurring within the system. Experimentation has led to an increased understanding of the LSB combustion physics and related instabilities, but much more work exists in order to declare that the nature of LSB systems are fully understood.

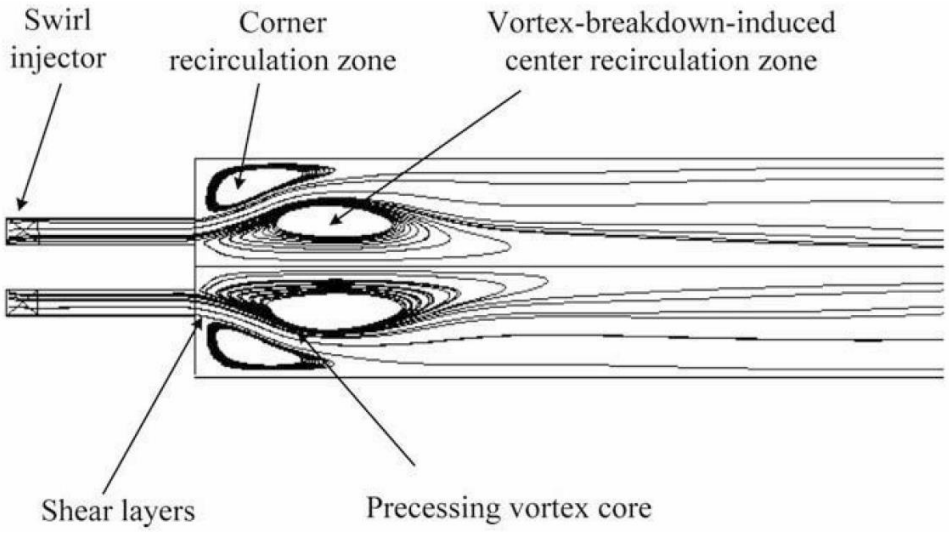

Figure 2.12: Streamlines and flow structures found within a typical high-swirl gas turbine combustor

Source: [114]

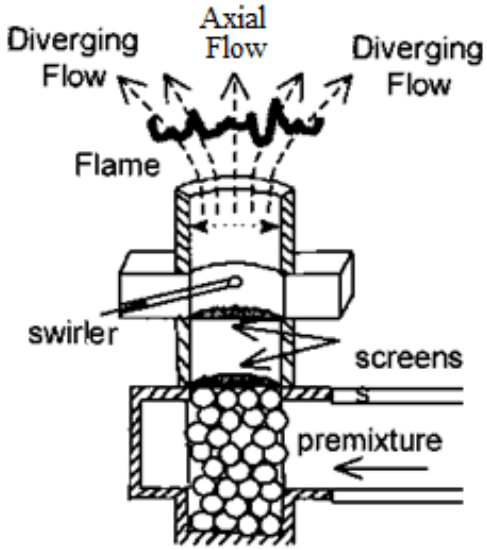

Figure 2.13: Basic geometry and components of a low swirl burner characterized by regions of axial and diverging flow

Adapted from [1]

2.3.2.3 Addition of Hydrogen

With the motivation to decrease NO_x emissions, industry is continuously designing combustion systems to operate under leaner conditions, which are more susceptible to instability. The viability of stabilizing a flame via the addition of hydrogen to the fuel mixture has been examined experimentally at atmospheric and increased chamber pressures, and has been shown to improve extinction limits and NO_x emissions for a variety of fuels.[16,115,116,117,118]

Using a general swirl combustor operating under preheated and premixed conditions, Boschek and Griebel[118] examined the LBO limits for methane and methane-hydrogen fuel mixtures. It was shown that with the addition of hydrogen to the premixed

fuel, the lean stability limit was extended significantly due to a higher OH radical concentration in the mixture. The increased concentration of OH radicals led to a higher global reaction rate and a higher flame speed, resulting in increased flame stability at lower equivalence ratios. Additionally, as the chamber pressure was increased, LBO occurred at lower equivalence ratios. Here, Boschek and Griebel attributed the lower LBO limits at higher pressures to the lower concentration of radicals present within the flame at higher chamber pressures.

Littlejohn et al.[119] examined the effect of hydrogen addition and chamber pressure on the LBO limits of low swirl injectors (LSI) using syngas fuel mixtures composed of hydrogen and one or more of the following components: methane, carbon monoxide, and carbon dioxide. At atmospheric pressure, LBO limits were examined for unconfined laboratory flames generated by a full size (6.35 cm) LSI. At elevated pressures, however, a confined, reduced scale LSI (2.54 cm) was examined instead. In examining the LBO limits of each system, results agreed with those observed by Boschek and Griebel;[118] an increasing fraction of hydrogen in the syngas fuel mixtures resulted in a decrease in the equivalence ratio at LBO. In a similar fashion, Emadi[17] examined the stability and LBO limits in a confined 3.81 cm LSB for methane and methane-hydrogen mixture flames at atmospheric pressure and elevated pressures. Following the general observed trend, increasing the fraction of hydrogen in the mixture fuel resulted in a decrease in the LBO limit. Furthermore, as the Emadi increased the chamber pressure, the LBO limit occurred at leaner conditions, which is akin to the elevated pressure results obtained by Boschek and Griebel. Other studies on the effect of hydrogen addition on flammability limits have been performed, and similar results have been obtained in each case.[116,120,121]

Additionally, many have noted that increasing the fraction of hydrogen in the fuel mixture results in an increase of the laminar and turbulent flame speeds and the associated fuel consumption rates.[15,116,120,122,123,124,125,126,127,128,129] Both the increased range of flammability/stability limits and the increase in flame speed have been attributed

to transport effects, which through a reduction in the Lewis number, play a role in the decreased flame sensitivity to stretching/strain rates for hydrogenated fuel mixtures.[15,116,128,130] Smaller Lewis numbers imply that the rate of molecular diffusion is higher than the rate of thermal diffusion. As a result, the vortices formed at the surface of the hydrogenated flame are relatively weaker and smaller than those in non-hydrogenated flames. Experimentally, both Halter[120] and Emadi[17] indicated that this was the case by examining the effect of hydrogen addition on the flame front curvature, h. In both investigations, an increase in the fraction of hydrogen in the unburned fuel mixture resulted in a broadening of the PDF of flame front curvature, indicating the enhancement of smaller-scale flame front wrinkling. Consequently, the breakdown of the smaller vortices in hydrogenated flames resulted in relatively smaller-scale disturbances to the flow field via localized pressure and heat release fluctuations.[17]

2.4 Imaging Techniques and Flow Field Characterization

In studying the characteristics of combustion fields, a number of approaches exist. However, two of these techniques are of particular importance, as they are the most commonly used in studying lean, premixed combustion systems. In both the PLIF and the chemiluminescence techniques, a special camera is used to filter and photograph regions of a flame at a given instant. Both are useful in examining the characteristics of a flame, but each carries its own set of advantages and disadvantages. When the research of combustion physics was new, chemiluminescence techniques were more commonly used. However, with the increase in technology and clarification of the limitations of chemiluminescence,[77] PLIF techniques are now prevalent in examinations of combustion instability in lean, premixed systems, including naturally unsteady systems and those in which the application of acoustic forcing is used to induce the formation of instability.

Some examples of previous work in oscillatory combustion systems have been sorted by imaging technique and instability associated with the system, and are shown in Table 2.3.

Table 2.3: Studies that have utilized chemiluminescence and PLIF in the examination of oscillatory flames

	Chemiluminescence	PLIF
Naturally Unsteady	• Sterling and Zukoski (1991) (188 Hz) • Broda et al. (1998) (1750 Hz) • Kendrick et al. (1999) (235 Hz, 355 Hz) • Venkataraman et al. (1999) (490 Hz) • Kappei et al. (2000) (370–460 Hz) • Bernier et al. (2004) (400 Hz)	• Cadou et al. (1991) (43 Hz) • Shih et al. (1996) (400 Hz) • Cadou et al. (1998) (328 Hz)
Acoustic Forcing	• Chen et al. (1993) (300 Hz, 400 Hz) • Durox et al. (2002) (0 - 400 Hz) • Schuller et al. (2003) (0 - 400 Hz)	• Cadou et al. (1998) (360 Hz, 420 Hz) • Pun et al. (2003) (22-55 Hz)

Source: [131]

2.4.1 Chemiluminescence

Within chemical reactions, energy is constantly being transferred to and from different species to carry the reaction forward. With this transfer of energy, electrons within the intermediary products may be excited, and move to a higher orbital shell. However, the most stable state in which an electron can reside is the ground state, or the state of lowest electronic energy. Then, as electronically excited species revert to their ground state, energy is typically emitted in the form of electromagnetic energy, which can be captured with cameras that can filter out unwanted wavelengths. The process of

capturing the naturally-emitted electromagnetic energy is known as chemiluminescence. Unlike many other imaging techniques, chemiluminescence relies solely on the natural transmission and emission of energy as the reactants proceed through the combustion process, and does not require an external energy source (e.g. a laser) to excite electrons. These techniques can capture the luminescence of different radical electrons within the flame, including OH^*, CH^*, C_2^*, and CO_2^*,[114] and can provide information regarding the concentration of the aforementioned radical species as well as local air/fuel ratios within the reacting flame. Two examples of chemiluminescence images are shown in Figure 2.14. In the first, OH^*-chemiluminescence was utilized to obtain an instantaneous snapshot of a low swirl burner flame.[17]

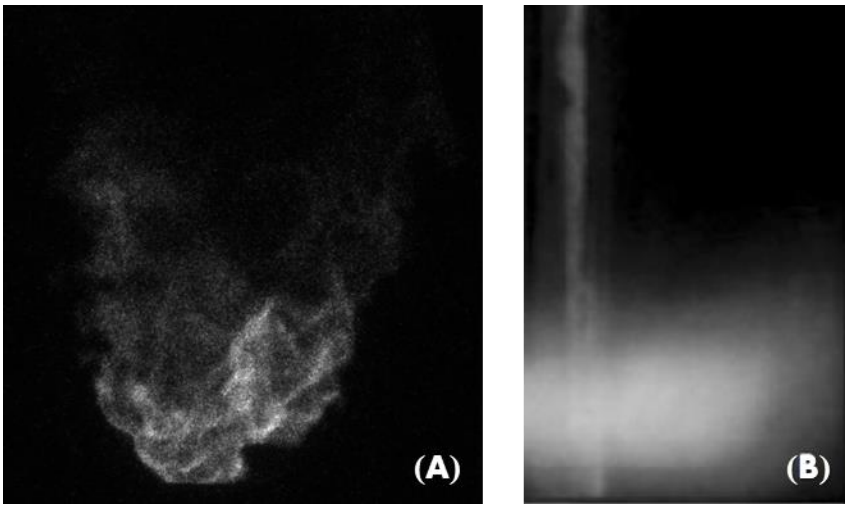

Figure 2.14: Illustration of disparities between an instantaneous and an average chemiluminescence image

(A) Adapted from [17]; image (B) adapted from [78]
(A) Instantaneous OH-chemiluminescence image for a 2.54 cm LSB
(B) Average chemiluminescence image for a flat flame

Chemiluminescence systems can be quickly implemented, and are relatively less expensive than other flame imaging techniques. Images of the flame using chemiluminescence can accurately measure flame oscillatory movement, but due to the spatially averaged nature of images captured with chemiluminescence, detailed internal flame structures cannot be correctly identified. If the Rayleigh index were used in examining structures and flame instability, the spatial averaging through the depth of the flame would result in inaccurate local and global Rayleigh index results.[84] In these cases, if examining internal flame structures, an imaging processes capable of resolving small-scale, internal flame structures should be employed. Additionally, the signal strength of chemiluminescence is not as strong as other flame imaging techniques, which results in a decrease of the temporal resolution of flame visualizations. Then, with a stronger signal, structures within the flame can be resolved for smaller windows of time, increasing the temporal resolution, since shorter integration times would be required to obtain a signal of sufficient strength.[77] One such imaging technique that has the required signal strength and the capability of resolving small-scale structures within the flame is planar laser-induced fluorescence, or PLIF.

2.4.2 Planar Laser-Induced Fluorescence

Unlike chemiluminescence, which cannot resolve small-scale spatial flame structures, PLIF can be used to investigate spatially localized characteristics of the flame. Laser-induced fluorescence (LIF) utilizes a laser system to excite electrons of specific intermediate combustion products, such as OH, CH, CH_2O, or NO. As species return to their ground state, electromagnetic energy is emitted, and can be captured for flame visualization. The intensity of the electromagnetic energy emitted is dependent on the concentration of the species within the flame. The wavelength of the laser beam (for LIF

processes) or laser sheet (for PLIF processes) determines which intermediate species is excited. In past work, an intensified charge-coupled device (ICCD) camera has been used to capture fluorescence in LIF/PLIF processes.[55,74,83,131,132,133,134,135]

Imaging with PLIF can be used in the identification of internal flame structures and the flame's response to acoustic forcing by imaging the concentrations of chemical species within the flame.[83] For example, as previously discussed, the ratio of heat release fluctuations can be predicted by the ratio of OH concentration fluctuations to the mean concentration of OH ($[OH]'/\overline{[OH]}$). Concentration data is collected using PLIF, which can then be used in determining local and global Rayleigh index values to provide insight into thermoacoustic instability within the flame. Examples of an instantaneous and average OH-PLIF image are shown in Figure 2.15a and Figure 2.15b, respectively. With these two images, the fluctuation in concentration of OH ($[OH]'$, see Figure 2.15c) is created. Then, in using a set of the $[OH]'$ images created from the instantaneous images, the Rayleigh index map (Figure 2.15d) is obtained by calculating the Rayleigh index on a pixel-by-pixel basis.

PLIF is a technique that has been used by many, including Driscoll[136] and Emadi,[17] who utilized the imaging process to examine the structure of flames. In Driscoll's work, PLIF images of OH, CH, and CH_2O were used to examine the effect of flamelet structures (e.g. FSD, Σ) on turbulent burning velocities. Emadi, on the other hand, used PLIF to analyze the effect of different flame parameters (fuel composition, chamber pressure, ϕ) on parameters including flame surface density and flame front curvature. In addition to these two studies, PLIF has been used to investigate the dynamics and characteristics of both swirled-flame systems.[16,79,114,133,137,138,139,140] and non-swirled flame systems[77,118,141,142].

In contrast to chemiluminescence imaging techniques, PLIF offers a better temporal resolution due to increased power of the signal and the resulting decreased amount of exposure time required for capturing the PLIF images.[77] In PLIF, the laser

sheet localizes the data collected to the fluoresced plane, while in chemiluminescence techniques, the images collected are line-of-sight spatial averages, so PLIF also offers better spatial resolution than chemiluminescence.[83] Then, the increased temporal and spatial resolutions precipitate the use of PLIF (over chemiluminescence) in examinations involving internal flame structures. However, the main disadvantage to using PLIF over chemiluminescence is the cost associating with purchasing, installing, and running the laser and associated optics equipment.

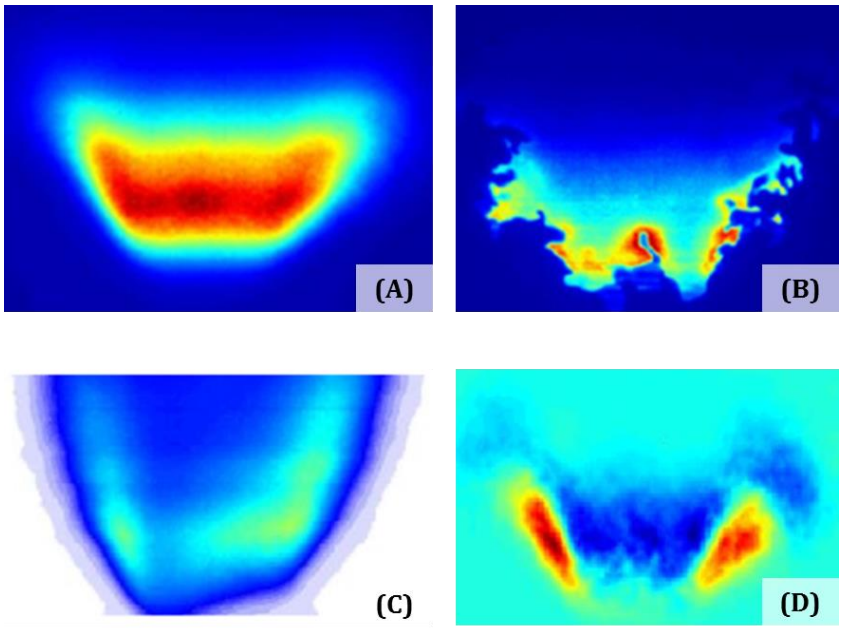

Figure 2.15: Average and Instantaneous OH-PLIF images used to create a sample [OH]' image, and the resulting Rayleigh index map

---

Adapted from [17]
(A) Average OH-PLIF data for a set 900 images for one set of operating conditions
(B) An instantaneous OH-PLIF image
(C) Map for the fluctuation in concentration of OH
(D) Resulting Rayleigh index map

CHAPTER 3

EXPERIMENTAL SETUP

The experimental setup used is an intricate network of components that interact to allow for the collection of data. The entire network of components can be separated into four fundamental subsystems. Each of these subsystems is imperative for the operation of the apparatus. A basic schematic of the entire apparatus is shown in Figure 3.1. For simplicity, the schematic in Figure 3.1 does not show each component contained within the apparatus. Instead, the minutiae of the four subsystems—the combustion chamber and LSB, the gas supply system, optics and imaging, and the data acquisition system—are detailed in subsequent sections.

3.1 The Combustion Chamber and Low Swirl Burner

At the heart of the experimental apparatus is the T-shaped, stainless steel combustion chamber, shown in Figure 3.2; associated dimensioning is shown in Figure 3.3. The 2.54 cm low swirl burner—shown in Figure 3.2, designed and created by Robert Cheng of the Lawrence Berkeley National Laboratory[1]—is integrated into the experimental configuration at the bottom of the vertical section of the chamber, which includes quartz windows to allow optical access to the flame. In this region, the pressure oscillations within the chamber are monitored through one of the chamber's side access ports via a side-mounted PCB-106B piezoelectric pressure transducer. Signals from the transducer are sent to the data acquisition system.

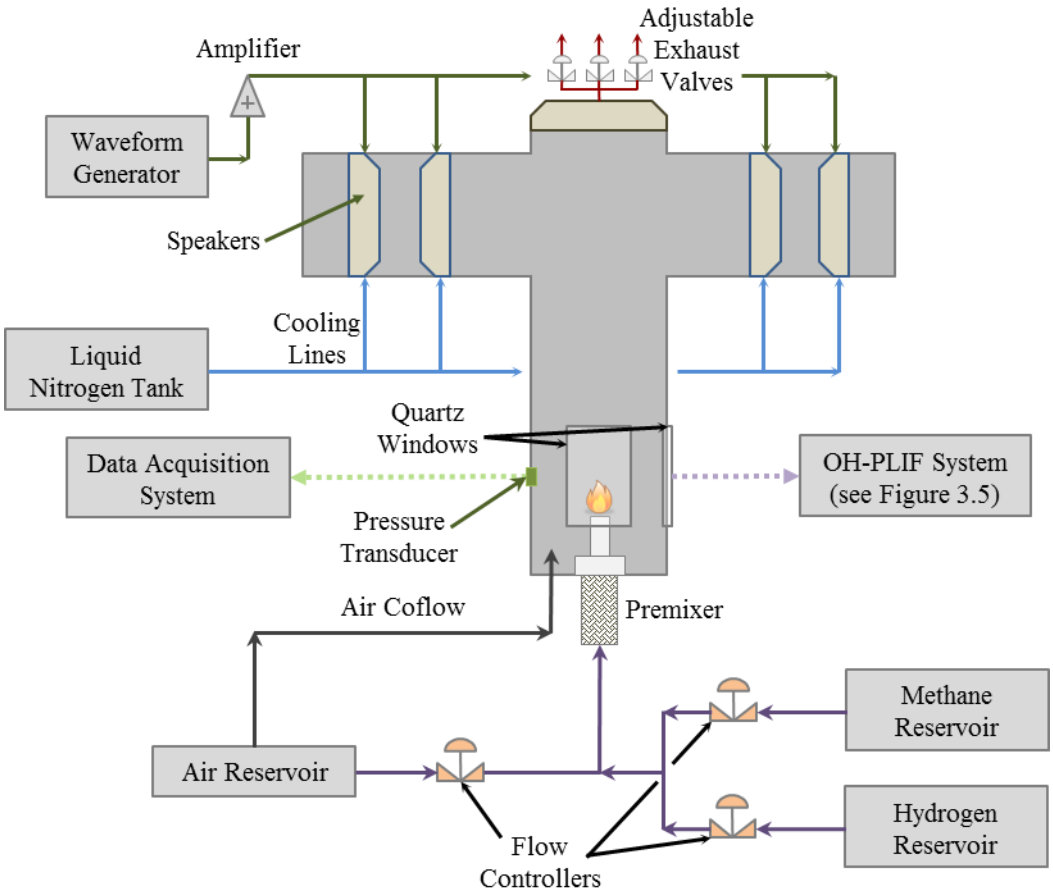

Figure 3.1: Schematic of experimental apparatus, subsystems, and key components

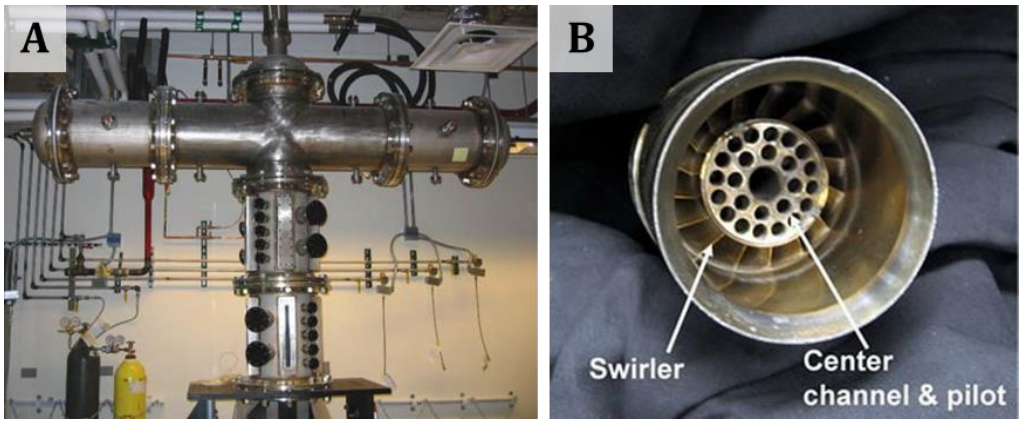

Figure 3.2: The stainless steel combustor and sample low swirl burner

Source: (A) [17]; (B) [143]
(A) Stainless Steel Combustion Chamber
(B) Top view of LSB

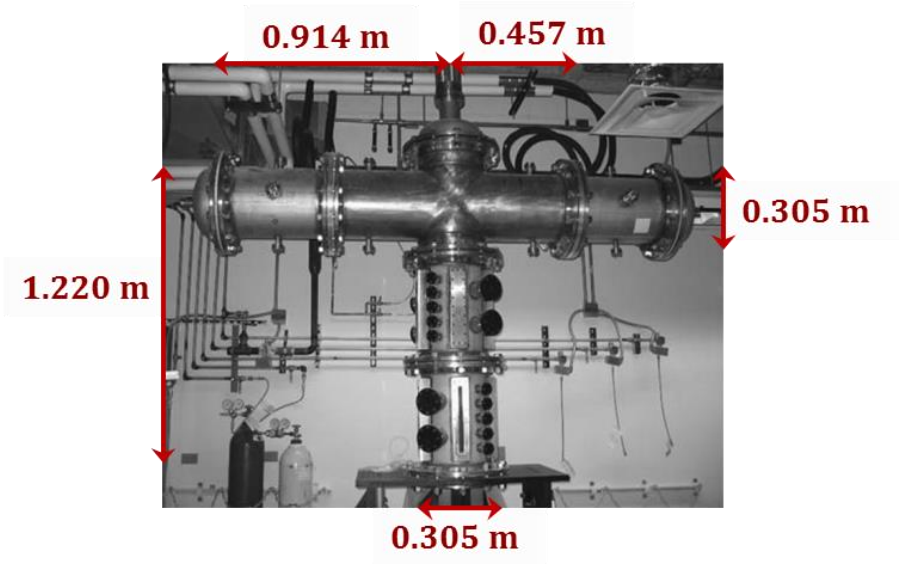

Figure 3.3: Combustion chamber with relevant dimensions shown

The combustion chamber is symmetric about each of the primary vertical planes bisecting the chamber.

At the apex, directly above the LSB, is the exhaust for the chamber. Coupled with this exhaust are three adjustable valves, which allow for the pressurization of the chamber. Located here, at the top of the chamber, are two horizontal branches. Housed within each branch are two speakers, which are controlled using a power supply, waveform generator, and an amplifier. Any acoustic forcing within the system is applied by these four speakers located downstream of the flame. To ensure the speakers do not overheat—as this typically results in failure—cooling lines run nitrogen to the speakers. The temperatures of the speakers are monitored using thermocouples, which are routed to a laptop computer specifically used for displaying the temperature of the two innermost speakers. Cooling lines containing water are responsible for cooling the chamber walls.

Ideally, observed flame responses are due solely to acoustic forcing or flame-flow interactions. Relative to the size of the LSB and the flame, the inner diameter of the chamber is large enough to safely assume that the flame does not interact with the walls of the chamber. As an additional precaution, however, a coaxial and turbulent coflow of air is utilized to affirm that the flame is isolated, and can only be affected only by acoustic forcing or flame-flow interactions.

3.2 Gas Supply System

During the data collection process, consistency is achieved by maintaining a constant unburnt gas mass flow rate. To accomplish this, a series of reservoirs, tubing, flow meters, and flow controllers are utilized. With the goal of maintaining a constant mass flow rate to the burner, the air coflow line and the speakers' nitrogen cooling lines are completely unattached from the network that delivers the unburnt gases to the LSB. With the coflow and the cooling lines, the flow is adjusted manually prior to the collection of data, and is usually untouched during the collection process.

Conversely, the flow rates of the methane, hydrogen, and air to the LSB are closely monitored using flow meters and the data acquisition/flow control system. The flow rates of the methane and the hydrogen are regulated using Hastings HFC-D-303 flow controllers, and the air is adjusted using a Hastings HFC-D-307 flow meter. The flow controller used for the methane is operated from a custom application operated within the data acquisition and control system. Once the flow of each gas has been regulated, the three gases are directed into the same conduit. While some mixing does occur within this pipeline, the gases proceed toward the combustion chamber. Before they are burnt, however, the methane, hydrogen, and air pass through a premixer to homogenize the mixture of the gases. Consisting of a 5 cm-thick layer of small ball bearings followed by a layer of honeycomb, the premixer acts not only to homogenize the gas mixture, but also to protect against the flame flashback to the fuel reservoirs, as the flame cannot propagate through the minute gapes between the ball bearings. Following the premixing, the gases are driven past a series of vanes in the swirler to initiate rotation as the gases exit the LSB and, subsequently, burn. Schematics of the premixer and the swirler for the 2.54 cm LSB are shown in Figure 3.4.

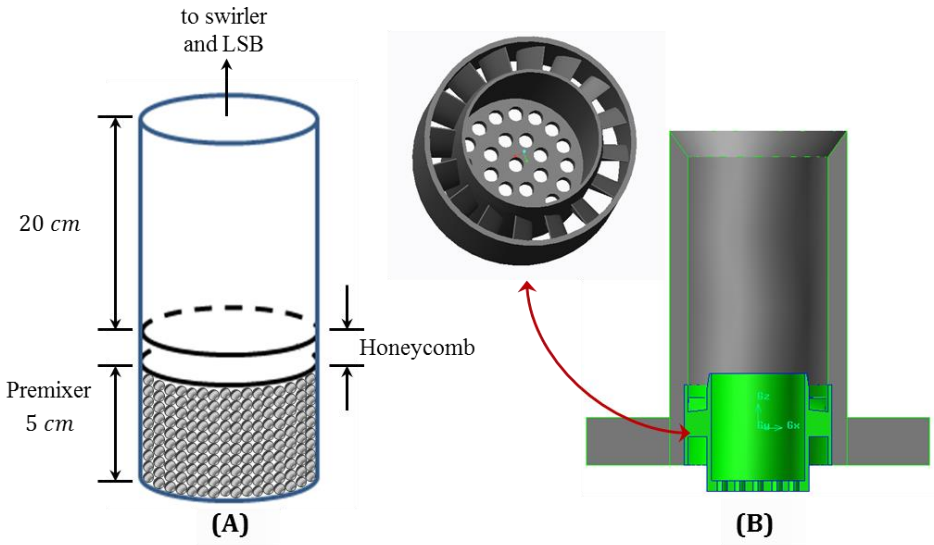

Figure 3.4: Premixer and Swirler

Adapted from [17]
(A) Premixer and premixing chamber
(B) Swirler and its associated position within the LSB

3.3 Optics and Imaging System

In capturing instantaneous images of the LSB flame, OH-PLIF is implemented using the series of components shown in Figure 3.5. The beam is first created by a Continuum Powerlite 9010 Nd:YAG pump laser, which can produce beams with wavelengths between 532 nm and 1064 nm. For the current study, the beam exiting the pump laser appears green, and is characterized by a wavelength of 532 nm. From this point, however, the beam passes through a Continuum ND6000 tunable dye laser, which alters the wavelength of the beam from 532 nm to 564 nm using a solution comprised of

methanol and Rhodamine 590. Following this shift in wavelength, the beam passes through a frequency doubler, which, as its name implies, doubles the frequency of the beam and simultaneously reduces the wavelength of the beam such that the end pulse has a wavelength of 282 nm. Then, the beam is directed through a series of optics to transform the nearly circular beam into a planar laser sheet. As the laser sheet enters the chamber to excite the A,X (1,0) band of OH radicals, an ICCD camera captures the OH-fluorescence emitted by the cross section of the LSB flame. The Nd:YAG laser sends a signal to the data acquisition and control system, which conducts the constant, precise timing delay between the laser pulses and the camera operation. For each set of operating conditions, the ICCD camera captures 900 instantaneous images.

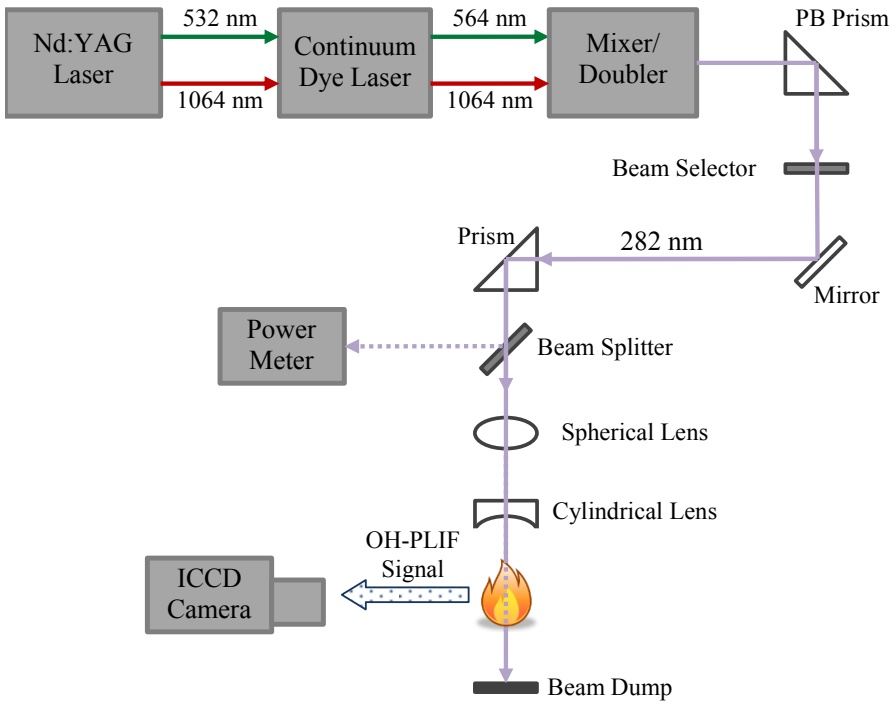

Figure 3.5: Schematic of the Optics and Imaging System

Source: [144]

3.4 Data Acquisition System and Post-Processing

Using a series of installed applications, a desktop computer acts as the hub of the data acquisition and control system. Specifically, the flow rate of the methane is regulated using series of text commands within a custom application. When triggered by the gating signal from the Nd:YAG laser, the ICCD camera captures and sends the digital image data and gating signal to the computer, which utilizes a camera-specific application—which also acts as a parallel card interface controller for the camera—to create a *.spe PlugIn File containing the image data. Additionally, the pressure transducer used in monitoring the chamber pressure sends a signal to a DAQ board, which in turn sends the signal for collection using LabVIEW, which simultaneously records the points within the pressure signal at which the instantaneous OH-PLIF images are captured. Following the data collection process, post-processing begins by using the camera-specific application to separate the stored *.spe files into the TIFF images of the instantaneous intensity of [OH] within the flame. Examples of nstantaneous OH-PLIF images for the LSB flame can be found in Figure 2.3

In conjunction with the chamber pressure signal recorded using LabVIEW, the gating signal is processed using MATLAB to create MATLAB data files containing the image and its associated phase bin information, the corresponding mean pressure, and the fluctuation of pressure (from the mean chamber pressure). Within this post-processing process in MATLAB, the Fast Fourier Transform (FFT) is calculated and subsequently used to map the power spectrum density of the pressure data. From this point, an alternate MATLAB program can be executed to create colorized instantaneous average OH-intensity images and Rayleigh index maps, which can provide insight into characteristics of the flame. In performing additional image processing techniques, flame structures—flame front curvature and flame surface density—can be analyzed by producing the associated probability density functions (PDFs).

CHAPTER 4

RESULTS AND DISCUSSION

Within the discussion that follows, results for the 2.54 cm burner will be presented, and the effect of hydrogen addition and burner diameter on flame stability and structure will be explored. Beginning with flame stability limits, discussions will focus on the limiting pressures associated with flashback for a fixed set of operating conditions within the 2.54 cm LSB. From this point, 2.54 cm LSB flame front curvature data will be presented—via probability distribution functions—and validated using results from previous work. Results following the expected trends are compared to Emadi's results in a 3.81 cm LSB system[17] to establish a relationship between burner diameter and flame front curvature. Then, current results on the flame surface density are presented, validated, and subsequently compared to the FSD results from the 3.81 burner to conclude investigation on the effect of burner diameter on flame structures.

4.1 Flame Stability Limits

In the results that follow, many of the operating points that are examined for the mixture fuel are not operating points that the pure methane fuel is capable of operating. Then, instead of omitting data, the full range of operating points are shown, even if data could not be collected for a fuel mixture or operating condition. However, only the ranges for which data exists for both conditions are considered in examining the effect a parameter may have on the stability limits of a 2.54 cm LSB flame. In some cases, the reason for lack of data at an operating point is simply because the set point simply is not within region of stability. However, as data was being acquired, the flow controller responsible for allowing hydrogen into the premixing region unexpectedly failed. Due to time constraints and the lengthy period of time required for repairing and/or ordering a

new flow controller, the out-of-order flow controller was replaced with a flow controller that was of a similar model. However, the replacement flow controller had a smaller range of operation, and could not supply the required amount of hydrogen for fuel compositions with $\alpha_{H_2} = 0.2$ and bulk velocities larger than 17.5 m/s. Even with limited results, however, general trends and comparisons of results regarding flame stability testing are presented in the following sections on flashback and blowout. In results shown, the discrete operating conditions examined leads to the highly-linear nature observed within graphical representations of the results. However, with an increased number of operating conditions examined, it is expected that graphically, the full sets of results would be characterized by continuous curves.

4.1.1 Flashback

As previously discussed, flashback can be influenced by a variety of parameters, including fuel type, flow velocity, system pressure, and burner geometry. In the current study, the effect of pressure and fuel composition on flashback is examined for pure methane fuel ($\alpha_{H_2} = 0$) and for CH_4/H_2 mixture fuels ($\alpha_{H_2} = 0.2$) operating within a range of equivalence ratios. As the pressure of the combustion system is slowly increased, the chamber pressure counteracts some of the buoyancy-related forces within the flame, and the flame slowly lowers toward the burner. As this occurs, the flame is observed to bounce, and will eventually form a red/orange cone-like structure at the center of the bowl-shaped flame where axial flow propagates downstream. As the pressure is increased, the outer swirled portion of the flame retains its intense blue color. With the current configuration, the moment of flashback occurs when the flame attaches to the swirler, which occurs as the bowl-shaped flame inverts to resemble a V-shaped flame. While the flame is attached to the swirler, the distinctive swirled motion of the

gases can be traced within the flame front. A sample progression toward flashback is shown in Figure 4.1. Results of flashback stability testing are particularly useful in designing stability test procedures, such as those conducted in the current study of blowout stability limits. Although the combustion chamber is designed for high pressures, attention to safe data collection practices were considered, and tests were discontinued if the pressure in the chamber exceeded 30 psig (approximately 3 bar, abs). Additionally, as the pressure within the chamber is increased, the temperature of the speaker system increases more rapidly, and there is a higher potential for melting to occur. Here, then, for segments of data that may seem to be missing, a marker has been added to the graph at a corresponding pressure of 30 psig (approximately three bar absolute) to show that flashback testing was performed for a given velocity, but that flashback did not occur between atmospheric pressure and a chamber pressure of 30 psig.

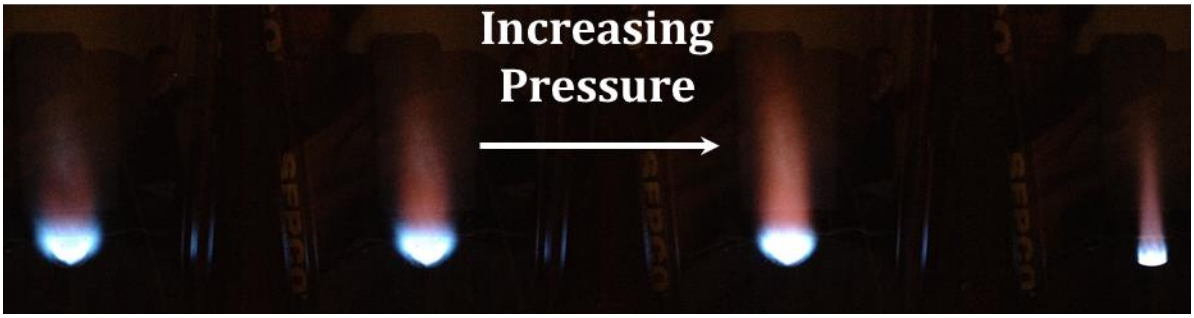

Figure 4.1: Flame structure of 2.54 cm LSB as chamber pressure increases

If examining a specific fuel composition, an increase in the chamber pressure results in an increase in the temperature of the chamber due to the increased number of molecular collisions between reactants and/or intermediate combustion products. Hence, the increased number of collisions is expected to cause an increase in the rate of reaction

and the corresponding reaction temperature. Then with this increase in temperature resulting from the higher mean kinetic energy of the reacting molecules, the density of the mixture is expected to decrease. From the definition of the turbulent flame speed shown in Equation 2.9, then, an increase in chamber pressure will result in an increase in the turbulent flame speed. Because flashback occurs when the flame speed is greater than the local flow velocity, it is expected that for any given set of operating points, a higher velocity will require a higher chamber pressure to induce flashback. For all subsequent flashback limit results that are discussed, this is, in fact, the general trend observed. Occasionally, a decrease in flashback pressure is observed for a higher velocity, but this is likely due to the effect of fluctuations of the pressure (and flow rate) of the compressed air or the effect of chamber pressure on the gas supply lines.

For flashback results presented for the 2.54 cm burner, data was collected by igniting the flame and adjusting the gas flow rates for consistency. The main parameters that were altered include the fuel's volumetric fraction of hydrogen, the equivalence ratio of the reactant mixture, and the bulk velocity of the flow. With all operating conditions set, the exhaust control valves were slowly closed to raise the pressure within the chamber. A pressure gauge was monitored as it was rising, and upon flame flashback, the pressure within the chamber was recorded. Throughout this process, the reactant flow rates were monitored and continually adjusted to maintain consistency within the flow. Although subsequent results provide an insight into the operating conditions examined, a complete list of operating conditions is shown in Appendix A.

As previous studies have shown, an increase in hydrogen in the fuel mixture has resulted in increased flammability limits and increased turbulent flame speeds.[13,15,17,116,120-129] For all equivalence ratios investigated, however, the hydrogenated flame flashed back at lower chamber pressures than the pure methane flame. This is true in observing both absolute flashback pressures as well as those normalized by the turbulent flame speeds for the coincident operating conditions, as shown in Figure 4.2.

With the limit of lower absolute chamber pressures observed at flashback, as evidenced by the results shown, hydrogenated flames cannot be examined for the same range of chamber pressures as those without hydrogen as a reactant.

Until flashback occurs, the flame maintains its bowl shape by resisting the force on the flame from the surrounding pressure, which coaxes the flame to attach to the swirler. As previously discussed, the addition of hydrogen reduces the Lewis number of the flow, causing a reduction in resistance to flame strain.[15,116,126,130] Then, with this decreased resistance to stretching, the mixed flame cannot counteract the effect of pressure as well as the pure methane flame. This provides a simple explanation for why hydrogenated flames are unable to maintain their original shape for the same range of pressures as the non-hydrogenated flames. As a result, the flashback is observed to occur at a lower absolute chamber pressure.

As discussed in the literature review, flashback occurs when the local flame speed exceeds the flow velocity, which allows the flame to propagate upstream toward the gas reservoir. As for the mechanism of flashback occurring here, the flashback is likely occurring in the boundary layer of the flow, since this is typically where the point of lowest velocity occurs. In many swirled flows, the CIVB mechanism will act on the PVC to induce flashback, but because the current system utilizes a low swirl flow, no PVC is present, so the CIVB mechanism is not responsible. Additionally, the flame does not typically bounce or exhibit a decrease in the intensity of radiosity perceived with the naked eye. Therefore, it is expected that the flashback observed in the current study is not a result of alternate instabilities within the system.

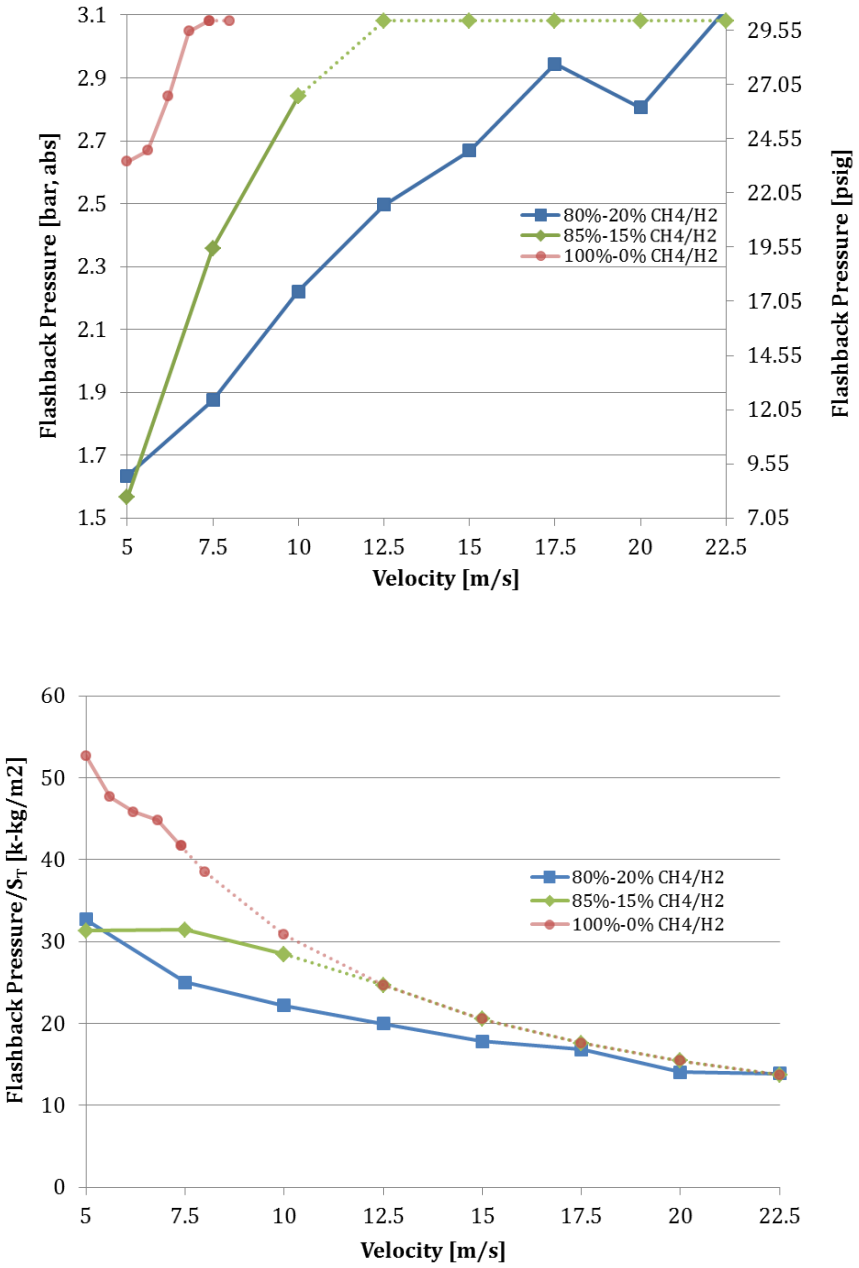

Figure 4.2: Upper flashback pressure limits for $\phi = 0.8$

Dashed lines indicate operating conditions that were examined, but did not flashback before 30 psig.

Top: Absolute Flashback Pressures
Bottom: Flashback pressures normalized by turbulent flame speed

Assuming that flashback occurs in the boundary layer, then, the flashback limits can be shown to be dependent on the composition of the reactant mixture. Recall from Equation 2.9 that the turbulent flame speed is dependent on the mass flow rate of the reactants, the surface area of the flame, and the density of the unburned reactant mixture.

$$S_t = \frac{\dot{m}}{\bar{A}\rho_u} \tag{2.9}$$

As part of the control system, the flow controllers are regulated with the goal of maintaining a constant mass flow rate for all operating conditions. Assuming a relatively consistent flame surface area for the current study, the turbulent flame speed can be thought of as solely dependent on ρ_u. However, the density is mainly dependent on the composition of the unburned reactant flow. Then, for the different levels of fuel hydrogenation, the turbulent flame speed is directly altered by the presence of hydrogen. An alternative explanation demonstrates that the laminar flame speed depends uniquely on the thermal and chemical properties of the mixture and the turbulent flame speed is dependent on these as well as the intensity of turbulence.[18] Consequently, changes in turbulent flame speed due to modified fuel compositions are due to the direct effect of fuel composition on laminar flame speed. As expected, the addition of hydrogen increases the laminar flame speed, which in turn increases the turbulent flame speed.

Although it is known that flashback limits are dependent on turbulent flame speed—and hence, the fuel composition—and substantial variations in the turbulent flame speed existing due to fuel composition have been concretely recognized, comprehensive data sets or validated models for the relationship between the two have not been established.[117]

In further examinations of the effect of fuel composition on the flashback pressure limit, the equivalence ratio is varied for a consistent volume fraction of hydrogen

($\alpha_{H_2} = 0.2$). Within these results, shown in Figure 4.3, higher flashback pressures are observed for an increasing equivalence ratio. The region of negative slope within absolute results for $\phi = 0.8$ is likely due to pressure fluctuations that occurred along the gas supply lines due to pressure oscillations within the combustion chamber or fluctuations in the flow rate of compressed air. As will be shown in Chapter 4 during the characterization of properties of a gaseous mixture, the density of a mixture is shown to decrease with an increase in equivalence ratio. Then, with a higher equivalence ratio, the turbulent flame speed increases due to the decrease in ρ_u. Then, for flashback to occur, a higher chamber pressure is required to counteract the increased flame speed and push the flame toward the burner. Normalizing the results by the turbulent flame speed acts to smooth the distribution by maintaining the inversely proportional trend between bulk velocity and normalized flashback pressure. Even though the magnitudes of the normalized flashback limits for the two reactant mixtures were similar, the mixture with the higher equivalence ratio is still shown to flashback at higher chamber pressures.

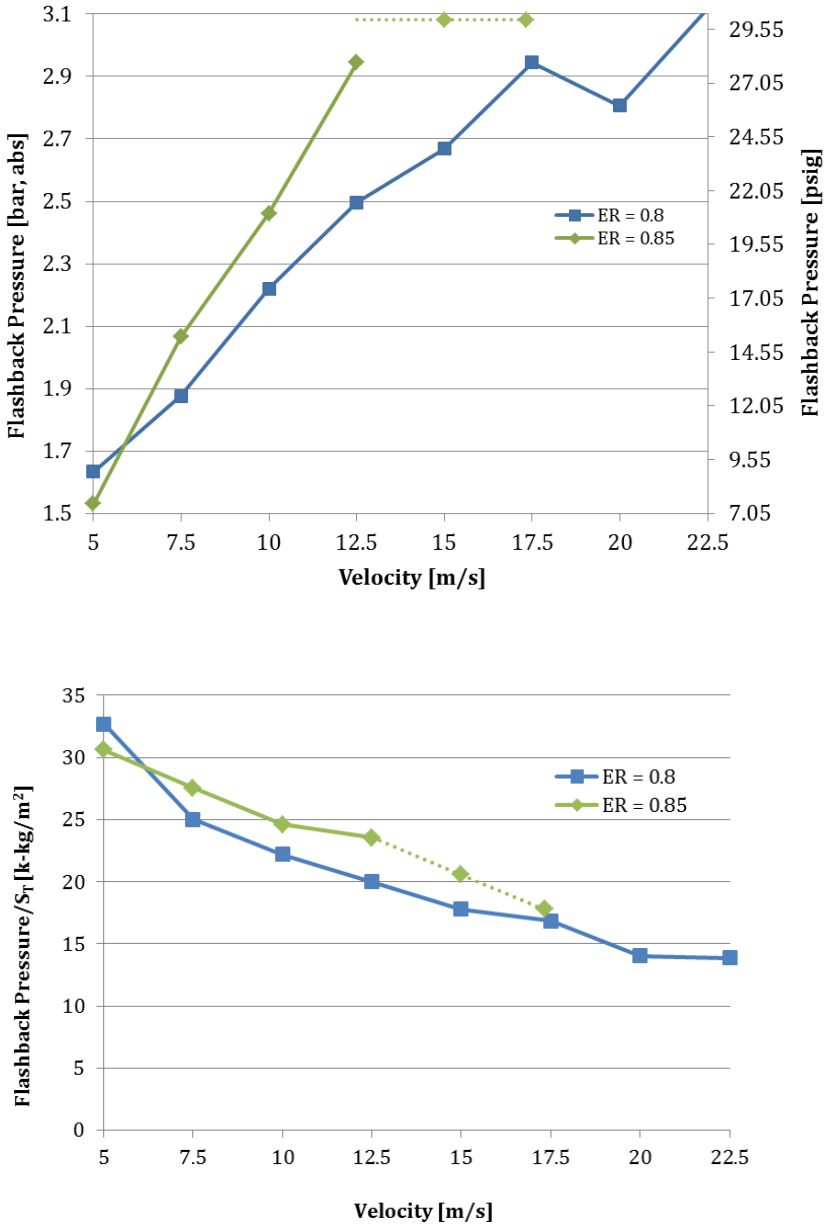

Figure 4.3: Upper flashback pressure limits for a constant fuel mixture consisting of 80% CH_4 – 20% H_2

For dashed lines shown, flashback did not occur before 30 psig (an absolute pressure of approximately 3.1 bar).

Top: Absolute Flashback Pressures
Bottom: Flashback pressures normalized by turbulent flame speed

4.1.2 Blowout

A process similar to collecting flashback limit information was employed in investigations examining the lean stability regime of the 2.54 cm LSB. Upon flame ignition, the flow conditions were adjusted to fulfill the predetermined operating conditions. In examining LBO characteristics of the system, the main parameters that were altered include the fuel's volumetric fraction of hydrogen, the bulk velocity of the flow, and the pressure within the combustion chamber. For cases at elevated pressures, the flow conditions were set, and the exhaust valves were closed until the pressure within the chamber held constant at the desired pressure. Occasionally, pressure fluctuations were observed, but did not typically influence the nature of the flame. Then, with the chamber pressure and bulk velocity held constant, the flow parameters were adjusted such that the equivalence ratio of the reactant mixture was decremented. At each equivalence ratio, the nature of the flame was observed to determine the lean stability characteristics at each set point. As ϕ was decremented, two equivalence ratios were recorded. The higher of the two equivalence ratios is the point at which the onset of instability is observed. Physically, at the onset of instability, the flame begins to bounce and the once bright blue flame becomes noticeably dimmer. For this set of operating conditions, the second equivalence ratio recorded is the leaner of the two key equivalence ratios. At this equivalence ratio, the flame extinguishes via the LBO mechanism. The dashed, gray arrow in Figure 4.4 is a simple illustration of the methodology used in examining the lean regime for a single set of conditions. For the subsequent results presented, dashed curves indicate the onset of instability, and like-colored solid curves illustrate the corresponding blowout. A full list of operating conditions is shown in Appendix A, but are also depicted in the figures shown by the geometrically-marked data points.

To compare the LBO limits of the 2.54 cm burner to those of the 3.81 cm burner, the effect of fuel hydrogenation and elevating the chamber pressure are first examined to

ensure that results follow the same general trends exhibited by previous investigations of LBO limits. With the exception of a select few operating conditions, an increase in flow velocity results in an increase in the LBO limit, demonstrating that lean regimes further away from the stoichiometric burning condition are more stable at lower velocities, which is in agreement with previous studies that have examined LBO limits.[17,117,118,120,121] Exceptions are likely attributable to natural fluctuations in the flow rate of the reactants; specifically, in the supply of the air or methane. Among other influences, unexpected equipment failure and the necessity for monitoring the speaker temperature limited the range of operating conditions that could be examined for the different fuel mixtures. For the same reason, equivalence ratios were adjusted using intervals of $\phi = 0.05$. In certain cases, however, the nitrogen cooling system effectively counteracted the heating caused by the presence of the flame, and modifications were made such that the interval between equivalence ratio was decreased to $\phi = 0.025$. Dashed lines in the subsequent presentation of stability limits represent the appearance of instability within the combustion system and physically, blowout of the flame is not observed until the equivalence ratios depicted by the solid line(s) shown.

In assessing the validity of the current examination of LBO limits in the 2.54 cm LSB, the effect of fuel hydrogenation is also examined. Resulting stability limits for two fuel mixtures ($\alpha_{H_2} = 0,\ 0.2$) are shown in Figure 4.4 and Figure 4.5. As predicted by previous examinations of the lean flammability limit,[17,115-121] the addition of hydrogen to the fuel mixture is shown to result in increased stability at lean regimes further away from the stoichiometric burning condition. With the addition of hydrogen, this trend is demonstrated by the lower LBO limits observed, as well as the lower onset of instability within the combustion chamber. Results at both atmospheric conditions (1 bar, absolute) and elevated chamber pressure conditions are consistent with the trends established by previous work.[17,118-120] For a given fuel mixture, the onset of instability occurs for a resolution ($d\phi$) that is $0.05 - 0.1$ higher than the limit at which LBO is observed.

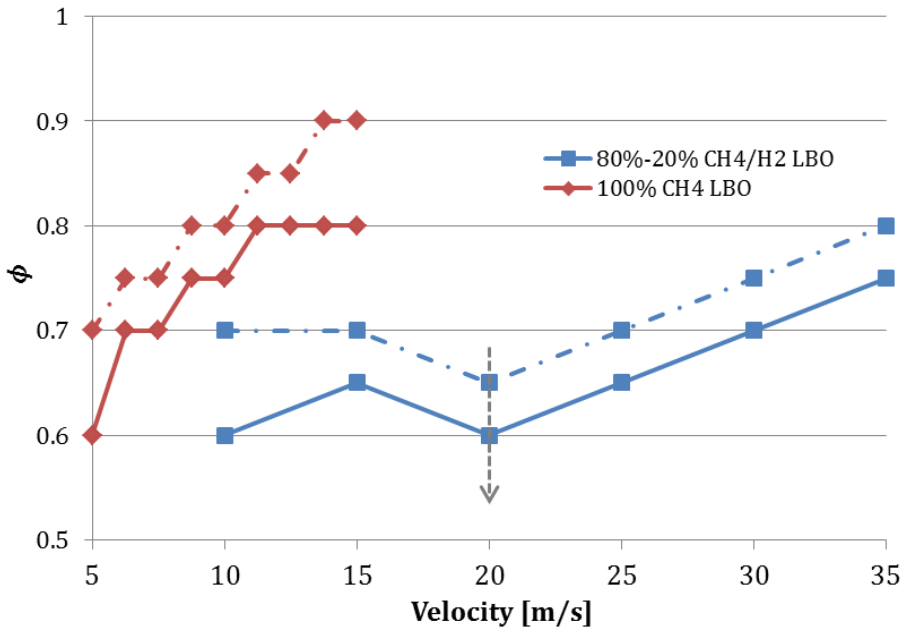

Figure 4.4: Effect of hydrogen addition on stability limits at atmospheric pressure (1 bar, absolute)

Dashed lines indicate the onset of instability. Flames exhibited an unstable nature between the dashed and solid lines, which indicate the point at which LBO was observed.

The gray arrow depicts the process used in examining lean stability limits. With a constant velocity, the equivalence ratio was decreased until the onset of instability and LBO were observed.

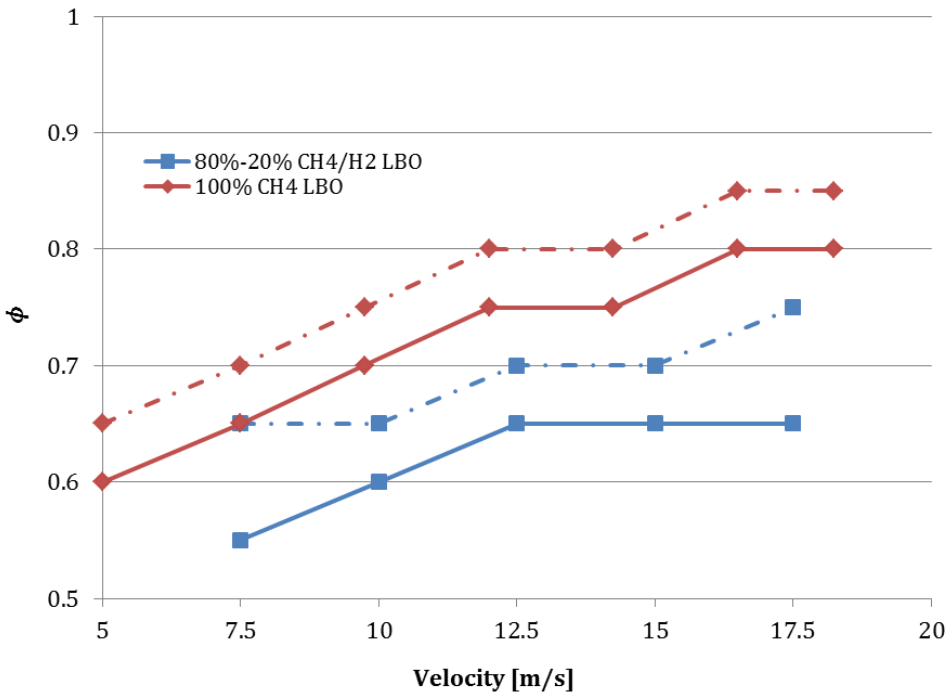

Figure 4.5: Effect of hydrogen addition on stability limits for a chamber pressure of 1.5 bar (absolute)

For further investigation of the legitimacy of the stability data in the 2.54 cm burner, the effect of pressure on the LBO is examined. If results for the pure methane fuel—shown in Figure 4.6—are examined, an increase in chamber pressure results in an apparent decrease in the lean stability limit of the burner, as predicted by previous examinations of the effect of chamber pressure on lean stability limits.[17] If examining results for the hydrogenated fuel, as shown in Figure 4.7, however, this trend is not as apparent. In some regions, the trend is observed, but in others, the onset of instability and the LBO limits overlap for an increasing chamber pressure. This may, in part, be attributable to resolution of the intervals between the examined equivalence ratios. Until this set of results, LBO stability trends have been in agreement with those established by previous work. Then, it is speculated that if the LBO limits were reexamined for fuel

having $\alpha_{H_2} = 0.2$ with a smaller resolution, an increase in pressure would more clearly result in a decrease in LBO limits. In lieu of this, the differential between the onset of instability and the observance of LBO in the current case is such that $d\phi \propto 0.05 - 0.1$. In examining the effect of bulk velocity, fuel hydrogenation, and elevating the pressure of the combustion chamber, nearly all of the current results comply with the general trends established by the previous results. With expectations that reexamining the effect of pressure on the $\alpha_{H_2} = 0.2$ hydrogenated fuel will result in the established trend, the current lean stability results will be compared to previous results.

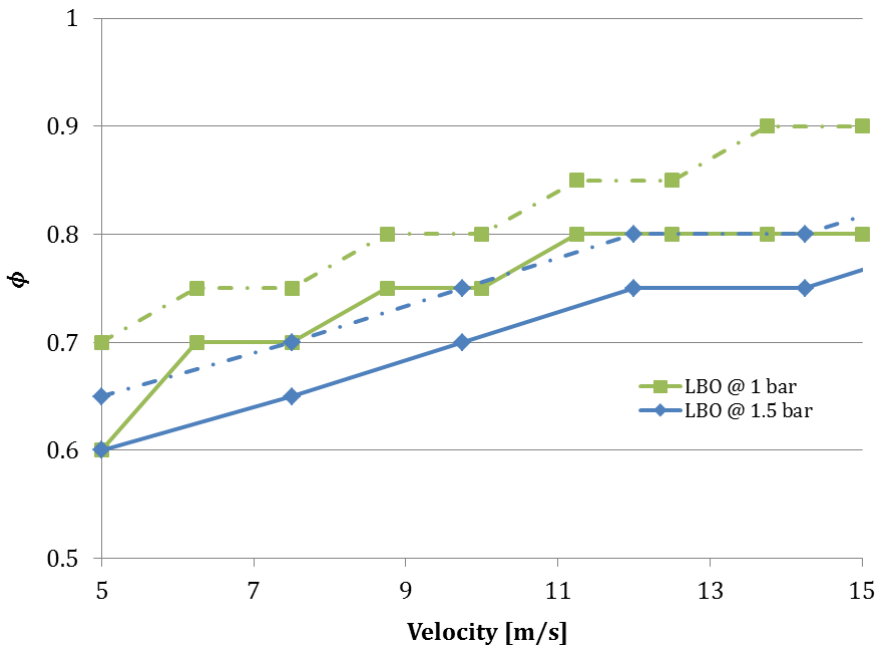

Figure 4.6: Effect of chamber pressure on stability limits for 100% CH_4 fuel

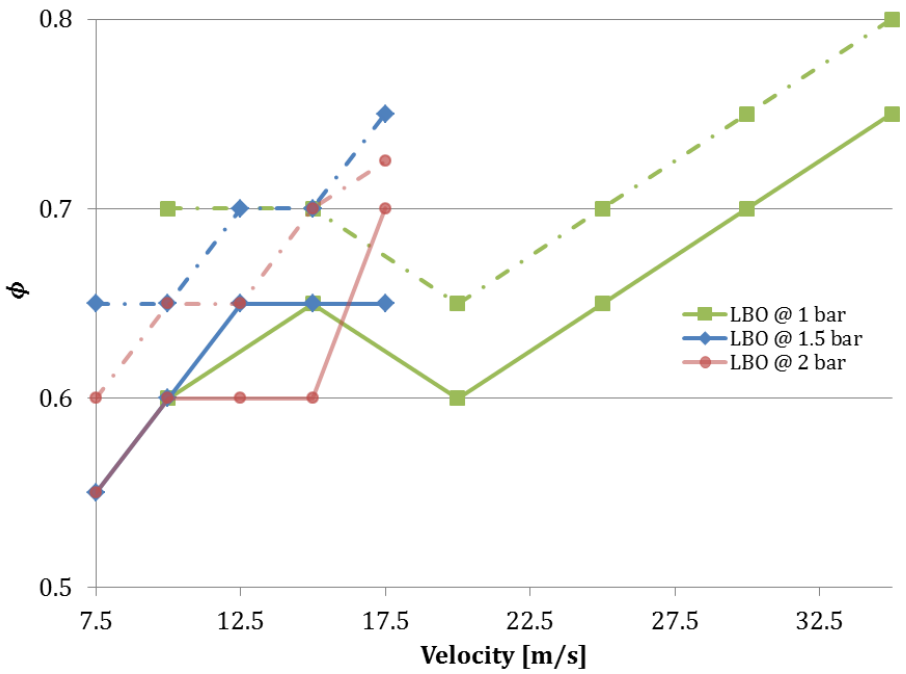

Figure 4.7: Effect of chamber pressure on stability limits for mixed fuel (80% CH_4 and 20% H_2)

While many have examined the effect of hydrogen addition on LBO limits in low swirl systems, most did not use mixtures of solely methane and hydrogen. For fuel mixtures that did resemble mixtures of methane and hydrogen, the LBO limits were typically presented for chamber pressures greater than 5 bar (absolute) or for a single operating point. Emadi,[17] however, presented LBO limits for a 3.81 cm burner for a much wider range of velocities and chamber pressures. Because the equivalence ratio is varied within LBO stability examinations, the Reynolds number of the flow is also constantly changing. Then, in comparing with Emadi's results, neither the Reynolds number nor the velocity of the flow is used. Instead, the lean stability limits in Figure 4.8, Figure 4.9, and Figure 4.10 are presented against the velocities per unit area of the burner outlet. For the 2.54 cm-diameter LSB, the outlet area is 5.067 cm^2 while Emadi's 3.81 cm-diameter LSB

has an outlet area of 11.401 cm^2. Other than the diameter of the burner, the other key difference is that in the current work, the resolution of equivalence ratio decrements was 0.05 while Emadi utilized a resolution of 0.025.

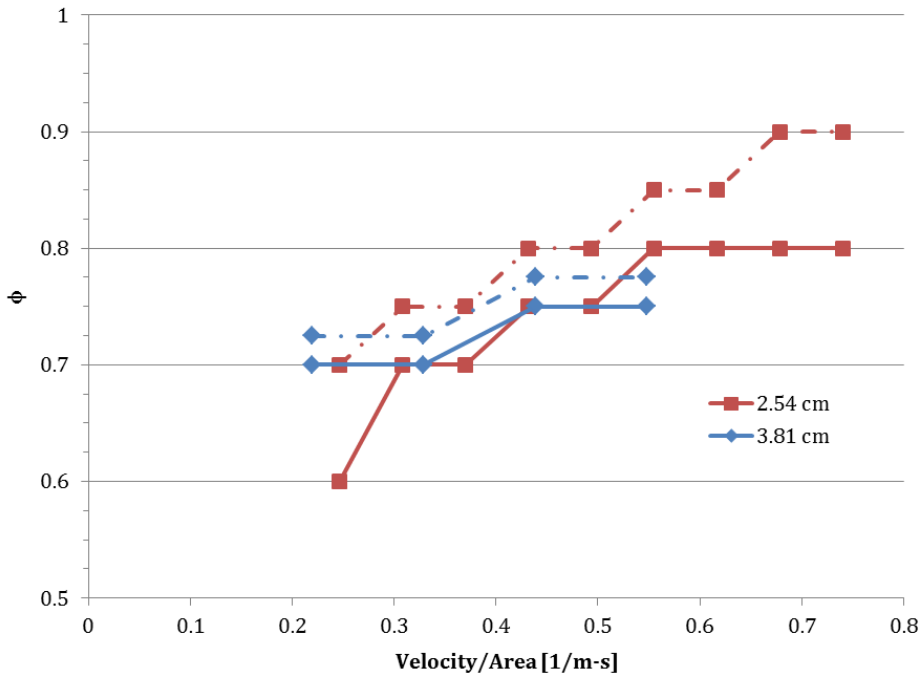

Figure 4.8: 100% CH_4 fuel LBO limits for the 2.54 and 3.81 cm LSB at atmospheric conditions

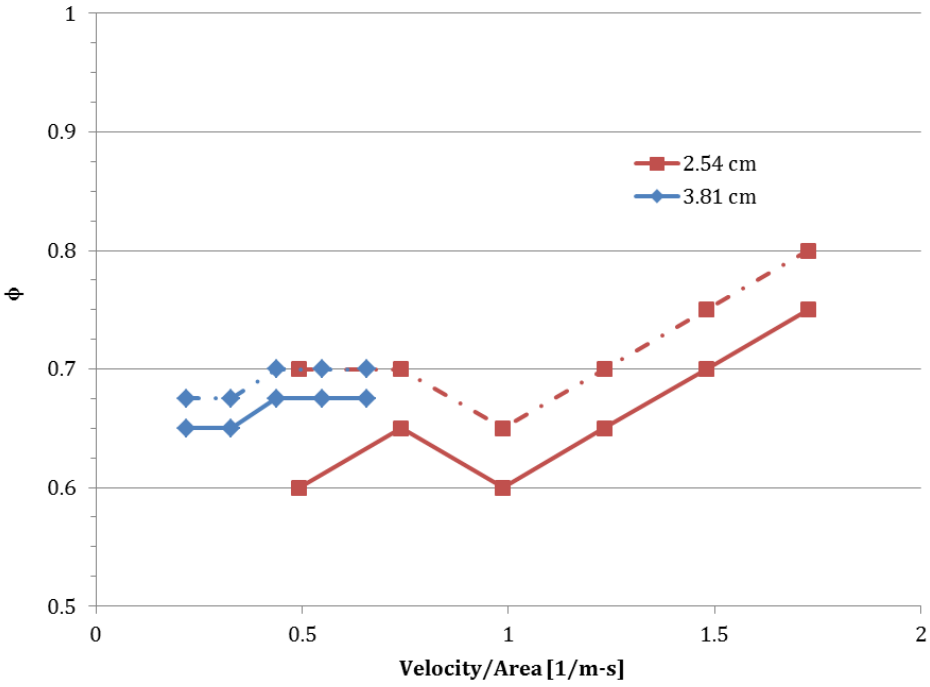

Figure 4.9: LBO limits for the 2.54 and 3.81 cm LSB with hydrogenated fuel (80% CH_4 and 20% H_2) flames at atmospheric pressure conditions

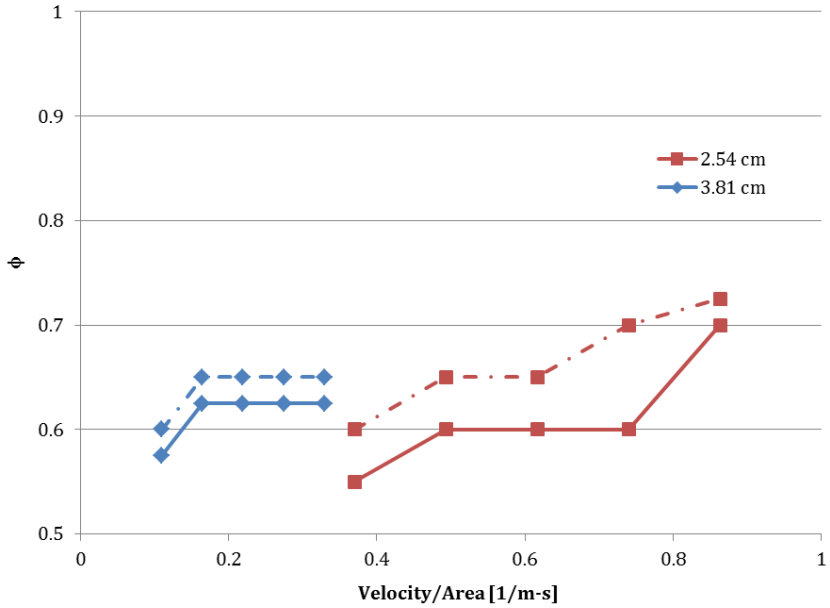

Figure 4.10: LBO limits of the 2.54 and 3.81 cm LSB for hydrogenated fuel (80% CH_4 and 20% H_2) flames at an elevated chamber pressure of 2 bar

In results for both the pure methane fuel and the mixed methane-hydrogen fuel ($\alpha_{H_2} = 0.2$), the magnitude of the equivalence ratio at both the onset of instability and the blowout limit are very comparable between the two burner sizes. The differential between the onset of instability and the blowout limit is also very similar; for the 2.54 cm burner, the differential is such that $d\phi \propto 0.05 - 0.1$. The sole exception lies at a normalized velocity of approximately 0.86 for the mixed fuel at a chamber pressure of 2 bar. Here, the differential was smaller, with $d\phi = 0.025$. However, for this velocity, the cooling system for the liquid nitrogen effective at cooling the speaker temperature, so the equivalence ratio decrement was decreased between each set of operating conditions examined. For the 3.81 cm LSB lean stability limits presented here, the differential between the onset of instability and LBO was consistently such that $d\phi = 0.025$. Beyond recognition that the magnitudes of the equivalence ratio and the order of magnitude between the onset of instability and LBO are similar, the differential between onset of instability and LBO appears to be directly correlated to the resolution employed in the data collection process. To confirm this observation, the examination should be performed for the 2.54 cm LSB using a smaller decrement between the observed equivalence ratios. Results of the current work will be useful in narrowing down operating conditions, as the flow rates for the reactants can be preset to minimize the time required for data collection. Then, with the current results, the duration of flame ignition is not likely to be as much of a limiting factor in future examinations of the lean stability region of 2.54 cm burners.

4.2 Flame Structures

In the examination of chamber pressure and acoustic forcing on mixed fuel flame structures, OH PLIF was used to record instantaneous images of the flame for

atmospheric pressure conditions and elevated chamber pressure conditions. In Emadi's work with a 3.81 cm LSB,[17] the bulk velocity was consistent at 10 m/s with an equivalence ratio of $\phi = 0.75$ for pure methane fuel cases and $\phi = 0.65$ for 80% CH_4 – 20% H_2 fuel mixtures. To be able to compare 2.54 cm and 3.81 cm results, expressions for mixture properties are derived in terms of predetermined properties to express the condition required for Reynolds number similarity and to establish the flow conditions required within the 2.54 cm LSB.

Following this derivation and an associated discussion on characteristic Reynolds numbers and the similarity condition, flame structure results are presented. In the determination of flame front curvature and flame surface density, MATLAB is used to extend the Canny edge detection algorithm to the OH-PLIF images obtained. In setting an limit on OH-intensity, the flame front of each instantaneous image of the flame is binarized, and the resulting flame edge is recorded. Until this point, the process of determining flame front curvature is identical to the process used to determine FSD. The pictorial demonstration in Figure 4.11 shows a flame edge detection process similar to that utilized in the current work. After this point, however, the process required in resolving curvature and FSD diverges. Subsequent steps required for image processing are detailed in the upcoming sections on results obtained for the flame front curvature and flame surface density of a 2.54 cm LSB.

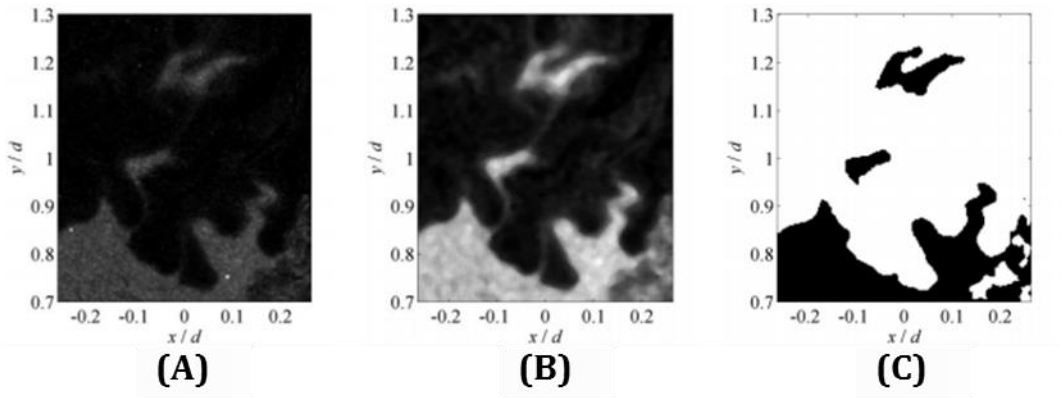

Figure 4.11: Pictorial demonstration of the process used to detect the flame edge along the boundary of the OH layer from OH-PLIF images

---

Source: [140]

Here, the raw image was collected using particle image velocimetry (PIV), but a similar edge detection process is applied for OH-PLIF images as well.

(A) Raw PIV image
(B) Median-filtered image
(C) Threshold image used in detecting the flame edge

The results of the current work are then validated using trends established in previous flame structure examinations. With validity confirmed, flame structures of 2.54 and 3.81 cm LSB flames are compared to establish any potential effect of burner diameter on flame front curvature and flame surface density.

4.2.1 Flow Properties of Binary and Three-Component Gaseous Mixtures

In the following derivation of flow properties, a few assumptions are made in to simplify the derivation process. In all compositions of the reactance mixture, the gases comprising the mixture are assumed to be perfect gases with non-variable dynamic viscosities and densities. Although many characteristic properties are highly dependent on pressure and temperature, the reactant mixture homogenizes in the premixing process that occurs in the gas supply lines and the premixer section (see Figure 3.4) prior to ignition. Then, it is assumed that as the reactants mix, the temperature and pressure of the reactance mixture is homogeneous prior to ignition. With this assumption, the properties for the individual reactant species are evaluated at standard temperature and pressure (STP), and will be specified during discussion of dimensionless number matching conditions. Additionally, when referring to the oxidizer in the subsequent derivations, air will be treated as its own species, instead of considering oxygen and nitrogen separately. With this assumption, the expressions for stoichiometric fuel/air mixture ratios shown in Equation 2.2 and Equation 2.6 will be rewritten in terms of a simplified coefficient, 'b,' such that $b = 4.76a$, where 'a' is the molar coefficient for the reacting air. The process used to determine mixture properties for different reactant mixture compositions will begin here. For further clarification on definition of variables, please refer to the attached nomenclature section. Once the derivations have been presented, results are applied to the flow conditions of the current work for comparison of flow conditions of the 2.54 cm LSB to similar burners having a different diameter.

4.2.1.1 Methane-Air Reactant Mixture

For a mixture consisting solely of methane and air, recall the stoichiometric reaction used in describing this process, as shown in Equation 2.1. Then, for combustion

of methane (CH_4), the coefficient $a = x + y/4$ is evaluated for a single carbon molecule and four hydrogen molecules. Then, for stoichiometric burning of methane, $a = 2$ and $b = 9.56$. If now, the fuel-to-air mixture ratio is rewritten using this new coefficient, the expression becomes as shown in Equation 4.1. For this binary mixture of gases, the fuel species translates directly to the methane species, and the oxidizer is simply air.

$$C_xH_y + a(O_2 + 3.76N_2) \rightarrow xCO_2 + \frac{y}{2}H_2O + 3.76aN_2 \tag{2.1}$$

$$(F/A)_{stoic} = \left(\frac{m_{fuel}}{m_{air}}\right)_{stoich} = \left(\frac{n_{fuel}}{n_{air}}\right)_{stoich} \frac{MW_{fuel}}{MW_{air}}$$

$$(F/A)_{stoic} = \frac{1}{b}\frac{MW_{fuel}}{MW_{air}} \tag{4.1}$$

Then, utilizing the definition of the equivalence ratio, Equation 2.3 can be rearranged to determine an expression for the molar ratio of fuel to air, as in Equation 4.2.

$$(F/A) = \phi(F/A)_{stoic}$$

$$\left(\frac{m_{fuel}}{m_{air}}\right) = \left(\frac{n_{fuel}}{n_{air}}\right)\frac{MW_{fuel}}{MW_{air}} = \phi\ \frac{1}{b}\frac{MW_{fuel}}{MW_{air}}$$

$$\left(\frac{n_{fuel}}{n_{air}}\right) = \frac{\phi}{b} \tag{4.2}$$

However, in recognizing that the mass of a component is simply the product of its density and volume, Equation 4.3 shows an expression for the ratio of fuel volume to the volume of air. From this point on, the subscript '$fuel$' will be shortened to 'f' and 'air' will be shortened to 'a' for clarity purposes.

$$\frac{m_{fuel}}{m_{air}} = \frac{\rho_f V_f}{\rho_a V_a} = \phi \, \frac{1}{b} \frac{MW_f}{MW_a}$$

$$\frac{V_{CH_4}}{V_a} = \frac{\phi}{b} \frac{\rho_a}{\rho_{CH_4}} \frac{MW_{CH_4}}{MW_a} \tag{4.3}$$

Then, with the assumption that each gas species acts ideally, the density of a gas mixture reduces to Equation 4.4, where the subscript 'm' denotes the mixture properties, and summations are performed over subscript 'i.'

$$\rho_m = \sum \rho_i V_i \Big/ \sum V_i \tag{4.4}$$

Then, for a reactant mixture of methane and air:

$$\rho_m = \left(\rho_{CH_4} V_{CH_4} + \rho_a V_a\right) \Big/ \left(V_{CH_4} + V_a\right)$$

$$\rho_m = \frac{\rho_{CH_4} \frac{V_{CH_4}}{V_a} + \rho_a}{\frac{V_{CH_4}}{V_a} + 1} \tag{4.5}$$

Then, the known densities and molecular weights can be used in Equation 4.3 to determine the volumetric ratio of CH_4 to air for any given equivalence ratio. Subsequently, the density of the binary CH_4-air mixture can be evaluated using Equation 4.4.

In assessing the Reynolds number of the flow, the dynamic viscosity of the mixture must also be known. This is accomplished using the form of the expression for mixture viscosity developed by Herning and Zipperer,[145] which, as shown in Equation

4.6, is dependent solely on the mole fractions, dynamic viscosities, and molecular weights of the gas species.

$$\mu_m = \sum x_i \mu_i \sqrt{MW_i} \Big/ \sum x_i \sqrt{MW_i} \tag{4.6}$$

For a mixture of methane and air, this expression can be simplified further. Recall, from Equation 4.2 that the molar ratio of methane to air is given by $\phi/2$ and that a mole fraction is defined as the ratio of the moles of a species to the total number of moles present within the mixture. A simplification of Herning and Zipperer's equation is shown, and is valid for the majority of gas mixture cases, except in hydrogen-rich mixtures. Even in the hydrogenated fuel (which will be discussed shortly), the mixture is not considered 'hydrogen-rich.' As the fuel mixture becomes increasingly rich in hydrogen, Davidson[145] suggests the use of Wilke's equation, which requires a significantly higher level of bookkeeping in the determination of viscosity. For the pure methane fuel, this is not a concern, and the resulting dynamic viscosity of the mixture is shown in Equation 4.7. Recall that for the binary mixture of methane and air, $b = 9.56$.

$$\mu_m = \frac{x_{CH_4}\mu_{CH_4}\sqrt{MW_{CH_4}} + x_a\mu_a\sqrt{MW_a}}{x_{CH_4}\sqrt{MW_{CH_4}} + x_a\sqrt{MW_a}}$$

$$\mu_m = \frac{\left(\frac{n_{CH_4}}{n_{CH_4}+n_a}\right)\mu_{CH_4}\sqrt{MW_{CH_4}} + \left(\frac{n_a}{n_{CH_4}+n_a}\right)\mu_a\sqrt{MW_a}}{\left(\frac{n_{CH_4}}{n_{CH_4}+n_a}\right)\sqrt{MW_{CH_4}} + \left(\frac{n_a}{n_{CH_4}+n_a}\right)\sqrt{MW_a}}$$

$$\mu_m = \frac{\left(\frac{n_{CH_4}}{n_a}\right)\mu_{CH_4}\sqrt{MW_{CH_4}} + \mu_a\sqrt{MW_a}}{\left(\frac{n_{CH_4}}{n_a}\right)\sqrt{MW_{CH_4}} + \sqrt{MW_a}}$$

$$\mu_m = \frac{\phi\mu_{CH_4}\sqrt{MW_{CH_4}}+b\mu_a\sqrt{MW_a}}{\phi\sqrt{MW_{CH_4}}+b\sqrt{MW_a}} \tag{4.7}$$

To summarize, Table 4.1 shows the equations required to find the mixture density and dynamic viscosity for a binary gas mixture.

Table 4.1: Equations needed in determining mixture density and viscosity of a binary gas mixture for known volume fraction of hydrogen and equivalence ratio

Quantity of Interest	**Equation Number**
$\frac{n_{fuel}}{n_{air}}$	(4.2)
$\frac{V_{CH_4}}{V_a}$	(4.3)
ρ_m	(4.5)
μ_m	(4.7)

4.2.1.2 Methane-Hydrogen-Air Reactant Mixture

The process used in formulating an expression for the density and viscosity of a three-gas mixture in terms of known quantities is similar to that of a binary gas mixture, but is much more of an involved process. As such, the full simplification of subsequent expressions is not presented here to maintain clarity. Instead, individual steps utilized in simplification processes are presented in Appendix B. To begin, the definition of volumetric fraction of hydrogen and the stoichiometric chemical reaction for a mixture of methane, hydrogen, and air are presented in Equations 2.4 and 2.5.

$$\alpha_{H_2} = \frac{V_{H_2}}{V_{H_2}+V_{CH_4}} \tag{2.4}$$

$$\begin{aligned}&\left(1-\alpha_{H_2}\right)CH_4 + \alpha_{H_2}H_2 + \left(2-1.5\alpha_{H_2}\right)(O_2+3.76N_2) \rightarrow \\ &\left(1-\alpha_{H_2}\right)CO_2 + \left(2-\alpha_{H_2}\right)H_2O + 3.76\left(2-1.5\alpha_{H_2}\right)N_2\end{aligned} \tag{2.5}$$

If α_{H_2} gives the volume fraction of hydrogen in fuel, then α_{CH_4} can be used to represent the volume fraction of methane within the fuel mixture. These two definitions are used to determine the volumetric ratio of methane to hydrogen, as shown in Equation 4.8.

$$\frac{V_{CH_4}}{V_{H_2}+V_{CH_4}} = 1-\alpha_{H_2}$$

$$\frac{V_{CH_4}}{V_{H_2}} = \frac{1-\alpha_{H_2}}{\alpha_{H_2}} \tag{4.8}$$

Within the assumptions that were made, it was assumed that the characteristic properties of the gas species were constant. Then, combining densities, viscosities, or molecular weights into single term will also act as a constant. Applying this principle and a series of conversions from a mass-basis to a molar-basis, expression for the molar ratio of methane to hydrogen (shown in Equation 4.9) is formulated.

$$\frac{\rho_{CH_4}}{\rho_{H_2}}\frac{MW_{H_2}}{MW_{CH_4}} = const.$$

$$\frac{n_{CH_4}}{n_{H_2}} = \frac{\left(1-\alpha_{H_2}\right)}{\alpha_{H_2}}\frac{\rho_{CH_4}}{\rho_{H_2}}\frac{MW_{H_2}}{MW_{CH_4}} \tag{4.9}$$

If, again, the coefficient 'b' is introduced to simplify expressions, the stoichiometric fuel-to-air ratio can be rewritten, with $b = 4.76(2 - 1.5\alpha_{H_2})$. Using a process resembling that for the binary fuel mixture, the actual ratio of fuel to air can be determined, and is shown in Equation 4.10. From this point, the process continues in finding the molar fuel-to-air ratio and subsequently, an expression for the molar ratio of methane to air. Equation 4.11 will be used for substitution in successive equations to reduce the number of unknown expressions required for evaluating the properties of the three-gas mixture.

$$(F/A) = \phi\,(F/A)_{stoic}$$

$$\frac{m_f}{m_a} = \frac{\phi}{b}\frac{MW_f}{MW_a} \tag{4.10}$$

$$\frac{n_f}{n_a} = \frac{n_{CH_4}+n_{H_2}}{n_a} = \frac{\phi}{b}$$

$$\frac{n_{CH_4}}{n_a} = \frac{\phi}{b} - \frac{n_{H_2}}{n_a} \tag{4.11}$$

Now, returning to Equation 4.9, a chain rule of sorts is applied to the molar methane-to-hydrogen ratio, and Equation 4.11 is used to simplify the expression to find the molar ratio of hydrogen to air in terms of known quantities. This relationship is found in Equation 4.12.

$$\frac{n_{CH_4}}{n_a}\frac{n_a}{n_{H_2}} = \frac{(1-\alpha_{H_2})}{\alpha_{H_2}}\frac{\rho_{CH_4}}{\rho_{H_2}}\frac{MW_{H_2}}{MW_{CH_4}}$$

$$\frac{n_a}{n_{H_2}} = \frac{b}{\phi}\left(1 + \frac{(1-\alpha_{H_2})}{\alpha_{H_2}}\frac{\rho_{CH_4}}{\rho_{H_2}}\frac{MW_{H_2}}{MW_{CH_4}}\right)$$

$$\frac{n_{H_2}}{n_a} = \frac{\phi}{b}\left[1 + \frac{(1-\alpha_{H_2})}{\alpha_{H_2}}\frac{\rho_{CH_4}}{\rho_{H_2}}\frac{MW_{H_2}}{MW_{CH_4}}\right]^{-1} \tag{4.12}$$

With the assumption that the gases in the reactant mixture act perfectly and exist at the same temperature and pressure, it follows that with the premixing of the gases, conservation of volume will also be assumed. With this assumption, the actual fuel to air ratio from Equation 4.10 can be expressed as a series of densities and volumes.

$$\rho_f V_f = \rho_{H_2} V_{H_2} + \rho_{CH_4} V_{CH_4}$$

$$\frac{m_f}{m_a} = \frac{\rho_f V_f}{\rho_a V_a}$$

$$\frac{\rho_{H_2} V_{H_2} + \rho_{CH_4} V_{CH_4}}{\rho_a V_a} = \frac{\phi}{b}\frac{MW_f}{MW_a} \tag{4.13}$$

For a gaseous mixture, the molecular weight of the mixture is the weighted sum of the molecular weights of the components. Using this definition, MW_f is expanded and the expression is simplified until Equation 4.14—a relationship for the volumetric ratio of air to hydrogen—is obtained.

$$MW_f = \frac{n_{CH_4}}{n_f} MW_{CH_4} + \frac{n_{H_2}}{n_f} MW_{H_2}$$

$$MW_f = \frac{b}{\phi}\left(\frac{n_{CH_4}}{n_a} MW_{CH_4} + \frac{n_{H_2}}{n_a} MW_{H_2}\right)$$

$$\frac{\rho_{H_2} V_{H_2} + \rho_{CH_4} V_{CH_4}}{\rho_a V_a} = \frac{\phi}{b}\frac{1}{MW_a} \cdot \frac{b}{\phi}\left(\frac{n_{CH_4}}{n_a} MW_{CH_4} + \frac{n_{H_2}}{n_a} MW_{H_2}\right)$$

$$\frac{V_a}{V_{H_2}} = \left[\frac{\rho_{H_2}}{\rho_a} + \frac{\rho_{CH_4}}{\rho_a}\frac{V_{CH_4}}{V_a}\right]\left[\frac{n_{H_2}}{n_a}\left(\frac{MW_{H_2} - MW_{CH_4}}{MW_a}\right) + \frac{\phi}{b}\frac{MW_{CH_4}}{MW_a} + \right]^{-1} \tag{4.14}$$

At this point, all of the terms required for the evaluation of the density and viscosity of the three-component gaseous mixture have been expressed in terms of known quantities. Beginning with Equations 4.4 and 4.6, the expressions for mixture density and viscosity have been simplified for a methane-hydrogen-air reactance mixture, and are shown in Equations 4.15 and 4.16, respectively.

$$\rho_m = \frac{\rho_{H_2} + \rho_{CH_4}\frac{V_{CH_4}}{V_{H_2}} + \rho_a\frac{V_a}{V_{H_2}}}{1 + \frac{V_{CH_4}}{V_{H_2}} + \frac{V_a}{V_{H_2}}} \tag{4.15}$$

$$\mu_m = \frac{\mu_{H_2}\sqrt{MW_{H_2}} + \mu_{CH_4}\frac{n_{CH_4}}{n_{H_2}}\sqrt{MW_{CH_4}} + \mu_a\frac{n_a}{n_{H_2}}\sqrt{MW_a}}{\sqrt{MW_{H_2}} + \frac{n_{CH_4}}{n_{H_2}}\sqrt{MW_{CH_4}} + \frac{n_a}{n_{H_2}}\sqrt{MW_a}} \tag{4.16}$$

In summary, Table 4.2 exhibits the equations required to find the mixture density and dynamic viscosity for a three-component gas mixture consisting of methane, hydrogen, and air.

Table 4.2: Equations needed in determining mixture density and viscosity of a methane-hydrogen-air gas mixture for known volume fraction of hydrogen and equivalence ratio

Quantity of Interest	Equation Number
V_{CH_4}/V_{H_2}	(4.8)
n_{CH_4}/n_{H_2}	(4.9)
n_{H_2}/n_a	(4.12)
V_a/V_{H_2}	(4.14)
ρ_m	(4.15)
μ_m	(4.16)

4.2.1.3 Burner Diameter and Flow Conditions

By definition, the kinematic viscosity, v, is defined as the ratio between the dynamic viscosity, μ, and the density of the fluid, ρ. Using the derived expressions, the mixture density and dynamic viscosity are determined for the operating conditions utilized in the current work with a 2.54 cm LSB and Emadi's work[17] with a 3.81 cm LSB. By equating the global Reynolds number (Equation 2.10) for the 3.81 cm LSB and the 2.54 cm LSB, the condition required for similarity is shown in Equation 4.17. Notice that the scaling relationship is dependent on the kinematic viscosities of each of the systems, which can be determined using the previously described expressions. As a reference, however, kinematic viscosities resulting from the derived mixture properties have been

tabulated, and are shown in Appendix C.

$$\frac{\bar{U}_{2.54}}{\bar{U}_{3.81}}\frac{\nu_{3.81}}{\nu_{2.54}} = 1.5 \tag{4.17}$$

Operating conditions shown in Table 4.3 were utilized. In examining $Re_{2.54}$ and $Re_{3.81}$, however, these flow conditions still produce valid results. For the operating conditions shown for $\alpha_{H_2} = 0$, the Reynolds number fell within 0.6% of $Re_{3.81}$. For the hydrogenated fuel ($\alpha_{H_2} = 0.2$), $Re_{2.54}$ is within 2.1% of $Re_{3.81}$. Due to the potential for lower error between the Reynolds numbers, current flame structure results will be validated by comparing the observed trends with those established by previous investigations of flame structures in premixed, turbulent combustion systems.[17,20,21,23,120] With this validation, results from the current work will be compared to prior investigations to examine the effect of burner diameter of flame structures.

Table 4.3: Flow parameters and characteristic Reynolds number for the operating conditions shown

D_{LSB} $[cm]$	$\bar{U}$ $[m/s]$	α_{H_2}	ϕ	Re $[\times 10^4]$
3.81	10	0	0.75	26,400
3.81	10	0.2	0.65	39,900
2.54	15	0	0.9	26,200
2.54	15.4	0.2	0.75	40,800
2.54	10	0	0.85	17,500
2.54	10	0.1	0.85	26,600
2.54	10	0.2	0.85	26,300

4.2.2 Flame Front Curvature

After finding the edge of the boundary for one image using the process depicted in Figure 4.11, the flame front curvature was determined at equidistant points along the flame edge using Equation 2.13. For nearly all operating conditions, 900 images were analyzed to create the sample population of flame front curvature. For one set of 300 images that was collected, the chamber pressure was sufficiently lower than ideal, so only 600 images were analyzed for the condition operating with pure methane fuel at a chamber pressure of 2 bar. A simple statistical analysis was performed on each population of data, and the PDF for each set of operating conditions was formulated. When discussing curvature results, the width of a PDF to which the discussion will refer is, for any given set of operating conditions, determined using a normalized PDF for a probability density of 0.5. Graphically, this width is depicted in depicted in Figure 4.12. Normalization is performed by scaling results by the maximum value of flame front curvature so that the upper limit within the PDF distribution is unity. Quantitative results for PDF distribution width and other characteristics of the distribution are shown in Table 4.4. In presenting distinguishing characteristics of the curvature distributions, μ_h and σ_h are the mean and standard deviation of the sample population, respectively, and W gives the width of the normalized curvature PDF. In presenting μ_h and σ_h, units are not presented due to a discrepancy within the MATLAB code used to determine flame front curvature. However, units are consistent for all statistics-related results presented. With the imposed time constraints, further analysis of the units within this MATLAB analysis was outside the current scope of work. Then, future work will require further consideration and alteration of the employed algorithm.

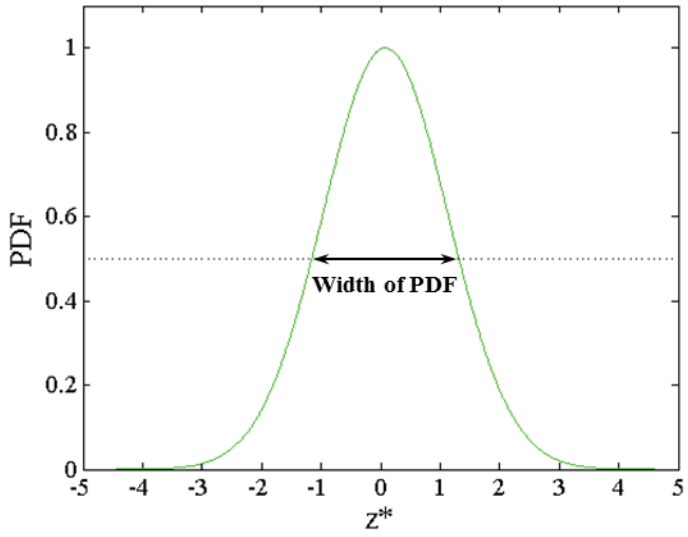

Figure 4.12: Graphical definition of PDF width

PDF shown is for pure methane fuel in the 2.54 cm LSB operating at a chamber pressure of 2 bar.

Table 4.4: Quantitative results and characteristics of flame front curvature PDF distributions for the 2.54 cm LSB

α_{H_2}	p [bar]	Re	W	μ_h	σ_h
0	1	26,200	0.816	0.0200	0.347
0	1.5	26,200	1.129	0.0372	0.480
0	2	26,200	2.476	0.0788	1.051
0.2	1	40,800	0.732	0.0134	0.311
0.2	1.5	40,800	0.901	0.0271	0.383
0.2	2	40,800	0.935	0.0301	0.397
0	1	17,500	0.874	0.0240	0.371
0.1	1	26,600	0.807	0.0251	0.342
0.2	1	26,300	0.882	0.0330	0.374

In Figure 4.13 and Figure 4.14, the PDFs of flame front curvature are shown for constant chamber pressure and constant reactant mixture composition, respectively. These results are used to confirm a similarity in the generalized trends exhibited trends established in previous work.[17,20,120]

In Figure 4.13, the curvature distributions are shown for a varying volume fraction of hydrogen at atmospheric pressure. From previous examinations of the flame front curvature, it is expected that an increase in hydrogen within the fuel mixture would result in smaller scale wrinkling (as shown in Figure 2.3) and a broadening of the PDF distribution. However, for the results shown in Figure 4.13, the intermediate fuel mixture ($\alpha_{H_2} = 0.1$) has a slightly slimmer distribution, with a width that is approximately 8% less than either the methane fuel or the $\alpha_{H_2} = 0.1$ fuel. With these two cases, the observed distribution width is very similar, which is contrary to what is expected by previously established trends. That is, the cases shown in Figure 4.13 do not display the PDF broadening expected with an addition of hydrogen. This discrepancy is likely due to uncontrollable fluctuations in the fuel and air flow rates. For some of the operating conditions summarized in Figure 4.13, external weather conditions were fairly inconsistent. Additionally, it was later determined that facilities management had been performing routine maintenance and construction within the building's heating, ventilation, and air conditioning (HVAC) system, which supplies the compressed air for the reactant mixture and chamber coflow. During data collection, uncontrollable fluctuations in both air and methane flow rates were observed, which are likely due to a combination of these disturbances to the system. Discussions regarding the effect of burner size on flame front curvature do not include results from the operating conditions shown in Figure 4.13. However, these results will be reviewed further in discussion on the flame surface density.

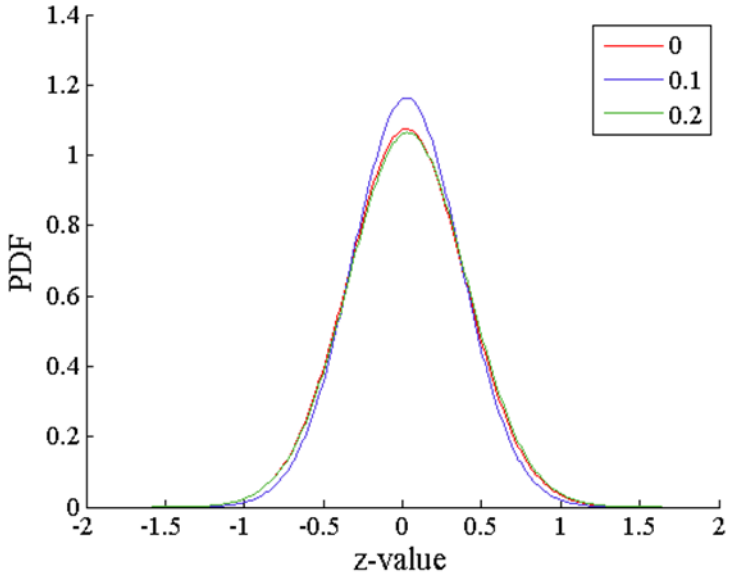

Figure 4.13: PDFs of flame front curvature at atmospheric pressure

If instead, the conditions are transposed such that the fuel composition is held constant and the effect of chamber pressure is examined, flame front curvature results for the 2.54 LSB are shown in Figure 4.14. For both fuel mixtures, an increase in chamber pressure results in a corresponding increase in width of the curvature distribution, indicating an increasing presence of smaller-scale wrinkles within the flame front. This observed trend is in agreement with trends that have been established for a variety of premixed, turbulent combustion systems.[17,21,120] Between the two fuel mixtures shown, this increase in distribution width is more pronounced for the pure methane fuel than for the $\alpha_{H_2} = 0.2$ methane-hydrogen fuel mixture. PDF distributions for curvature from Halter's Bunsen burner investigation, Emadi's investigation of a 3.81 cm burner, and Soika's examination of using a bluff-body stabilized combustor are shown in Figure 4.15 to illustrate the expected trends.

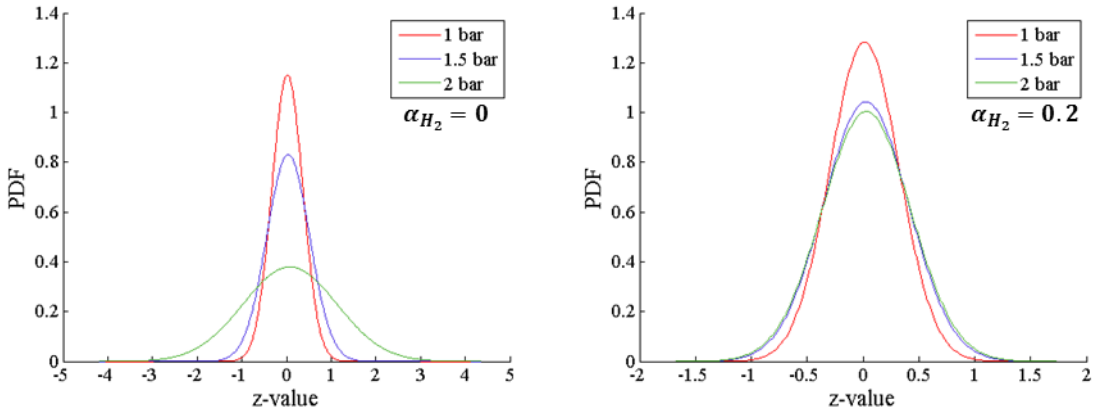

Figure 4.14: PDFs of Flame Front Curvature for consistent fuel composition

Quantitatively, both fuel mixtures in the current work exhibit an overall percentage increase if the chamber pressure is increased from 1 bar to 2 bar. For the mixed fuel, an overall percentage change of 27.8% was observed, and for the methane flame, the overall percentage increase was 203.3%. A number of factors could be responsible for the order of magnitude difference. Primarily, flow conditions for each of these sets of operating conditions were designed not for direct comparison to each other, but rather to satisfy similarity conditions with the 3.81 cm LSB, as well as to examine the nature of the flame front curvature and validate the existence of previously established trends. With this validation, results obtained in the current work are compared to results obtained by Emadi.[17] Results showing the effect of hydrogen addition are not compared with the Halter's examination[120] due to the inconclusive trend that was observed.

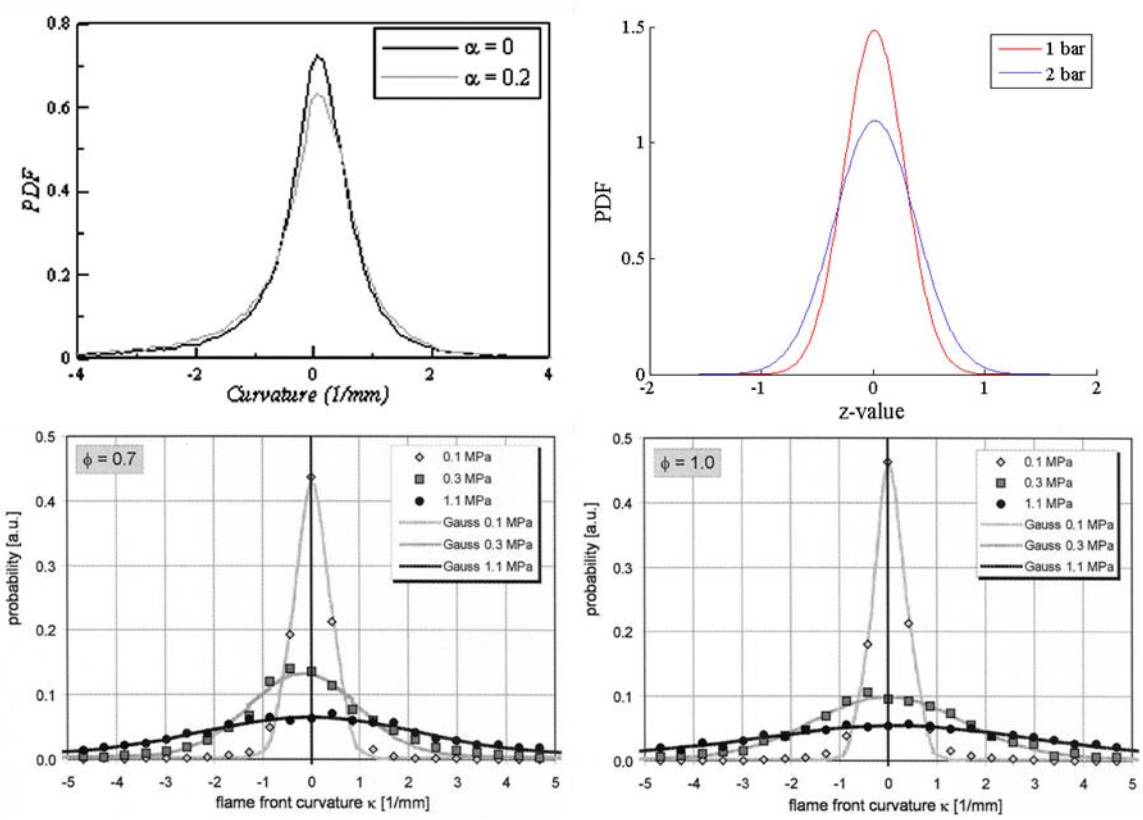

Figure 4.15: Flame front curvature distributions from the work of Halter, Emadi, and Soika

---

Source:
Top Left: [120], p = 15 bar
Top Right: Adapted from [17], binary methane-air reactant mixture.
Bottom: Adapted from [21]

To investigate the effect of burner diameter on flame front curvature, PDF widths and distribution statistics are shown in Table 4.5, and results for both the 2.54 cm LSB and the 3.81 cm LSB are shown graphically in Figure 4.16. For all cases examined, a decrease in burner diameter results in a broadening of the curvature distribution. Using the results from the 3.81 cm LSB as a reference, the percentage increase in PDF width for

the 2.54 cm LSB is shown to be dependent on both the fuel composition and the chamber pressure. With the exception of the results for $\alpha_{H_2} = 0.2$ at 2 bar, increase in PDF width is on the order of 10%, with exact percentage increases ranging from 7.8% to 29%. For $\alpha_{H_2} = 0.2$ at 2 bar, the increase is on the order of 100%, with a percentage increase of 188.8%. Relative percentage increases are shown in Table 4.6. Within this table, the characteristic Reynolds number for a set fuel mixture and chamber pressure is represented by the average of $Re_{2.54}$ and $Re_{3.81}$. In addition to observing broader distributions of curvature with the smaller-diameter LSB, the mean curvature within the flame front increases as well, suggesting that the wrinkling structures within the flame front of the 2.54 cm LSB are of a smaller scale than those present for the 3.81 cm LSB.

Table 4.5: Quantitative results and characteristics of flame front curvature distributions for the 2.54 cm LSB and the 3.81 cm LSB

α_{H_2}	p [bar]	D_{LSB} [cm]	Re	W	μ_h	σ_h
0	1	3.81	26,400	0.633	0.0131	0.269
0	1	2.54	26,200	0.816	0.0200	0.347
0	2	3.81	26,400	0.858	0.0177	0.364
0	2	2.54	26,200	2.476	0.0788	1.051
0.2	1	3.81	39,900	0.633	0.0122	0.269
0.2	1	2.54	40,800	0.732	0.0134	0.311
0.2	2	3.81	39,900	0.868	0.0164	0.368
0.2	2	2.54	40,800	0.935	0.0301	0.397

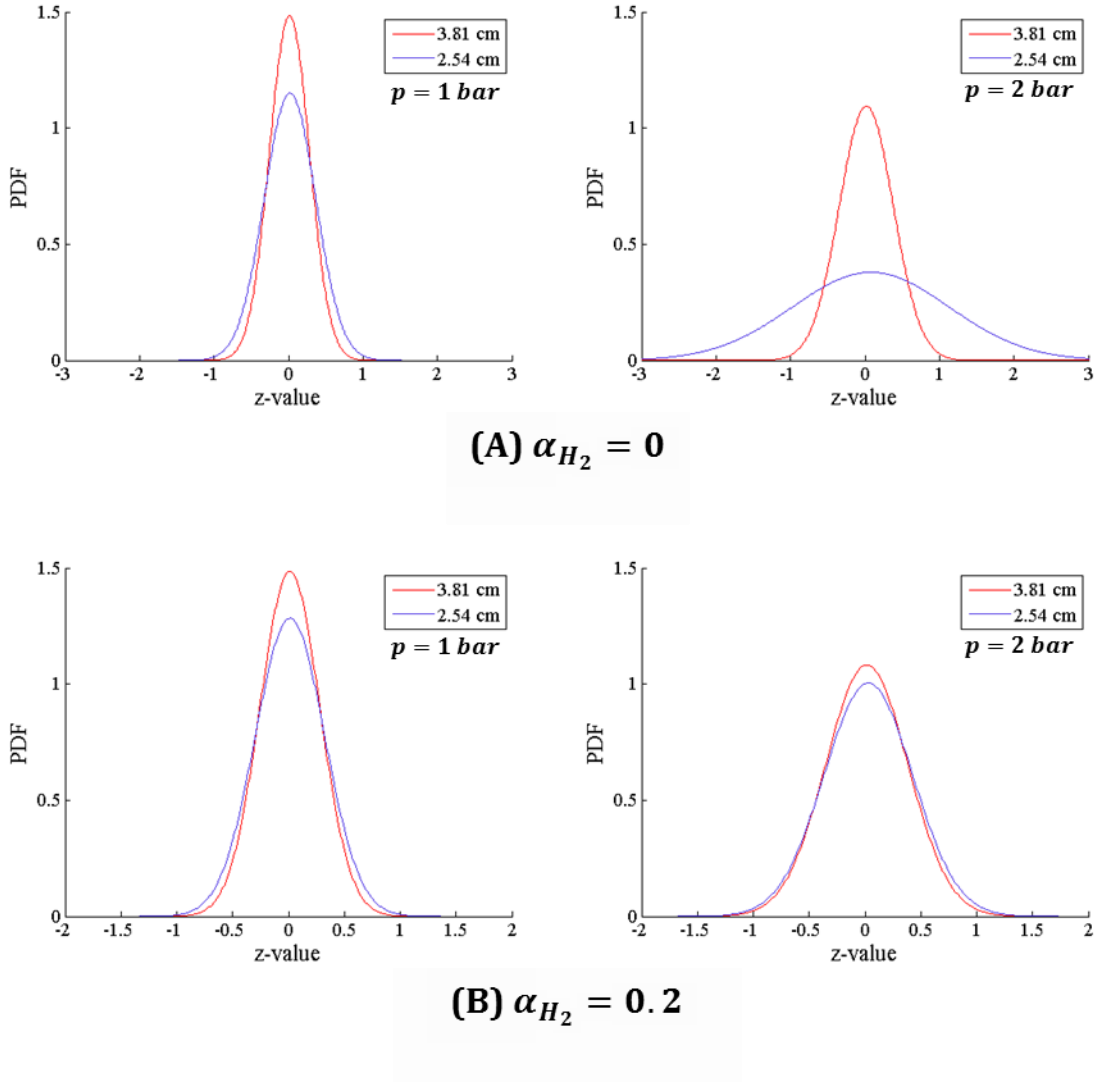

Figure 4.16: Flame front curvature for a 2.54 cm LSB and a 3.81 cm LSB

Note:

For binary mixture, Reynolds numbers for 3.81 cm LSB system and 2.54 cm LSB are 26,400 and 26,200, respectively.

For three-component mixture, Reynolds numbers for 3.81 cm LSB system and 2.54 cm LSB are 39,900 and 40,800, respectively.

Table 4.6: Quantitative results and characteristics of flame front curvature distributions for the 2.54 cm LSB and the 3.81 cm LSB

$\boldsymbol{Re}$	$\boldsymbol{\alpha_{H_2}}$	$\boldsymbol{p}$ **[bar]**	$\boldsymbol{(W_{2.54} - W_{3.81})/W_{3.81}}$ **[%]**
26,300	0	1	29.0%
26,300	0	2	188.7%
40,300	0.2	1	15.6%
40,300	0.2	2	7.9%

4.2.3 Flame Surface Density

After the edge of the flame was detected using the Canny edge detection algorithm, an analysis was performed to create a pictorial representation of the flame brush. Using MATLAB, the probability of an edge falling within a given region was analyzed, and processed to create 10 mean progress variable ($\langle c \rangle$) contours. With this completed a polynomial fit (of an even degree) was applied to create a smoother set of progress variable contours. An example of a flame brush, the raw contours, and the resulting smoothed contours are shown in Figure 4.17. For most sets of operating conditions, using a 4th degree polynomial was sufficient to produce progress variable contours that did not overlap. Occasionally, however, if a 4th degree polynomial produces curves with an incorrect concavity (i.e. concave down) or produces progress curves that overlap, a higher polynomial was used. From this point, the upper portion of the flame is separated from the lower portion, as including the transition from the OH-rich region to the burnt combustion products above the flame would skew results. Here, MATLAB is used to sum the length of the flame edges and areas between the mean progress variable polynomial curves for use in Equation 2.14. Again, with the exception of a single case

(100% methane with a chamber pressure of 2 bar), 900 images were processed for each set of operating conditions, results are shown in Figure 4.18 – Figure 4.20.

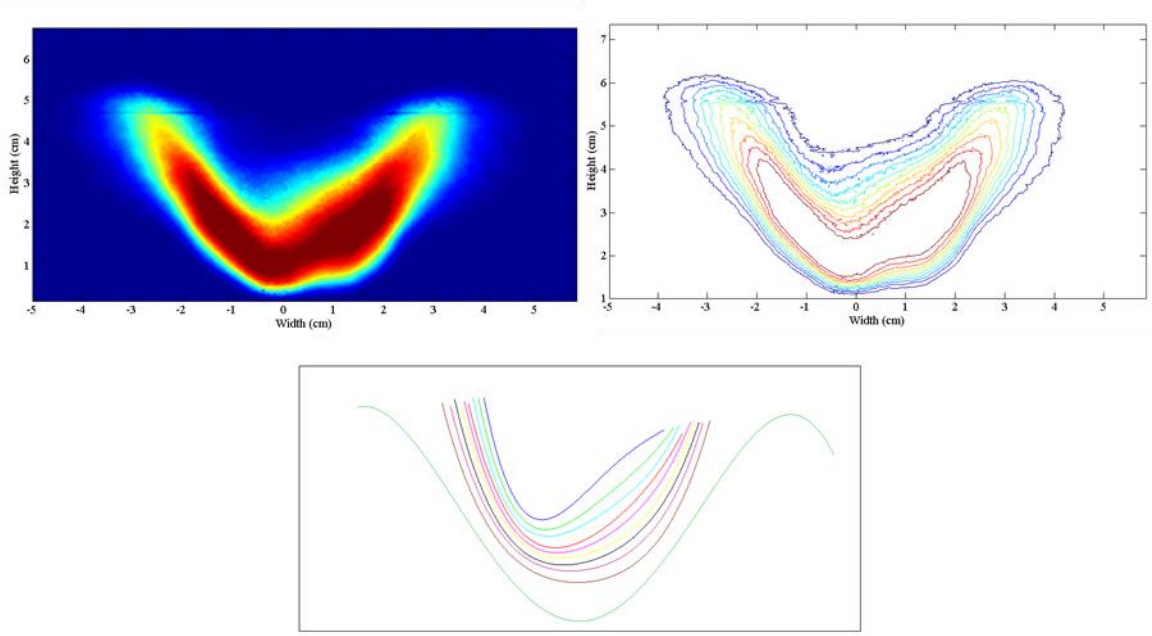

Figure 4.17: Representative flame brush, flame brush contours, and resulting 4th degree polynomial contours

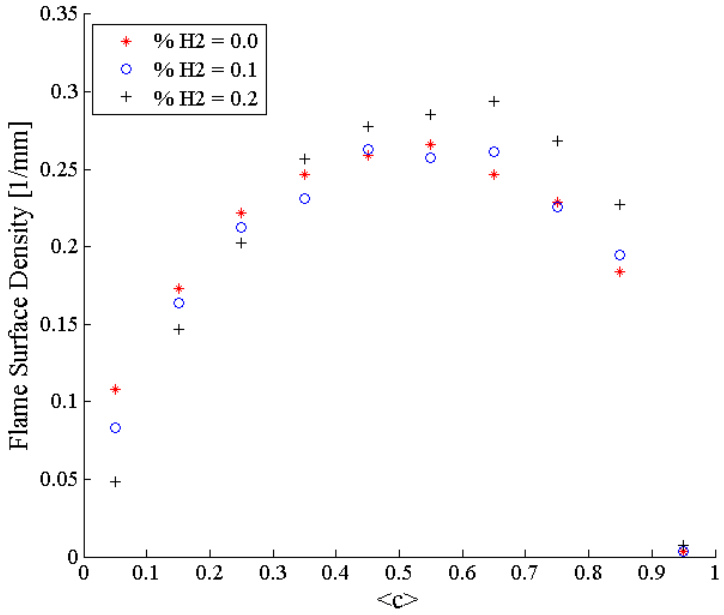

Figure 4.18: Flame surface density at atmospheric pressure

For similar flow conditions and an atmospheric chamber pressure, increasing the volume fraction of hydrogen from 0 to 0.2 results in a slight increase in FSD near the peak of the parabolic results shown. However, for smaller mean progress variables, the opposite was observed. An increase in FSD was observed when decreasing the volume fraction of hydrogen within the reactant mixture. In both scenarios, however, FSD for the intermediate fuel mixture ($\alpha_{H_2} = 0.1$) more closely resembles results for the pure methane. Then, even though this set of FSD results (which corresponds operating conditions associated with curvature results shown in Figure 4.13) exhibits the parabolic trend observed by others, but no apparent trend exists between increasing the volume fraction of hydrogen in the reactant mixture and the FSD distribution.

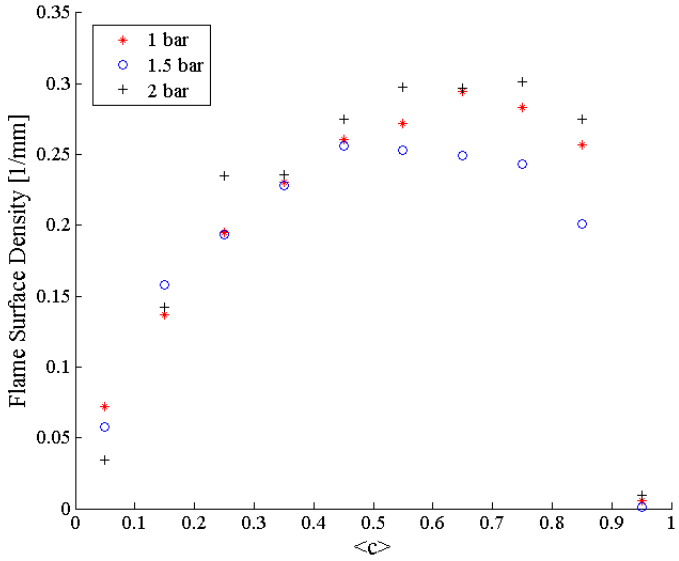

Figure 4.19: Flame surface density for a consistent fuel mixture of 80% CH_4 and 20% H_2

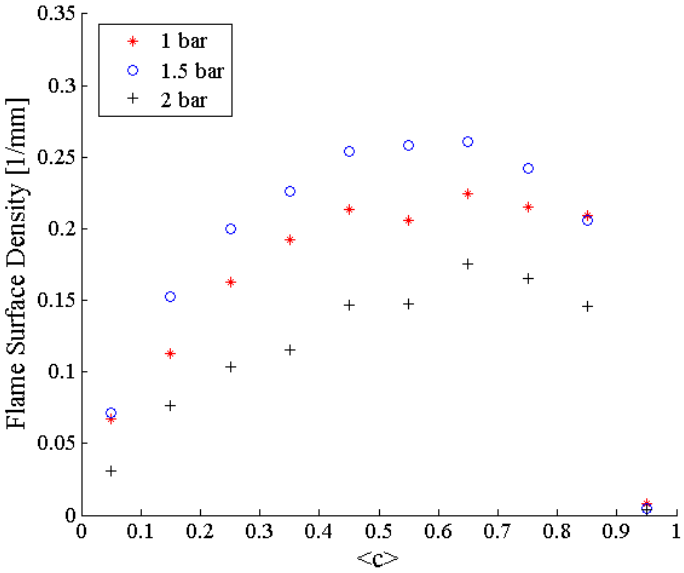

Figure 4.20: Flame surface density for a 100% CH_4 fuel mixture of

For all results shown, distributions for the FSD display the parabolic trend observed by Halter[120] for a Bunsen burner configuration, Guo[23] for a V-shaped flame, Shepherd[20] for an intense turbulence LSB (diameter unknown), and Emadi[17] for a 3.81 cm diameter LSB. Halter, Shepherd, and Guo's FSD results are shown in Figure 4.21. For Halter and Emadi, adding hydrogen to the fuel mixture resulted an overall increase in the values observed within FSD distributions. Guo, however, observed the opposite trend, and demonstrated a decrease in FSDs with an increase in hydrogen. As shown, no conclusive trend is observed for the FSD results shown in Figure 4.18, so results do not agree with those presented by Halter, Guo, or Emadi.

For a constant fuel composition, however, the effect of chamber pressure on FSD observed in the current results is much more indicative of the trend established by Emadi for a 3.81 cm LSB. For a constant hydrogen volume fraction, Emadi observed that an increase in chamber pressure resulted in a corresponding increase in the values within the FSD distribution.[17] In the current work, this is best represented by the results of the pure methane flame, which are exhibited in Figure 4.20. The quality of the trend for the hydrogenated fuel ($\alpha_{H_2} = 0.2$) is not as apparent. This is most likely due to the methodology used within MATLAB to formulate the flame surface density. In performing the horizontal division between the upper and lower portion of the flame, the process is highly variable and dependent on the shape of the flame brush. With this method, the flames that produce the best results using this method are those with a sufficiently clear horizontal cut through the highest-intensity [OH] region within the flame brush. Due to natural motion of the flame, some sets of images are such that the horizontal cut is sufficient and produces the expected results. However, depending on the nature of the flame brush, the size and motion of the flame may be such that no horizontal cut can be made through the highest-[OH] intensity region of the flame brush.

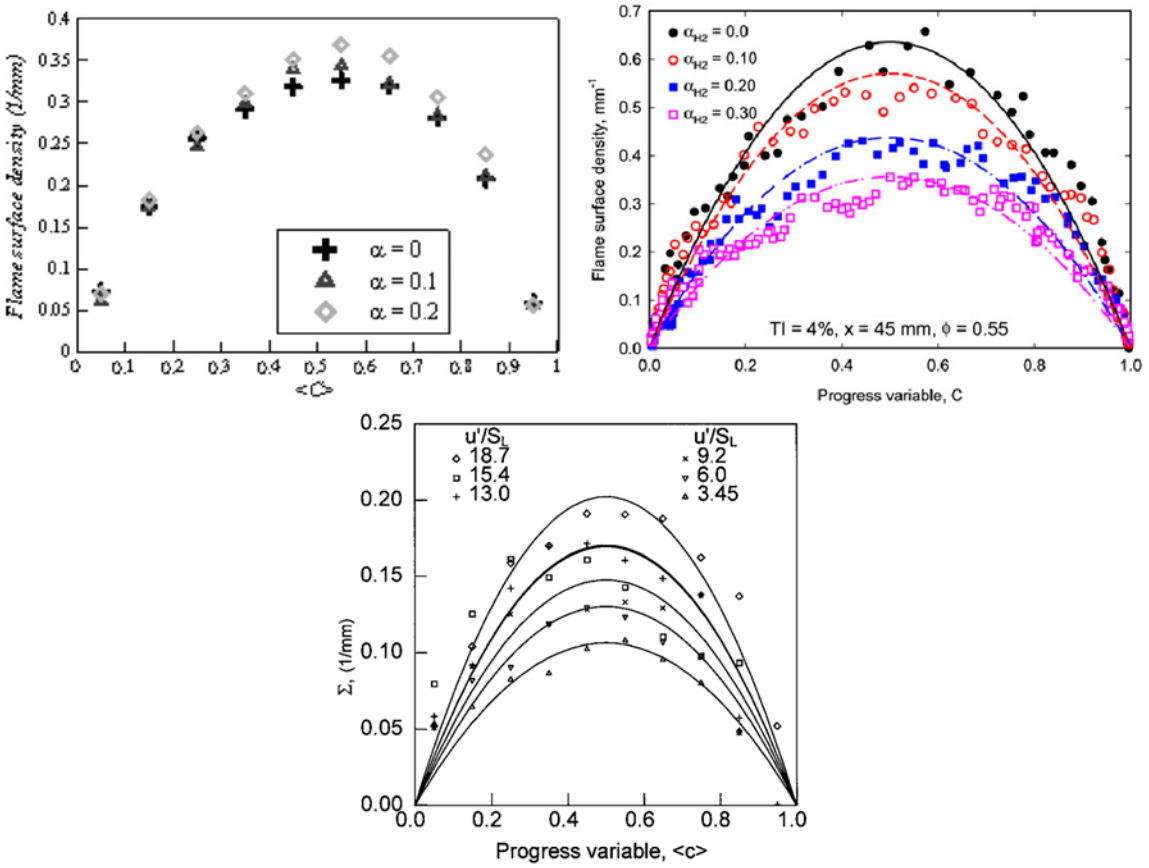

Figure 4.21: FSD results from Halter (Bunsen burner), Guo (V-shaped flame), and Shepherd (Intense turbulence LSB)

Source:
Left: [120]
Right: [23]
Bottom: [20]

To account for the natural motion of the flame reflected in the OH-PLIF images and the resulting flame brush, the algorithm could be altered such that in place of linearly separating the upper portion of the flame, a curved, parabolic cutting scheme is implemented instead. To adjust for the variability of flame motion within each set of

images, this could be performed using a specified polynomial as a reference for the curved cut. For example, MATLAB could implement a parabolic cut based on the $\langle c \rangle = 0.6$ contour resulting from a 2nd degree polynomial fit to the flame brush contours, such as those shown in Figure 4.17. However, the implementation and confirmation of validity of this proposed algorithm is beyond the scope of the current work, and is instead left as a topic for future investigation of flame structures in low swirl burners.

Because they exhibited trends that coincided with those predicted by previous examinations of flame surface density, only the results for $\alpha_{H_2} = 0$ will be examined in the discussion of the effect of burner size on flame surface density. For $\alpha_{H_2} = 0$ at atmospheric and elevated pressure conditions, FSD distributions for both the 2.54 cm burner and the 3.81 cm burner are shown in Figure 4.22.

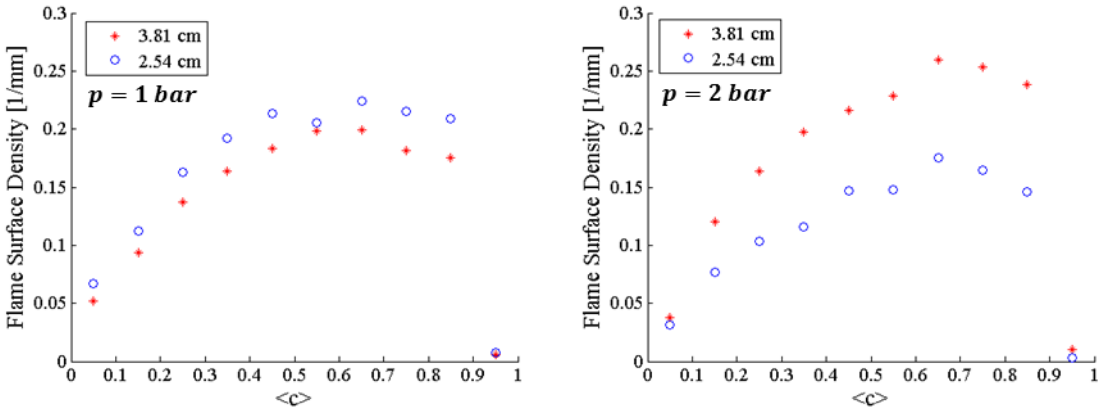

Figure 4.22: Flame surface density for a 2.54 cm LSB and a 3.81 cm LSB with a consistent 100% CH_4 fuel mixture

---

Note:

For binary mixture, Reynolds numbers for 3.81 cm LSB system and 2.54 cm LSB are 26,400 and 26,200, respectively.

For three-component mixture, Reynolds numbers for 3.81 cm LSB system and 2.54 cm LSB are 39,900 and 40,800, respectively.

Unlike the flame front curvature, a clear relationship does not appear to exist between the current 2.54 cm LSB results and the results for a 3.81 cm burner. At atmospheric pressure, FSD results for the 2.54 cm LSB are between 3.5% and 31% higher than results for the 3.81 cm LSB. However, at the elevated chamber pressure, the 2.54 LSB exhibits FSD results between 16.5% and 66% lower than those for the 3.81 cm burner.

CHAPTER 5

SUMMARY AND CONCLUSIONS

In furthering the understanding of the characteristics of a 2.54 cm LSB and associated combustion instability, a series of analyses were performed to compile data for methane and mixed methane-hydrogen fuel flames. In the first series of assessments, a flame operating under a strict set of conditions was initially at atmospheric pressure. The pressure of the chamber was elevated until the initially bowl-shaped flame inverted and flashed back to attach to the swirler at the inlet of the burner. In the resulting examination of the pressure limits associated with flashback, general trends between the flashback pressure and the bulk flow velocity were as anticipated. From a simple theoretical analysis involving thermodynamic relations and basic combustion theory, increasing the bulk flow of the velocity was expected to raise the limiting flashback pressures of the system. Experimental results from the examination on flashback were in agreement with the predicted trend. That is, as the bulk flow velocity was increased, the upper pressure limits that caused flashback were seen to rise. Predictions regarding alternative parameters and the effect on flashback limits were developed using others' examinations into stability limits for lean, premixed combustors. Here, the trends observed for the current work exactly resembled the formulated predictions. Compared to a pure methane flame, the methane-hydrogen mixture flame exhibited lower flashback pressures for an increasing bulk flow velocity. This is likely due to hydrogen addition reducing the Lewis number of the flame, which decreases the flame's resistance to stretching along the flame front. Finally, with an increase in the equivalence ratio of the bulk flow, flames were observed to flash back at lower pressures. This is in agreement with many results that have been previously attained for many fundamentally different experimental setups with different burner configurations.

In investigating the lean blowout limits of the 2.54 cm LSB flame, results were compared to many similar analyses that have been previously performed. With a singular exception, trends observed within the current work's examination of LBO limits matched those attained in previous years. As such, an increase in the percent of hydrogen within the fuel mixture resulted in a decrease in the observed LBO limits. Additionally, an increase in the chamber pressure was also shown to decrease the LBO limits within the pure methane flame. However, an anomaly existed in the mixed methane-hydrogen flame, and this trend was not clearly observed. This irregularity is likely due to the increased pace at which tests must be performed with the mixed flames (to maintain speaker temperatures below their melting point) or construction within the building's HVAC system. Then, it is likely that chamber pressure fluctuations were still occurring within the chamber as the equivalence ratio was decreased to locate the LBO limits. Comparisons between the 2.54 cm LSB and the 3.81 cm LSB were achieved by scaling the bulk flow velocity by the outlet area of the burners, and it was found that the magnitude of the equivalence ratio at the onset of instability and LBO extinction was very similar for the two differently-sized burners. Similarly, both burners' differential equivalence ratios (from the onset of instability to extinction) were of the same order of magnitude, and appeared to be directly correlated to the size of resolution of the equivalence ratio decrement.

In preparation of examining the effect of burner diameter on flame structures, it was shown that properties of the flow were dependent on the composition and equivalence ratio of the reactant mixture, and could be determined for binary methane-air gas mixtures and for methane-hydrogen-air mixtures using known parameters, such as species' densities, viscosities, and molecular weights. With this derivation, the condition for Reynolds number similarity was expressed, and it was shown that for the current work, Reynolds numbers were within 2% of those characterizing the flow field utilized in work with the 3.81 cm burner.[17] Well-established relationships between chamber pressure

and flame front curvature from previous examinations[17,20,120] were used to in validation of the current curvature results. With this confirmation, current results for the 2.54 cm LSB were compared to results for the 3.81 cm LSB presented by Emadi.[17] For the majority of operating conditions compared, the breadth of the curvature distribution in the current study was shown to be of O(10%) wider than the curvature distributions for the 3.81 cm LSB. This, in conjunction with the observation that the average curvature within the front is higher in the smaller-diameter burner, demonstrates that wrinkles within the 2.54 cm LSB flame front are of a smaller scale than those within the 3.81 cm flame front. In examinations of the flame surface density, the current results displayed the expected parabolic nature when moving across the flame brush, but with the exception of one set of operating conditions, the additional expected trends were not observed. A potential modification to the post processing algorithm used in determining FSD was proposed but not investigated, as it is outside of the current scope of work. As comparisons were performed between the 2.54 cm LSB and the 3.81 cm LSB, no apparent relationship was found to exist between burner diameter and flame surface density.

5.1 Future Work

In extending and clarifying the results presented in the current work, it would be beneficial for future work to establish a more involved method of comparing burners of different diameters. The Reynolds number is useful, but only considering Reynolds number intensity does not account for other important aspects of the flame, including heat release. With an alternative method of scaling that considers both the turbulent intensity and the heat release of a system, resulting comparisons between burner diameters will—in terms of the physical phenomena occurring in the combustion—be more accurate.

To confirm the comparison in LBO limits of the 2.54 and the 3.81 cm LSB, results from the current work should be used to predetermine ranges of equivalence ratios, and subsequently use a smaller equivalence ratio increment (most likely 0.25) between operating conditions.

In future examinations of the flame structure (for both flame front curvature and flame surface density), observed trends in the current work can be confirmed and refined by re-adjusting inlet flow parameters to minimize the difference between characteristic Reynolds numbers. In MATLAB, analyses should be performed to determine the units produced for post processing associated with flame front curvature, and alterations should be made accordingly. Additionally, future investigations into the FSD of a system should consider the potential for modifying the cutoff algorithm currently utilized. Instead of implementing a horizontal separation between the upper and lower section of the flame, a parabolic cutting mechanism using the mean progress variable contours may produce more consistent results. Of course, any modifications made to the post processing should be validated to ensure that results align with expected trends and results.

Within the behind-the-scenes effort associated with the current work, the full range of operating conditions originally detailed in the experiment design was not fully explored due to unexpected equipment failure during the data collection process. Then, in examining the initial complete set of operating conditions, more concrete trends and results may be observed. In particular, some higher-velocity data was initially collected, but many more operating conditions could not be explored due to the required rotation of equipment within the data collection processes.

Procedurally, the experimental setup and operation of the apparatus as it stand now requires that the temperature of the speakers used in acoustic forcing must be monitored and maintained below a certain level to prevent melting. Even with the liquid nitrogen cooling system operating, extreme time limits are placed on the duration for which a flame can burn within the combustion chamber. This cooling system is effective

in cooling the speakers following the extinction of a flame, but with a revamped design, the speakers could potentially be cooled more efficiently during the period in which the flame is lit. With as rushed as the data collection process is currently, the accuracy of any information acquired is likely compromised. With a more effective solution for cooling the speakers in place, data acquisition will not likely be as rushed, and the resulting information will as a whole, be more accurate.

REFERENCES

1. Cheng, R.K., Yegian, D.T., Miyasato, M.M., Samuelsen, G.S, Benson, C.E., Pellizzari, R., and Loftus, P. "Scaling and development of low-swirl burners for low-emission furnaces and boilers." *Proc. Combust. Inst.* 28, No. 1 (2000): 1305-1313.

2. Bowman, C.T. "Control of combustion-generated nitrogen oxide emissions: Technology driven by regulation." In *Symp. (Int.) Combust.* 24, No. 1 (1992): 859-878. Elsevier.

3. Keller, J.J. "Thermoacoustic oscillations in combustion chambers of gas turbines." *AIAA Journal* 33, No. 12 (1995): 2280-2287.

4. Bradley, D., Gaskell, P.H., Gu, X.J., Lawes, M., and Scott, M.J. "Premixed turbulent flame instability and NO formation in a lean-burn swirl burner." *Combust. Flame* 115, No. 4 (1998): 515-538.

5. Brewster, B.S., Cannon, S.M., Farmer, J.R., and Meng, F. "Modeling of lean premixed combustion in stationary gas turbines." *Prog. Energy Combust Sci.* 25, No. 4 (1999): 353-385.

6. Lieuwen, T., Torres, H, Johnson, C., and Zinn, B.T. "A mechanism of combustion instability in lean premixed gas turbine combustors." *J. Eng. Gas Turb. Power* 123, No. 1 (2001): 182-189.

7. Lieuwen, T.C. and Yang, V. "Combustion instabilities in gas turbine engines (operational experience, fundamental mechanisms and modeling)." *Prog. Astronaut. Aeronaut.* (2005).

8. Dowling, A.P. and Morgans, A.S. "Feedback control of combustion oscillations." *Annu. Rev. Fluid Mech.* 37, (2005): 151-182.

9. Gupta, A.K., Lilley, D.G., and Syred, N. *Swirl flows*. Tunbridge Wells, Kent, England: Abacus Press, (1984).

10. Syred, N. and Beér, J.M. "Combustion in swirling flows: A review." *Combust. Flame* 23, No. 2 (1974): 143-201.

11. Cheng, R.K. and Levinsky, H. "Lean premixed burners." Chapter 6. In: Dunn-Rankin, D., ed. *Lean combustion: Technology and control*. Academic Press, (2008).

12. Chan, C.K., Lau, K.S., Chin, W.K., and Cheng, R.K., "Freely propagating open premixed turbulent flames stabilized by swirl." In *Symp. (Int.) Combust.* 24, No. 1 (1992): 511-218. Elsevier

13. Bedat, B. and Cheng, R.K. "Experimental study of premixed flames in intense isotropic turbulence." *Combust. Flame* 100, No. 3 (1995): 485-494.

14. Cheng, R.K. "Velocity and scalar characteristics of premixed turbulent flames stabilized by weak swirl." *Combust. Flame* 101, No. 1 (1995): 1-14.

15. Halter, F., Chauveau, C., Djebaili-Chaumeix, N., and Gökalp, I. "Characterization of the effects of pressure and hydrogen concentration on the laminar burning velocities of methane-hydrogen-air mixtures." *Proc. Combust. Inst.* 30, No. 1 (2005): 201-208.

16. Beerer D., McDonnell, V., Therkelsen, P, and Cheng, R.K. "Flashback, blow out, emissions, and turbulent displacement flame speed measurements in a hydrogen and methane fired low-swirl injector at elevated pressures and temperatures." In *ASME Turbo Expo 2012: Turbine Technical Conference and Exposition*. ASME, (2012): 113-124.

17. Emadi, M. "Flame structure and thermo-acoustic coupling for the low swirl burner for elevated pressure and syngas conditions." (PhD diss., The University of Iowa, 2012).

18. Turns, S.R. *An introduction to combustion: Concepts and applications.* 3rd Ed. New York: McGraw-Hill, (2012).

19. Cowie, M. and Watts, H. "Diffusion of methane and chloromethanes in air." *Can. J. Chem.* 49, No. 1 (1971): 74-77.

20. Shepherd, I.G., Cheng, R.K., Plessing, T., Kortschik, C., and Peters, N. "Premixed flame front structure in intense turbulence." *Proc. Combust. Inst.* 29, No. 2 (2002): 1833-1840.

21. Soika, A., Dinkelacker, F., and Leipertz, A. "Pressure influence on the flame front curvature of turbulent premixe flames: Comparison between experiment and theory." *Combust. Flame* 132, No. 3 (2003): 451-462.

22. Tang, B.H.Y. and Chan, C.K. "Simulation of flame surface density and burning rate of a premixed turbulent flame using contour advection." *Combust. Flame* 147, No. 1 (2006): 49-66.

23. Guo, H., Tayebi, B., Galizzi, C., and Escudié. "Burning rates and surface characteristics of hydrogen-enriched turbulent lean premixed methane-air flames." *Int. J. Hydrogen Energy* 35, No. 20 (2010): 11342-11348.

24. Poinsot, T. and Veynante, D. *Theoretical and numerical combustion.* RT Edwards, Inc., (2005).

25. Higgins, B. "On the sound produced by a current of hydrogen gas passing through a tube." *Journal of Natural Philosophy, Chemistry and the Arts* 1, (1802): 129-131.

26. Rijke, P.L. "LXXI. Notice of a new method of causing a vibration of the air contained in a tube open at both ends." *Lond. Edinb. Dubl. Phil. Mag.* 17, No. 116 (1859): 419-422.

27. Tyndall, J. "On the sounds produced by the combustion of gases in tubes." *J. Franklin Inst.* 64, No. 6 (1857): 404-409.

28. Tyndall, J. "XIV. On sounding and sensitive flames." *Lond. Edinb. Dubl. Phil. Mag.* 33, No. 221 (1867): 92-99.

29. Rayleigh J.W.S. *Theory of Sound, Vol. 1 & Vol. 2*. (1945).

30. Putnam, A.A. and Dennis, W.R. "Organ-pipe oscillations in a flame-filled tube." In *Symp. (Int.) Combust.* 4, No. 1 (1953): 566-575. Elsevier.

31. Putnam, A.A. and Dennis, W.R. "Burner oscillations of the gauze-tone type." *J. Acoust. Soc. Am.* 26, (1954): 716-725.

32. Chu, B.T. "On the energy transfer to small disturbances in fluid flow (Part I)." *Acta Mechanica* 1, No. 3 (1965): 215-234.

33. Zinn, B.T. "Pulse combustion: Recent applications and research issues." In *Symp. (Int.) Combust.* 24, No.1 (1992): 1297-1305. Elsevier.

34. Nicoud, F. and Poinsot, T. "Thermoacoustic instabilities: Should the Rayleigh criterion be extended to include entropy changes?" *Combust. Flame* 142, No. 1 (2005): 153-159.

35. Culick, F.E.C. "A note on Rayleigh's criterion." *Combust. Sci. Technol.* 56, (1987): 159-166.

36. Raun, R.L., Beckstead, M.W., Finlinson, J.C., and Brooks, K.P. “A review of Rijke tubes, Rijke burners and related devices.” *Prog. Energy Combust. Sci.* 19, No. 4 (1993): 313-364.

37. Barrère, M. and Williams, F.A. “Comparison of combustion instabilities found in various types of combustion chambers.” In *Symp. (Int.) Combust.* 12, No. 1 (1969): 169-181. Elsevier.

38. Putnam A.A. *Combustion driven oscillations in industry.* New York: American Elsevier Publishers, (1971).

39. Zel’dovich, Y.B. and Frank-Kamenetskii, D.A. “A theory of thermal propagation of flame.” *Zh. Fiz. Khim.* 12 No. 1 (1938): 100-105.

40. Darrieus, G. “Propagation d’un front de flame.” *La Technique Moderne,* (1938).

41. Landau, L.D. “On the theory of slow combustion.” *Acta Physicochim.,* No. 1 (1944): 77-85.

42. Clanet, C. and Searby, G. “First experimental study of the Darrieus-Landau instability.” *Phys. Rev. Lett.* 80, No. 17 (1988):3867.

43. Pelce, P. and Clavin, P. “Influence of hydrodynamics and diffusion upon the stability limits of laminar premixed flames.” *J. Fluid Mech.* 124, (1982): 219-237.

44. Markstein, G.H., Guenoche, H., and Putnam, A.A. “Nonsteady flame propagation.” (1964): 328.

45. Zel’dovich, A.B., Istratov, A.G., Kidin, N.I., and Librovich, V.B. “Flame propagation in tubes: Hydrodynamic and stability.” *Combust. Sci. Technol.* 24, No. 1-2 (1980):1-13.

46. Sivashinsky, G.I. “Diffusional-Thermal Theory of Cellular Flames.” *Combust. Sci. Technol.* 15, No. 3-4 (1977): 137-146.

47. Joulin, G. and Clavin, P. “Linear stability analysis of nonadiabatic flames: Diffusional-thermal model.” *Combust. Flame* 35, (1979):139-153.

48. Barenblatt, G.I., Zel’dovich, Y.B., and Istratov, A.G. “On thermal-diffusive stability of a laminar flame.” *Zh. Prikl. Mekh. Fiz.,* (1962): 21-26.

49. Gutman, S. and Sivashinsky, G.I. "The cellular nature of hydrodynamic flame instability." *Physica D.: Nonlinear Phenomena* 43, No. 1 (1990): 129-139.

50. Bastiaans, R.J.M., Vreman, A.W., and Pitsch, H. "DNS of lean hydrogen combustion with flamelet-generated manifolds." *CTR Annual Research Briefs 2007*, (2007): 195.

51. Giacomazzi, E., Picchia, F.R., and Arcidiacono, N. "A review of chemical diffusion, criticism and limits of simplified methods for diffusion coefficients calculation." *Combust Theory Model.* 12, (2008): 135-158.

52. Williams, G. *Combustion theory*. (1985).

53. Emadi, M., Karkow, D., Melendez, A., and Ratner, A. "Parameter variations and the effects of hydrogen: An experimental investigation in a lean premixed low swirl combustor." *Int. J. Hydrogen Energy* 38, No. 13 (2013): 5401-5409.

54. Joulin, G. and Mitani, T. "Linear stability analysis of two-reactant flames." *Combust. Flame* 40, (1981): 235-246.

55. Friz, J., Kroner, M., and Sattelmayer, T. "Flashback in a swirl burner with cylindrical premixing zone." *J. Eng. Gas Turb. Power* 126, No. 2 (2004): 276-283.

56. Von Elbe, G. and Mentser, M. "Further studies of the structure and stability of burner flames." *J. Chem. Phys.* 13, No. 2 (2004):89-100.

57. Wohl, K. "Quenching, flash-back, blow-off—Theory and experiment." *4th Symp. (Int.) Combust.*, The Combustion Institute, Pittsburgh, PA, (1952): 69-89.

58. Eichler, C., Baumgartner, G., and Sattelmayer, T. "Experimental investigation of turbulent boundary layer flashback limits for premixed hydrogen-air flames confined in ducts." *J. Eng. Gas Turb. Power* 134, No. 1 (2012).

59. Gökalp, I. "On the correlations of turbulent burning velocities." *Combust. Sci. Technol.* 23, (1980): 137-142.

60. Liu, Y. and Lenze, B. "The influence of turbulence on the burning velocity of premixed CH_4 – H_2 flames with difference laminar burning velocities." In *Symp. (Int.) Combust.* 22, No. 1 (1989):747-754. Elsevier.

61. Abdel-Gayed, R.G., Bradley D., Hamid, M.N., and Lawes M. "Lewis number effects on turbulent burning velocity." *Proc. Combust. Inst.* 20, (1984): 505-512.

62. Koroll, G.W., Kumar, R.K., and Bowles, E.M. “Burning velocities of hydrogen-air mixtures.” *Combust. Flame* 94, No. 3 (1993): 330-340.

63. Guin, C. “Characterization of autoignition and flashback in premixed injection systems.” *AVT Symp. On Gas Turbine Engine Combustion, Emission and Alternative Fuels,* Lisbon, Portugal, (1998).

64. Kiesewetter, F., Hirsch, C., Fritz, J., Kroner, M., and Sattelmayer, T. “Two-dimensional flashback simulation in strongly swirling flows.” In *ASME Turbo Expo 2003, collocated with the 2003 Int. Joint Power Generation Conference*. ASME, (2003).

65. Kiesewetter, F., Konle, M., and Sattelmayer, T. “Analysis of combustion induced vortex breakdown driven flame flashback in a premix burner with cylindrical mixing zone.” *J. Eng. Gas Turb. Power* 129, No. 4 (2007): 929-936.

66. Dam, B., Corona, G., Hayder, M., and Choudhuri, A. “Effects of syngas composition on combustion induced vortex breakdown (CIVB) flashback in a swirl stabilized combustor.” *Fuel* 90, No. 11 (2011): 3274-3284.

67. Lieuwen, T. and Zinn, B.T. “Theoretical investigation of combustion instability mechanisms in lean premixed gas turbines.” *AIAA paper* 98-0641, (1998).

68. Kendrick, D., Anderson, J., and Sowa, W. “Acoustic sensitivity of lean premixed fuel injectors in a single nozzle rig.” *ASME paper* 98-GT-382, (1998).

69. Kang, D.M., Fernandex, V., and Ratner, A. “Measurements of fuel mixture fraction oscillations of a turbulent jet non-premixed flame.” *Combust. Flame* 156, (2009):214-220.

70. Reynst, F. *Pulsating combustion: The collected works of F.H. Reynst*. Thring, M., ed. New York: Pergamom, (1961).

71. Ho, C. and Huerre, P. “Perturbed free shear layers.” *Annu. Rev. Fluid Mech.* 16, No. 1 (1984): 365-422.

72. Schadow, K.C. and Gutmark, E. “Combustion instability related to vortex shedding in dump combustors and their passive control.” *Prog. Energy Combust. Sci.* 18, No. 2 (1992): 117-132.

73. Culick, F.E.C. “Nonlinear behavior of acoustic waves in combustion chambers. Parts I and II.” *Acta Astronautica* 3, (1976): 714-757.

74. Kang, D.M., Culick, F.E.C., and Ratner, A. “Combustion dynamics of a low-swirl combustor.” *Combust. Flame* 151, No. 3 (2007): 412-425.

75. Huang, Y. and Ratner, A. “Experimental investigation of thermoacoustic coupling for low-swirl lean premixed flames.” *J. Propul. Power* 25, No. 2 (2009): 365-373.

76. Yilmaz, İ., Ratner, A., Ilbas, M., and Huang, Y. “Experimental investigation of thermoacoustic coupling using blended hydrogen-methane fuels in a low swirl burner.” *Int. J. Hydrogen Energy* 35, No. 1 (2010): 329-336.

77. Pun, W., Palm, S.L., and Culick, F.E.C. “PLIF measurements of combustion dynamics in a burner under forced oscillatory conditions.” *AIAA* (2000): 3123.

78. Allison, P.M., Driscoll, J.F., and Ihme, M. “Acoustic characterization of a partially-premixed gas turbine model combustor: Syngas and hydrocarbon fuel comparisons.” *Proc. Combust. Inst.* 34, No. 2 (2013): 3145-3153.

79. Huang, Y., Ratner, A., and Bethel, B. “Chamber pressure perturbation coupling with a swirl-stabilized lean premixed flame at elevated pressures.” In *5th US Combustion Meeting*, (2007).

80. Poinsot, T.J., Trouve, A.C., Veynante, D.P., Candel, S.M., and Esposito, E.J. “Vortex-driven acoustically coupled combustion instabilities.” *J. Fluid Mech.* 177, (1987): 265-292.

81. Shinjo, J., Mizobuchi, Y., and Ogawa, S. “LES of unstable combustion in a gas turbine combustor.” In *High Performance Computing*. Berlin: Springer Berlin Heidelberg, (2003): 234-244.

82. Cadou, C.P., Logan, P., Karagozian, A., Marchant, R., and Smith, O.I. “Laser diagnostic techniques in a resonant incinerator.” In *Optics, Electro-Optics, and Laser Applications in Sci. Engr.;* International Society for Optics and Photonics, (1991).

83. Allen, M.G., McManus, K.R., Sonnenfroh, D.M., and Paul, P.H., “Planar laser-induced-fluorescence imaging measurements of OH and hydrocarbon fuel fragments in high-oressure spray-flame combustion.” *Appl. Opt.* 34, No. 27 (1995): 6287-6300.

84. Ratner, A., Pun, W., Palm, S., and Culick, F.E.C. “Comparison of chemiluminescence, OH PLIF, and NO PLIF for determination of flame response to acoustic waves.” (2002).

85. Lieuwen, T. "CDMS helps prevent forced outages, tune engine after overhaul." *Combined Cycle Journal* 3rd Quarter, (2008): 89-97.

86. Lang, W., Poinsot, T., and Candel S. "Active control of combustion instability." *Combust. Flame* 70, No. 3, (1987): 281-289.

87. Goy, C.J., James, S.R., and Rea, S. "Monitoring combustion instabilities." Chapter 8. In: Lieuwen, T., Yang, V., ed. Combustion instabilities in gas turbine engines: operational experience, fundamental mechanisms, and modeling. *Prog. Astronaut. Aeronaut.* 210, (2005): 163-175.

88. Temkin, Samuel and Temkin, S. In *Elements of acoustics*. New York: Wiley, (1981).

89. Roberts, W.L., Driscoll, J.F., Drake, M.C., and Goss, L.P. "Images of quenching a flame by a vortex-to quantity regimes of turbulent combustion." *Combust. Flame* 95, (1993): 58-69.

90. Candel, S. and Sébastien, M. "Combustion instabilities coupled by pressure waves and their active control. In *Symp. (Int.) Combust.* 24, No. 1, 1277-1296.

91. Delabroy, O., Haile, E., Lacas, F., Candel, S., Pollard, A., Sobiesiak, A., and Becker, H.A. "Passive and active control of NO_x in industrial burners." *Exp. Therm. Fluid Sci.* 16, No. 1 (1998): 64-75.

92. Sobiesiak, A., Rahbar, S., and Becker H.A. "Development and performance evaluation of the new low NO_x CGRI for use with air high air preheat. *Combust. Flame, submitted.*

93. Tsein, H.S. "Servo-stabilization of combustion in rocket motors." *J. Am. Rocket Soc* 22, No. 5 (1952): 256-262.

94. Marble, F.E. and Cox, D.W. "Servo-stabilization of low-frequency oscillations in a liquid bipropellant rocket motor." *J. Am. Rocket Soc.* 23, (1953): 63-81.

95. Marble, F.E. "Servo-stabilization of low-frequency oscillations in liquid propellant rocket motors." (1955)

96. Crocco, L. and Cheng, S. "Theory of combustion instability in liquid propellant rocket motors." On behalf of the *Advisory Group for Aeronautical Research and Development*. North Atlantic Treaty Organization. (1956).

97. Keller, J.O. and Hongo, I. “Pulse combustion: The mechanism of NO_x production.” *Combust. Flame* 80 (1990): 219-237.

98. Dec, J.E. and Keller, J.O. “Pulse combustor tail-pipe heat-transfer dependence on frequency, amplitude, and mean flow rate.” *Combust Flame* 77 (1989): 359-374.

99. Dec, J.E., Keller, J.O., and Arpaci, V.S. “Heat transfer enhancement in the oscillating turbulent flow of a pulse combustor tail pipe.” *Int. J. Heat Mass Tran.* 35, No. 9 (1992): 2311-2325.

100. Hongo, I. and Saito, K. “Development of small twin-valveless pulse combustiors: effect of injection system.” *Combust. Sci. Technol.* 94, No. 1-6 (1993): 43-55.

101. Williams, J.E. Ffowcs. “Review lecture: Anti-sound.” *Proc. R. Soc. A* 395, No. 1808 (1984): 63-88.

102. Dines, P.J. “Active control of flame noise.” (PhD diss., University of Cambridge, 1983).

103. Heckl, M.A. “Active control of the noise from a Rijke tube.” In *Aero- and Hydro-acoustics* (1986): 211-216.

104. Bloxsidge, G.J. and Langhorne, P.J. “Active control of an acoustically driven combustion instability.” *Colloque Euromech* 213, (1996).

105. Ishino, Y., Kojima, T., Oiwa, N., and Yamguchi, S. “Acoustic excitation of diffusion flames with coherent structure in a plane shear layer.” *JSME B* 39, (1996): 156-163.

106. Neumeier, Y. “Experimental demonstration of active control of combustion instabilities using real-time modes of observation and secondary fuel injection.” In *Symp. (Int.) Combust.* 26, No. 2 (1996): 2811-2818. Elsevier.

107. Chigier, N.A. and Beer, J.M. “Velocity and static-pressure distributions in swirling air jets issuing from annular and divergent nozzles.” *J. Basic Eng.* 86, NO. 4 (1964): 788-796.

108. Davies, T.W. and Beer, J.M. “Flow in the wake of bluff-body flame stabilizers.” In *Symp. (Int.) on Combust.* 13, No. 1 (1971): 631-638. Elsevier.

109. Beer, J.M. and Chigier, N.A. "Combustion aerodynamics" *Applied Sci. Publ.,* London. (1972).

110. Lilley, G.D. "Swirl flows in combustion: A review." *AIAA Journal* 15, No. 8 (1977): 1063-1078.

111. Gupta, A.K., Beer, J.M., and Swithenbank, J. "On the operational characteristics of a multi-annular swirl burner." *Combust. Sci. Technol.* 17, N. 5-6 (1978): 199-214.

112. Sheen, H.J., Chen, W.J., and Jeng, S.Y. "Recirculation zones of unconfined and confined annular swirling jets." *AIAA Journal* 34, No. 3 (1996): 572-579.

113. Syred, N. "A review of oscillation mechanisms and the role of the precessing vortex core (PVC) in swirl combustion systems." *Prog. Energy Combust. Sci.* 32, No. 2 (2006): 93-161.

114. Huang, Y. and Yang, V. "Dynamics and stability of lean-premixed swirl-stabilized combustion." *Prog. Energy Combust. Sci.* 35, No. 4 (2009): 292-364.

115. Yamaoka, I. and Tsuji, H. "An anomalous behavior of methane-air and methane-hydrogen-air flames diluted with nitrogen in a stagnation flow." *24th Symp. (Int.) on Combust.,* The Combustion Institute, (1992): 145-152.

116. Jackson, G.S., Sai, R., Plaia, J.M., Boggs, C.M., and Kiger, K.T. "Influence of H_2 on the response of lean premixed CH_4 flames to high strained flows." *Combust. Flame* 132, No. 3 (2003): 503-511.

117. Lieuwen, T., McDonell, V., Petersen, E., and Santavicca, D. "Fuel flexibility influences on premixed combustor blowout, flashback, autoignition, and stability." *J. Eng. Gas Turb. Power* 130, No. 1 (2008): 011506.

118. Boschek, E., Griebel, P., and Jansohn, P. "Fuel variability effects on turbulent, lean premixed flames at high pressures." In *ASME Turbo Expo 2007: Power for Land, Sea, and Air*, (2007): 373-382.

119. Littlejohn, D., Noble, D.R., Lieuwen, T., and Cheng, R.K. "Laboratory investigations of low-swirl injectors operating with syngases." *J. Eng. Gas Turb. Power* 132, No. 1 (2010): 011502.

120. Halter, F., Chauveau, C., and Gökalp, I. "Characterization of the effects of hydrogen addition in premixed methane/air flames." *Int. J. Hydrogen Energy* 32, No. 13 (2007): 2585-2592.

121. Kim, H.S., Arghode, V.K., and Gupta, A.K. “Flame characteristics of hydrogen-enriched methane-air premixed swirling flames.” *Int. J. Hydrogen Energy* 34, No. 2 (2009): 1063-1073.

122. Scholte, T.G. and Vaags, P.B. “Burning velocities of mixtures of hydrogen, carbon monoxide and methane with air.” *Combust. Flame* 3 (1959): 511-524.

123. Milton, B.E. and Keck, J.C. “Laminar burning velocities in stoichiometric hydrogen and hydrogen-hydrocarbon gas mixtrues.” *Combust. Flame* 58, No. 1 (1984): 13-22.

124. Yu, G., Law, C.K., and Wu, C.K. “Laminar flame speeds of hydrocarbon + air mixtures with hydrogen addition.” *Combust. Flame* 63, No. 3 (1986): 339-347.

125. Lawn, C.J. and Schefer, R.W. “Scaling of premixed turbulent flames in the corrugated regime.” *Combust. Flame* 146, No. 1 (2006): 180-199.

126. Fairweather, M., Ormsby, M.P., Sheppard, C.G.W., and Woolley, R. “Turbulent burning rates of methane and methane-hydrogen mixtures.” *Combust. Flame* 156, No. 4 (2009): 780-790.

127. Kim, H.S., Arghode, V.K., Linck, M.B., and Gupta, A.K. “Hydrogen addition effects in a confined swirl-stabilized methane-air flame.” *Int. J. Hydrogen Energy* 34, No. 2 (2009): 1054-1062.

128. Mandilas, C., Ormsby, M.P., Sheppard, C.G.W., and Woolley, R. “Effects of hydrogen addition on laminar and turbulent premixed methane and iso-octane—air flames.” *Proc. Combust. Inst.* 31, No. 1 (2007): 1443-1450.

129. Tahtouh, T., Halter, F., Samson, E., and Mounaïm-Rousselle, C. “Effects of hydrogen addition and nitrogen dilution on the laminar flame characteristics of premixed methane-air flames.” *Int. J. Hydrogen Energy* 34, No. 19 (2009): 8329-8338.

130. Gauducheau, J.L., Denet, B., and Searby, G. “A numerical study of lean CH_4/H_2/air premixed flames at high pressure.” *Combust. Sci. Technol.* 137, No. 1-6 (1998): 81-99.

131. Kang, D.M. “Measurements of combustion dynamics with laser-based diagnostic techniques.” (PhD diss., California Institute of Technology, 2006).

132. Thévenin, D., Renard, P.H., Rolon, J.C., and Candel, S. "Extinction processes during a non-premixed flame-vortex interaction." In *Symp. (Int.) Combust.* 27, No. 1 (1998): 719-726. Elsevier.

133. Fritsche, D. "Origin and control of thermoacoustic instabilities in lean premixed gas turbine combustion." (PhD diss., ETH Zürich, 2005, 2006).

134. Driscoll, J.F. "Turbulent premixed combustion: Flamelet structure and its effect on turbulent burning velocities." *Prog. Energy Combust. Sci.* 34, No. 1 (2008): 91-134.

135. Singla, G., Scouflaire, P., Rolon, J.C., and Candel, S. "Flame stabilization in high pressure LO_x/GH_2 and GCH_4 combustion." *Proc. Combust. Inst.* 31, No. 2 (2007): 2215-2222.

136. Coriton, B., Frank, J.H., and Gomez, A. "Effects of strain rate, turbulence, reactant stoichiometry and heat losses on the interaction of turbulent premixed flames with stoichiometric counterflowing combustion products." *Combust. Flame* 160, No. 11 (2013): 2442-2456.

137. Bellows, B.D., Neumeier, Y., and Lieuwen, T. "Forced response of a swirling, premixed flame to flow disturbances." *J. Propul. Power* 22, No. 5 (2006): 1075-1084.

138. Weigand, P., Meier, W., Duan, X.R., Stricker, W., and Aigner, M. "Investigations of swirl flames in a gas turbine model combustor: I. Flow field, structures, temperature, and species distributions." *Combust. Flame* 144, No. 1 (2006): 205-224.

139. Beerer, D.J. "Combustion characteristics and performance of low-swirl injectors with natural gas and alternative fuels at elevate pressures and temperatures." (PhD diss., University of California, 2013).

140. Marshall, A., Venkateswaran, P., Seitzman, J., and Lieuwen, T. "Measurements of leading point conditioned statistics of high hydrogen content fuels." In *8^{th} US National Combustion Meeting*. (2013).

141. Kothnur, P.S., Tsurikov, M.S., Clemens, N.T., Donbar, J.M., and Carter, C.D. "Planar imaging of CH, OH, and velocity in turbulent non-premixed jet flames." *Proc. Combust. Inst.* 29, No. 2 (2002): 1921-1927.

142. Griebel, P., Siewert, P., and Jansohn, P. "Flame characteristics of turbulent lean premixed methane/air flames at high pressure: Turbulent flame speed and flame brush thickness." *Proc. Combust. Inst.* 31, (2007): 3083-3090.

143. Retrieved from <http://energy.lbl.gov/aet/combustion/LSC-Info/>.

144. Kaufman, K., Zhang, J., and Ratner, A. “Effect of frequency variation and driving pressure amplitude on global flame response in a low swirl burner.” Presented at the Spring Technical Meeting of the Central States Section of the Combustion Institute, Tulsa, OK. (March 16 – 18, 2014).

145. Davidson, T.A. “A simple and accurate method for calculating viscosity of gaseous mixtures.” (1993).

APPENDIX A: INCLUSIVE LIST OF OPERATING CONDITIONS

Table A.1: Operating Conditions in Flashback Examinations

α_{H_2}	ϕ	**Velocity [m/s]**
0.2	0.8	5
0.2	0.8	7.5
0.2	0.8	10
0.2	0.8	12.5
0.2	0.8	15
0.2	0.8	17.5
0.2	0.8	20
0.2	0.8	22.5
0.2	0.85	5
0.2	0.85	7.5
0.2	0.85	10
0.2	0.85	12.5
0.2	0.85	15
0.2	0.85	17.33
0.15	0.8	5
0.15	0.8	7.5
0.15	0.8	10
0.15	0.8	12.5
0.15	0.8	15
0.15	0.8	17.5
0.15	0.8	20
0.15	0.8	22.5
0	0.8	5
0	0.8	5.6
0	0.8	6.2
0	0.8	6.8
0	0.8	7.4
0	0.8	8

Table A.2: Operating Conditions in Blowout Examinations

α_{H_2}	Chamber Pressure [bar]	Velocity [m/s]
0.2	1	10
0.2	1	15
0.2	1	20
0.2	1	25
0.2	1	30
0.2	1	35
0.2	1.5	7.5
0.2	1.5	10
0.2	1.5	12.5
0.2	1.5	15
0.2	1.5	17.5
0.2	2	7.5
0.2	2	10
0.2	2	12.5
0.2	2	15
0.2	2	17.5
0	1	5
0	1	6.25
0	1	7.5
0	1	8.75
0	1	10
0	1	11.25
0	1	12.5
0	1	13.75
0	1	15
0	1.5	5
0	1.5	7.5
0	1.5	9.75
0	1.5	12
0	1.5	14.25
0	1.5	16.5
0	1.5	18.25

Table A.3: Operating Conditions in Examinations of Flame Structures.

α_{H_2}	**Chamber Pressure [bar]**	**Velocity [m/s]**
0	1	15
0	1.5	15
0	2	15
0.2	1	15.4
0.2	1.5	15.4
0.2	2	15.4
0	1	10
0.1	1	10
0.2	1	10

APPENDIX B: SIMPLIFYING THE THREE-COMPONENT GASEOUS MIXTURE RELATIONS

Volume Fractions of fuel species:

$$\alpha_{H_2} = \frac{V_{H_2}}{V_{H_2}+V_{CH_4}} \tag{2.4}$$

$$\frac{V_{CH_4}}{V_{H_2}+V_{CH_4}} = 1 - \alpha_{H_2}$$

$$\frac{V_{CH_4}}{V_{H_2}} = \frac{1-\alpha_{H_2}}{\alpha_{H_2}} \tag{4.8}$$

Molar ratio of methane to hydrogen:

$$\frac{\rho_{CH_4}}{\rho_{H_2}}\frac{MW_{H_2}}{MW_{CH_4}} = const.$$

$$\frac{\rho_{CH_4}}{\rho_{H_2}}\frac{MW_{H_2}}{MW_{CH_4}} = \frac{\frac{m_{CH_4}}{V_{CH_4}}MW_{H_2}}{MW_{CH_4}\frac{m_{H_2}}{V_{H_2}}}$$

$$\frac{m_{CH_4}}{m_{H_2}}\frac{V_{H_2}}{V_{CH_4}}\frac{MW_{H_2}}{MW_{CH_4}} = \frac{\rho_{CH_4}}{\rho_{H_2}}\frac{MW_{H_2}}{MW_{CH_4}}$$

$$\frac{n_{CH_4}}{n_{H_2}}\frac{V_{H_2}}{V_{CH_4}} = \frac{\rho_{CH_4}}{\rho_{H_2}}\frac{MW_{H_2}}{MW_{CH_4}}$$

$$\frac{n_{CH_4}}{n_{H_2}} = \frac{(1-\alpha_{H_2})}{\alpha_{H_2}}\frac{\rho_{CH_4}}{\rho_{H_2}}\frac{MW_{H_2}}{MW_{CH_4}} \tag{4.9}$$

Molar ratio of methane to hydrogen:

$$(F/A) = \phi\ (F/A)_{stoic}$$

$$\frac{m_f}{m_a} = \frac{\phi}{b}\frac{MW_f}{MW_a} \tag{4.10}$$

$$\frac{n_f}{n_a}\frac{MW_f}{MW_a} = \frac{\phi}{b}\frac{MW_f}{MW_a}$$

$$\frac{n_f}{n_a} = \frac{n_{CH_4}+n_{H_2}}{n_a} = \frac{\phi}{b}$$

$$\frac{n_{CH_4}}{n_a} + \frac{n_{H_2}}{n_a} = \frac{\phi}{b}$$

$$\frac{n_{CH_4}}{n_a} = \frac{\phi}{b} - \frac{n_{H_2}}{n_a} \tag{4.11}$$

Molar ratio of hydrogen to air:

$$\frac{n_{CH_4}}{n_{H_2}} = \frac{(1-\alpha_{H_2})}{\alpha_{H_2}}\frac{\rho_{CH_4}}{\rho_{H_2}}\frac{MW_{H_2}}{MW_{CH_4}} \tag{4.9}$$

$$\frac{n_{CH_4}}{n_a}\frac{n_a}{n_{H_2}} = \frac{(1-\alpha_{H_2})}{\alpha_{H_2}}\frac{\rho_{CH_4}}{\rho_{H_2}}\frac{MW_{H_2}}{MW_{CH_4}}$$

$$\left(\frac{\phi}{b} - \frac{n_{H_2}}{n_a}\right)\frac{n_a}{n_{H_2}} = \frac{(1-\alpha_{H_2})}{\alpha_{H_2}}\frac{\rho_{CH_4}}{\rho_{H_2}}\frac{MW_{H_2}}{MW_{CH_4}}$$

$$\left(\frac{\phi}{b}\frac{n_a}{n_{H_2}} - 1\right) = \frac{(1-\alpha_{H_2})}{\alpha_{H_2}}\frac{\rho_{CH_4}}{\rho_{H_2}}\frac{MW_{H_2}}{MW_{CH_4}}$$

$$\frac{n_a}{n_{H_2}} = \frac{b}{\phi}\left(1 + \frac{(1-\alpha_{H_2})}{\alpha_{H_2}}\frac{\rho_{CH_4}}{\rho_{H_2}}\frac{MW_{H_2}}{MW_{CH_4}}\right)$$

$$\frac{n_{H_2}}{n_a} = \frac{\phi}{b}\left[1 + \frac{(1-\alpha_{H_2})}{\alpha_{H_2}}\frac{\rho_{CH_4}}{\rho_{H_2}}\frac{MW_{H_2}}{MW_{CH_4}}\right]^{-1} \quad (4.12)$$

Volumetric ratio of air to hydrogen:

$$\rho_f V_f = \rho_{H_2} V_{H_2} + \rho_{CH_4} V_{CH_4}$$

$$\frac{m_f}{m_a} = \frac{\rho_f V_f}{\rho_a V_a} \text{ and } \frac{m_f}{m_a} = \frac{\phi}{b}\frac{MW_f}{MW_a}$$

$$\frac{\rho_{H_2} V_{H_2} + \rho_{CH_4} V_{CH_4}}{\rho_a V_a} = \frac{\phi}{b}\frac{MW_f}{MW_a} \quad (4.13)$$

$$MW_f = \sum x_i MW_i$$

$$MW_f = \frac{n_{CH_4}}{n_f} MW_{CH_4} + \frac{n_{H_2}}{n_f} MW_{H_2}$$

$$MW_f = \frac{n_{CH_4}}{n_a}\frac{n_a}{n_f} MW_{CH_4} + \frac{n_{H_2}}{n_a}\frac{n_a}{n_f} MW_{H_2}$$

$$MW_f = \frac{b}{\phi}\left(\frac{n_{CH_4}}{n_a} MW_{CH_4} + \frac{n_{H_2}}{n_a} MW_{H_2}\right)$$

$$\frac{\rho_{H_2} V_{H_2} + \rho_{CH_4} V_{CH_4}}{\rho_a V_a} = \frac{\phi}{b}\frac{1}{MW_a} \cdot \frac{b}{\phi}\left(\frac{n_{CH_4}}{n_a} MW_{CH_4} + \frac{n_{H_2}}{n_a} MW_{H_2}\right)$$

$$\frac{\rho_{H_2} V_{H_2} + \rho_{CH_4} V_{CH_4}}{\rho_a V_a} = \left(\frac{n_{CH_4}}{n_a}\frac{MW_{CH_4}}{MW_a} + \frac{n_{H_2}}{n_a}\frac{MW_{H_2}}{MW_a}\right)$$

$$\frac{\rho_a V_a}{\rho_{H_2} V_{H_2} + \rho_{CH_4} V_{CH_4}} = \left[\frac{n_{CH_4}}{n_a}\frac{MW_{CH_4}}{MW_a} + \frac{n_{H_2}}{n_a}\frac{MW_{H_2}}{MW_a}\right]^{-1}$$

$$\frac{\rho_a \frac{V_a}{V_{H_2}}}{\rho_{H_2} + \rho_{CH_4}\frac{V_{CH_4}}{V_{H_2}}} = \left[\frac{n_{CH_4}}{n_a}\frac{MW_{CH_4}}{MW_a} + \frac{n_{H_2}}{n_a}\frac{MW_{H_2}}{MW_a}\right]^{-1}$$

$$\rho_a \frac{V_a}{V_{H_2}} = \left[\rho_{H_2} + \rho_{CH_4}\frac{V_{CH_4}}{V_{H_2}}\right]\left[\frac{n_{CH_4}}{n_a}\frac{MW_{CH_4}}{MW_a} + \frac{n_{H_2}}{n_a}\frac{MW_{H_2}}{MW_a}\right]^{-1}$$

$$\frac{V_a}{V_{H_2}} = \left[\frac{\rho_{H_2}}{\rho_a} + \frac{\rho_{CH_4}}{\rho_a}\frac{V_{CH_4}}{V_{H_2}}\right]\left[\frac{n_{CH_4}}{n_a}\frac{MW_{CH_4}}{MW_a} + \frac{n_{H_2}}{n_a}\frac{MW_{H_2}}{MW_a}\right]^{-1}$$

$$\frac{V_a}{V_{H_2}} = \left[\frac{\rho_{H_2}}{\rho_a} + \frac{\rho_{CH_4}}{\rho_a}\frac{V_{CH_4}}{V_a}\right]\left[\frac{n_{H_2}}{n_a}\left(\frac{MW_{H_2} - MW_{CH_4}}{MW_a}\right) + \frac{\phi}{b}\frac{MW_{CH_4}}{MW_a}\right]^{-1} \quad (4.14)$$

Density of Mixture:

$$\rho_m = \sum \rho_i V_i \Big/ \sum V_i \quad (4.4)$$

$$\rho_m = \left(\rho_{H_2} V_{H_2} + \rho_{CH_4} V_{CH_4} + \rho_a V_a\right) \Big/ \left(V_{H_2} + V_{CH_4} + V_a\right)$$

$$\rho_m = \frac{\rho_{H_2} + \rho_{CH_4}\frac{V_{CH_4}}{V_{H_2}} + \rho_a\frac{V_a}{V_{H_2}}}{1 + \frac{V_{CH_4}}{V_{H_2}} + \frac{V_a}{V_{H_2}}} \quad (4.15)$$

Dynamic Viscosity of Mixture:

$$\mu_m = \sum x_i \mu_i \sqrt{MW_i} \Big/ \sum x_i \sqrt{MW_i} \quad (4.6)$$

$$\mu_m = \frac{x_{H_2}\mu_{H_2}\sqrt{MW_{CH_4}}+x_{CH_4}\mu_{CH_4}\sqrt{MW_{CH_4}}+x_a\mu_a\sqrt{MW_a}}{x_{H_2}\sqrt{MW_{CH_4}}+x_{CH_4}\sqrt{MW_{CH_4}}+x_a\sqrt{MW_a}}$$

$$n_t = n_{H_2} + n_{CH_4} + n_a$$

$$\mu_m = \frac{\frac{1}{n_t}\left(n_{H_2}\mu_{H_2}\sqrt{MW_{CH_4}}+n_{CH_4}\mu_{CH_4}\sqrt{MW_{CH_4}}+n_a\mu_a\sqrt{MW_a}\right)}{\frac{1}{n_t}\left(n_{H_2}\sqrt{MW_{CH_4}}+n_{CH_4}\sqrt{MW_{CH_4}}+n_a\sqrt{MW_a}\right)}$$

$$\mu_m = \frac{\mu_{H_2}\sqrt{MW_{H_2}}+\mu_{CH_4}\frac{n_{CH_4}}{n_{H_2}}\sqrt{MW_{CH_4}}+\mu_a\frac{n_a}{n_{H_2}}\sqrt{MW_a}}{\sqrt{MW_{H_2}}+\frac{n_{CH_4}}{n_{H_2}}\sqrt{MW_{CH_4}}+\frac{n_a}{n_{H_2}}\sqrt{MW_a}} \quad (4.16)$$

APPENDIX C: TABLE OF KINEMATIC VISCOSITIES FOR BINARY AND THREE-COMPONENT GASEOUS MIXTURES

Using Herning and Zipperer's[145] equation to calculate the dynamic viscosity of a mixture of gases is said to be valid for mixtures that do not contain significant amounts of hydrogen. Because the flames utilized in the current study are still lean in hydrogen, Herning and Zipperer's equation was used to determine dynamic mixture viscosities. Then, kinematic viscosities are presented only for mixtures containing a hydrogen volume fraction of less than or equal to 0.2.

Table C.1: Kinematic viscosities determined using mixture relations derived in Chapter 4 for fuel mixture consisting of 100% CH_4 – 0% H_2

Equivalence Ratio, ϕ	**Kinematic Viscosity, $\nu\ [\mu m^2/s]$**
1.00	9.542
0.95	9.524
0.90	9.505
0.85	9.487
0.80	9.468
0.75	9.449
0.70	9.431
0.65	9.412
0.60	9.392
0.55	9.373
0.50	9.354
0.45	9.335
0.40	9.315
0.35	9.295
0.30	9.276

Table C.2: Kinematic viscosities determined using mixture relations derived in Chapter 4 for fuel mixture consisting of 90% CH_4 – 10% H_2

Equivalence Ratio, ϕ	**Kinematic Viscosity, $\nu\ [\mu m^2/s]$**
1.00	9.629
0.95	9.607
0.90	9.584
0.85	9.562
0.80	9.539
0.75	9.517
0.70	9.494
0.65	9.471
0.60	9.448
0.55	9.425
0.50	9.401
0.45	9.378
0.40	9.354
0.35	9.331
0.30	9.307

Table C.3: Kinematic viscosities determined using mixture relations derived in Chapter 4 for fuel mixture consisting of 80% CH_4 – 20% H_2

Equivalence Ratio, ϕ	**Kinematic Viscosity, $\nu\ [\mu m^2/s]$**
1.00	9.731
0.95	9.705
0.90	9.678
0.85	9.651
0.80	9.624
0.75	9.597
0.70	9.569
0.65	9.542
0.60	9.514
0.55	9.486
0.50	9.458
0.45	9.430
0.40	9.401
0.35	9.373
0.30	9.344